A Multinuclear Solid State Nuclear Magnetic Resonance Investigation of the Preparation of Co, Pt and Ni Based Hydrogenation Catalyst Systems

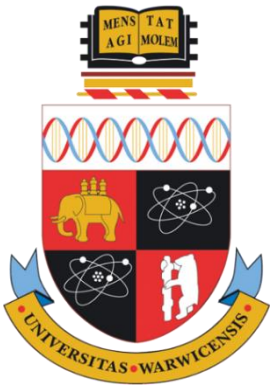

Joshua Patrick Clark

Department of Physics

University of Warwick

This dissertation is submitted for the degree of

Doctor of Philosophy

Declaration

The contents of this thesis are an original work and have not been submitted for a degree or qualification in this, or any other University. This thesis is the result of my own work and collaborative contributions have been indicated in the text. All sample syntheses were carried out at Johnson Matthey Technology Centre, UK by Dr. Peter Ellis. Single crystal X-ray diffraction measurements presented in Chapter 3 were carried out by Dr. Wim Klooster and Dr. Mateusz Pitak alongside Dr. Simon Coles at the UK National Crystallography Service based at the University of Southampton.

Joshua Patrick Clark

2017

Acknowledgements

A general thank you to all those that have supervised, discussed and supported my studies at Warwick. This work and opportunity would not have been possible without Dr John Hanna and his expertise; thank you.

This research motivation of the work presented has reflected the collaboration with Johnson Matthey. I am grateful for the opportunity to work with this fantastic company. Thank you to everyone at JM who have put time and effort into discussions throughout the last four years. Special thanks to Dr Peter Ellis whose expertise was fundamental to the success of this research, and whose patience was greatly appreciated. Apologies for the leg work required on some of the experimentation.

For my friends and colleagues at Warwick, cheers. It may not be possible to put into words the gratitude felt towards the community within the solid state NMR department at Warwick. To Sam Page, Thomas James Nelson Hooper and Maria Vlachou who begun this journey together with me, thank you.

My family deserve significant recognition, they have supported what some may describe as an eight year attempt to avoid doing any real work. Thank you for your support which was present right from the beginning.

Finally, my gratitude to the Engineering and Physical Sciences Research Council (EPSRC), Johnson Matthey and the University of Warwick whose financial contributions enabled this research.

Joshua P. Clark

Abstract

It was known highly dispersed Co (HDC) catalysts for Fischer-Tropsch applications could be synthesised from either Co metal or $CoCO_3$ precursors. Both synthesis routes were known to precipitate Co oxide nanoparticles from solution onto a support via Co(III) ammine complexes. The synthesis pathway was not known. Using solid state NMR and single crystal X-ray diffraction (XRD) a suite of Co(III) complexes have been characterised. The HDC catalyst synthesis from Co metal produced the Co(III) complex which was identified as $[(Co(NH_3)_3)_2(\mu\text{-}OH)_2(\mu\text{-}CO_3)](CO_3)\cdot 5H_2O$ via single crystal XRD. The ^{59}Co solid state NMR then confirmed the precipitant from the $CoCO_3$ route was the same complex.

The characterisation of a suite of Co(III) complexes of differing oxo coordination has been obtained. It was observed that each oxo coordinating ligand increased the NMR chemical shift by ~800 ppm. For a single oxo coordination a disparity of ~1000 ppm was also observed due to effects from the anion, crystallographic water and type of oxo coordination. Spin-spin coupling with the ^{59}Co nucleus was observed to occur for bidentate carbonate and ammine ligands yielded $|^2J(^{59}Co,^{13}C)|$ of 1-10 Hz and $|^1J(^{59}Co,^{15}N)|$ of 56-75 Hz. The bonding of monodentate and bridging carbonate ligands was observed to be ionic in nature lacking the spin-spin coupling.

It was hypothesised Co oxide nanoparticles precipitated from Werner's complex, $[Co((\mu\text{-}OH)_2Co(NH_3)_4)_3](SO_4)_3\cdot 9H_2O$. This was observed in the solid state NMR studies at 14518 ppm. From the time resolved ^{59}Co solution state NMR measurements of the HDC catalyst syntheses a resonance was observed at 14300 ppm. This was assigned to the central Co oxo coordinated environment of Werner's complex. In conjunction with observations of chemical shifts coinciding with known precursors to Werner's complex, it has been possible to suggest a reaction pathway. It was concluded that $[Co(NH_3)_5CO_3]^+$ and $[Co(NH_3)_4CO_3]^+$ eventually become Werner's complex before precipitating out of solution as Co oxide nanoparticles.

The study of Pt and Ni hydrogenation catalyst precursors on α-alumina, γ-alumina, silica and titania have been undertaken. From the Pt materials, it was observed oligomeric

Pt oxide structures deposited on the supports. The ^{195}Pt NMR measurements of these oligomeric structures showed disorder due to a mix of hydroxyl and O bridges in addition to preferential orientations. These orientations were thought to arise from the formation of sheet like structures. All measurements were compared to PtO_2, the ^{195}Pt measurement of which produced an axial symmetric lineshape due to chemical shift anisotropy yielding a Ω of 3916(100) ppm, κ of -1.00(8) and a δ_{iso} of 4607(100) ppm.

Finally, ^{27}Al measurements of the γ-alumina support showed reactions with nitric acid occurred. This formed an aluminium nitrate species on the surface which was removed with heat treatment. It was also concluded AlO(V) sites were preferential binding points for the Pt oxide. The AlO(V) ^{27}Al NMR resonance was seen to disappear with heat treatment, it has been proposed AlO(V) converts to AlO(VI) with the addition of Al–O–Pt bonds.

Contents

List of Figures

List of Tables

Nomenclature

NMR	Nuclear Magnetic Resonance
MAS	Magic Angle Spinning
FT	Fischer-Tropsch
DP	Deposition and Precipitation
HDC	Highly Dispersed Cobalt
JM	Johnson Matthey
EFG	Electric Field Gradient
PAS	Principle Axis System
CSA	Chemical Shift Anisotropy
CT	Central Transition
rf	Radio Frequency
VOCS	Variable Offset Cumulative Spectroscopy
CPMAS	Cross Polarisation Magic Angle Spinning
XRD	X-Ray Diffraction
ICP-MS	Inductively Induced Plasma Mass Spectroscopy
ATMA	Automatic Tuning and Matching
MQMAS	Multiple Quantum Magic Angle Spinning

Chapter 1 Introduction

1.1 The Role of NMR for Material Applications

Nuclear magnetic resonance (NMR) has been shown to be a diverse tool for structural and chemical characterisation. Since the first experiments by Purcell[1] and Bloch[2], the technique has been shown to be a powerful tool for obtaining atomic scale information. For example, the application of magnetic resonance imaging. Numerous specialities and perspectives have arisen, biological, inorganic and pharmaceutical applications represent areas solid state NMR plays significant roles.[3-5] However, the challenges of each of these areas can be unique from handling proteins to managing internal NMR interactions.

Solid state NMR can suffer from a lack of sensitivity and anisotropic interactions reducing the spectral resolution. Improving the latter typically focuses on the use of larger magnetic fields and magic angle spinning (MAS), a physical rotation of the sample.[6] Focusing on materials applications numerous methods are available via NMR without depending on these. For instance, the use of low fields can be vital for extracting quadrupole parameters[7] or for the study of paramagnetic species.[8] In specific situations significant quadrupole interactions allow for quadrupole resonance spectroscopy to be employed, and allows for chemical assignment without the need for an external magnetic field.[9] Furthermore, zero (internal) field NMR offers a method to study ferromagnetic materials again without an external magnetic field.[10]

The insensitivity of NMR has not limited its use in the study of catalytic materials, where surface species of interest make up only a few percent of the sample.[11,12] Studies utilise more “exotic” nuclei such as molybdenum[13], platinum[12] and

vanadium[5] NMR; information can aid in reducing the use of precious metals as well as identifying the active catalytic species. When required methods attempt to offset the drawback via isotopic enrichment (labelling) and polarisation transfer schemes (See section 2.2.6).

The studies presented in this thesis aim to demonstrate the use of multinuclear NMR to study commercially relevant catalytic materials. Predominantly work has focused on improving the understanding the precipitation of Co oxide nanoparticles from Co(III) ammine complexes. Cobalt catalysts are widely used in the gas or coal to liquids technologies which offer a method via which sustainable hydrocarbon fuels and products could be manufactured.[14] The final chapter of this thesis will aim to use solid state NMR to study catalyst support interactions via Pt and Ni hydrogenation catalyst precursors. It will be shown how a multi nuclear approach from an NMR perspective can allude to structural features and changing speciation. The comparison of different oxide supports informs similarities and differences in supporting mechanisms.

1.2 Motivations for Probing Fischer-Tropsch Nanoparticle Synthesis Routes

1.2.1 The Fischer-Tropsch Process

The Fischer-Tropsch (FT) reaction occurs over a suitable Group VIII metal and forms a key component of the gas to liquid, coal to liquid and biomass to liquids technologies.[15] Depending on the catalysts selectivity syngas, H_2 and CO, is converted into usable long chain hydrocarbons such as diesel fuel, kerosene, lubrication oils, waxes, etc.[16,17]. Due to the increased purity and quality of the FT products can demand a premium or be used to improve lower quality natural materials.[16]

Traditionally, natural gas or coal would act as a syngas precursor, however, the current economic climate targets the use of biomass.[18] The use of biomass could potentially offer a method of making carbon neutral transportation fuels and provide energy security.[19] The FT conversion of syngas into long chain hydrocarbons at elevated temperatures and pressures occurs in the presence of a catalyst. The first report of the FT reaction was reported in 1926 showed Co and Fe as FT catalysts, since then Ni and Rh have also been shown to be viable.[20,21] The conversation reaction:[22]

$$n\mathrm{CO}+2n\mathrm{H_2}\rightarrow(\mathrm{CH_2})_n+n\mathrm{H_2O} \qquad \text{(Equation 1-1)}$$

The number of units (n) in a product defining the production of a hydrocarbon species. However, depending on the catalyst selected the efficiency of reactions can be hindered by a water gas shift reaction which can cause a deactivation of the catalyst, such:[22]

$$\mathrm{CO}+\mathrm{H_2O}\leftrightarrow\mathrm{H_2}+\mathrm{CO_2} \qquad \text{(Equation 1-2)}$$

The FT reaction is highly exothermic and presents a key criterion for choosing the appropriate reactor design. At present, industrial FT reactors can be broadly categorised into slurry and fixed bed. Slurry bed reactors primary suffer from the difficulty associated with separation of the FT product and the catalyst, which has the additional effect of deactivation problems from attrition. However, water-cooling can be easily applied and provides control over the reaction temperature. Alternatively by fixing the catalyst to a surface the product remains pure, but controlling thermal conditions is difficult which in turn manifests as a larger capital cost.[15,23]

From the FT active catalysts, Fe has poor selectivity (preference for longer hydrocarbon chains) and is prone to deactivation but is the cheapest. Alternatively, Ru is highly selective but is too expensive for industrial applications where tonnes of material are needed.[24] Cobalt is the compromise, offering a high selectivity catalysts which is resistive to deactivation via the water gas shift reaction shown in Equation

1-2.[25] Cobalt nanoparticles have been used in both slurry and fixed bed reactors and allow for low temperature FT synthesis (operating in a range of 493-513 K).[26] The use of nanoparticles maximises surface area and thus maximising the dispersion of the active metal sites. However, it has been shown that particles should be larger than 9 nm in diameter otherwise efficiency and selectivity are normally lost.[26,27] The output from the Co catalysts is a wax (*n* up to 100 in Equation 1-1)[28,29] which can be processed with hydrocracking to achieve diesel fuel selectivity (*n* = 12-22 in Equation 1-1).[30]

1.2.2 Synthesis Methods for Co Oxide Nanoparticles

To increase surface area, catalysts are typically prepared on oxide supports, examples include SiO_2 (silica) and Al_2O_3 (alumina).[31] The production of supported Co nanoparticles varies, but have been shown to be synthesised from Co(II) salts such as $Co(NO_3)_2$, $Co(C_2H_3O_2)_2$ or $CoCO_3$.[32,33] There are also a number of production techniques which include: impregnation, strong electrostatic adsorption, deposition-precipitation and hydrothermal methods *etc*.[32,33] Choosing an appropriate precursor and technique is important to ensure catalysts are well dispersed, produce appropriately sized particles and are reproducible.[16]

The impregnation technique relies on the deposition of the Co salt (typically cobalt nitrate) onto a dry porous support material where incipient wetness impregnation distributes the precursor material. Although technically simple, the technique suffers from reproducibility problems and nonhomogeneous nanoparticle distributions; furthermore, depending on the pH of the precursor and the zero point charge of the support it is possible to have materials containing a mix of the catalyst and support due to dissolution.[16] This has been reported when $Co(C_2H_3O_2)_2$ has been used as a precursor, where an exothermic reaction with the silica support lead to the formation of cobalt silicate.[33,34]

Alternatively, precipitation is carried out from a Co solution which ensures particles are well dispersed. Furthermore, materials are reproducible and allow for the control of phase compositions and particle size.[35] However, both precipitation and impregnation require a calcination (heat treatment) to ensure metal oxides form, this can be carried out in air but can cause support catalyst interactions.[36,37] The metal catalysts can then be formed from the reduction of the oxides via treatment with H_2.[38]

A deposition and precipitation (DP) technique electrostatically deposits precursor cation and anions onto a support surface thus controlling the point of precipitation.[16,35] It has been shown the method reduces the risk of reacting the catalyst precursor and support material if an oxide precipitated to the surface.[32] In silicon fibres this method produces a catalyst with better activity than those from impregnation methods.[32]

1.2.3 Hypothesis for Studying Deposition and Precipitation of Co Oxide Nanoparticles via Co(III) Ammine Complexes

Utilising the DP method Johnson Matthey have previously reported a high dispersion cobalt (HDC) catalyst from Co metal and $CoCO_3$ precursors.[39] This HDC catalyst is known to be highly effective.[40] However, unlike many other catalysts in literature the precipitation of supported Co oxide nanoparticles occurs via a Co(III) ammine complex.[16] The exact mechanism of this reaction is not understood with very little information regarding the Co(III) complexes being presented.[39,41]

In this thesis, a significant effort has been undertaken to understand the precipitation of cobalt oxide nanoparticles from aqueous media. The synthesis is understood to contain numerous ammine species in a complex dynamic system. A greater understanding though could offer control over size and distribution, ratio of specific crystal phases and provide insight into scaling of production from batch to continuous.[16]

Solid and solution state ^{59}Co NMR measurements have been used to study the reaction mechanisms leading to the the precipitation of cobalt oxide nanoparticles. Solid state studies aim to characterise Co(III) ammine complexes which can be synthesised and crystallised out as single compounds.[42,43] Characterisation of solid state Co(III) complexes, with different degrees and types of oxo coordination, aims to allow individual species observed in solution state to be identified via their NMR chemical shifts. In addition, the solid-state complexes provide the opportunity to study the ligands. Thus, providing further insight into the reaction schemes driving the Co(III) ammine complexes evolution to higher oxo coordination. Single crystal X-ray diffraction measurements carried out by the National Crystallography Service at Southampton University have been used to verify synthesis products and further the analysis of NMR features.

Of the two synthesis methods used at Johnson Matthey to make HDC catalysts, the elemental Co metal route is not a common precursor for ammine complexes. Catalytic products from the Co metal route are considered by JM to be very similar (almost identical) to the $CoCO_3$ route. Further verification of similarities between the two routes was also seen in the study of solid precipitants isolated during the synthesis. From literature, Co(II) salts are common precursors for ammine coordination complexes and a better understanding of the metal synthesis should be achievable by drawing comparisons to the $CoCO_3$ method.[42-44] Thus, the initial hypothesis for the precipitation of cobalt oxide nanoparticles will focus on the $CoCO_3$ route illustrated in Figure 1-1 (synthesis route from literature is described here[43]).

The known presence of ammine complexes[39] in the HDC synthesis, prior to the precipitation of Co oxide nanoparticles, indicates the potential for the formation of $[Co(NH_3)_5CO_3]X$ (where X is an appropriate counter ion when crystallised out). When synthesised via literature methods the counter ion X, is reported to be controllable via the Co(II) salt used.[42] However, it was not possible to crystallise out a complex with a carbonate anion ($X = CO_3$). The formation of this tetrammine complex is probable due to the similarities of the precursor materials illustrated in

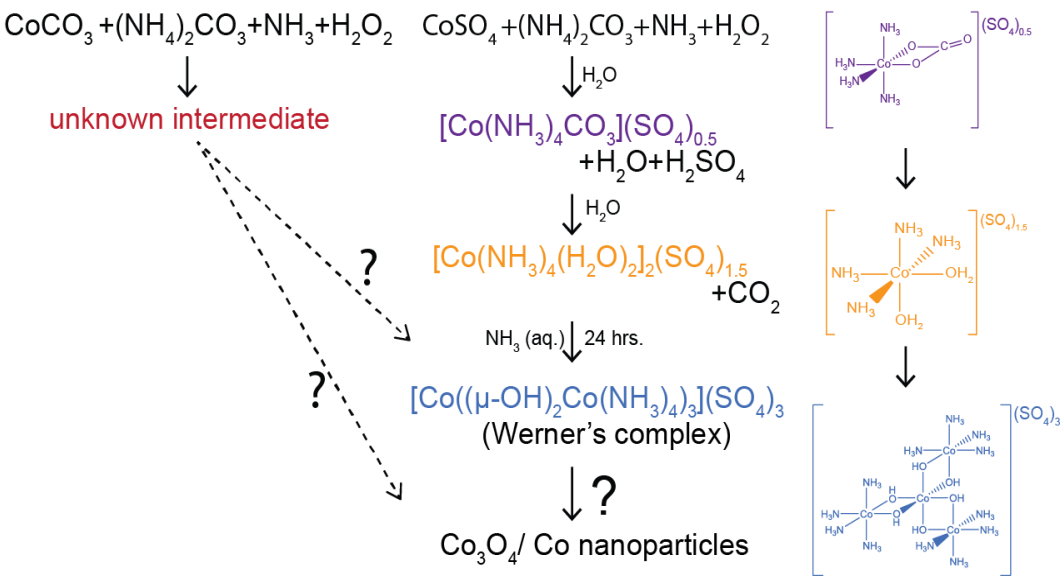

Figure 1-1: Initial high dispersion catalyst (HDC) route is shown on the left next to a known evolution route found in literature which is hypothesised to lead to the formation of cobalt oxide nanoparticles (see main text). It is not known if or how these two schemes compare, illustrated by the dashed arrows.

Figure 1-1. The carbonatotetrammine complexes are also known to be precursors to $[Co((\mu–OH)_2Co(NH_3)_4)_3]X$, the sulphate version being referred to as Werner's complex for the remainder of the report. As shown in Figure 1-1 Werner's complex has an oxygen coordinated core.[43] It is hypothesised that from Werner's complex continued growth of the oxygen coordinated core could lead to the precipitation of cobalt oxide nanoparticles as illustrated in Figure 1-1.

The characterisation via NMR of Werner's complex also has significant historical relevance for modern coordination chemistry.[45] Alfred Werner hypothesised the octahedral configuration of transition metal ions which forms the foundation of modern coordination chemistry.[46] The proof of Werner's theories was the measurement of optical activity, where the axis of polarised light is adjusted upon passing through the compound, of Werner's complex (originally a bromide version).[46,47]

During the preparation of Werner's complex several steps allow for the sampling of isolated compounds which are seen via the structure diagrams in Figure 1-1. These compounds include a tetrammine species oxygen coordinated to a bidentate carbonate, and its substitution with water ligands. Thus, the type of oxo coordination can be explored and should shed further insight usable to analyse unknown materials which are in the HDC syntheses.[39] It has been illustrated in Figure 1-1 that the ammine complex can be isolated from the HDC synthesis. However, it is unknown where in the hypothesised route to Werner's complex the compound would fit, if this is the route to cobalt oxide nanoparticles. Thus, verification of this complex within the literature reaction would support the hypothesis.

A combined solid state and solution state study should enable details of the nanoparticle precipitation and deposition of the HDC synthesis. Furthermore, a multinuclear approach should enable a fuller picture of the active complexes to be understood. This approach should enable equilibria and evolution pathways of the Co(III) complexes to be suggested.

A full reaction pathway is not possible via NMR though due to the different magnetic properties of the Co oxidation states. The Co(III) precursors discussed thus far are low spin (d^6) and form diamagnetic octahedral complexes which are ideal for NMR studies. However, the Co_3O_4 which precipitates out of the industrial synthesis would be ferromagnetic and thus is NMR silent.[48] The final state of consideration is the Co(II) complexes that may occur during the synthesis and are high spin (d^7) and are paramagnetic.[49] In the scenario under study it is expected the paramagnetic species within the solution studies would cause a broadening of the NMR spectra but should not degrade the NMR measurements to a significant degree.

1.3 Catalytic Supports

1.3.1 The role of Metal Oxide Support Materials

Hydrogenation via heterogeneous catalysis represents huge commercial investment. The hydrogenation reaction plays a key role in food, petrochemical and pharmaceutical industries.[50-52] Precious metals (Pt, Rh, Ru and Pd) are typically used as highly efficient catalysts, enabling the reaction to occur at greatly reduced temperatures.[53,54] However, due to the expense Ni catalysts can be used as an economic alternative.[55] However, the trade off to Ni based catalysts can mean reactions require additional heat and pressure to achieve reactivities comparable to precious metal counter parts.[51]

The role of inorganic oxide supports is significant in heterogeneous catalysis. The high surface area of the oxide support materials (which can be around 200 m^2 per gram) enables a large dispersion of the precursors.[56] Thus, upon calcination and reduction, agglomeration of the catalyst materials can be minimised. Good dispersion maximises the catalyst surface area, the location of the catalytically active sites making efficient use of sometimes expensive materials, such as platinum.[56]

Catalyst efficiencies are not subject to just the increased dispersion support materials provide. There are also “strong metal-support interactions”, which over time have been associated to the migration of support across nanoparticle surfaces, however, the term should not be limited to this definition.[57] The interactions are not necessarily detrimental to catalytic activity as with the previous example, catalyst structures perturbed by the lattice of the support can be beneficial.[58] These aiding the bonding of catalyst and reactant. The nature of these interactions can even extend to electronic effects, it has been reported perturbing the election configuration of platinum clusters on cerium dioxide can also improve catalytic performance.[59]

Many oxides are used for catalyst supports, α-alumina, γ-alumina, silica and titania represent four common support materials.[60] A previous study of FT catalysts looked at oxide support effects on Co oxide nanoparticles.[61] It was reported small pore (γ-

alumina and silica) yielded clusters of small particles and evenly distributed single particles when pore size was larger (α-alumina and titania).[61] For γ-alumina it has been reported smaller particles generally bind electrostatically, but as these grow evidence is subjective and may incorporate surface hydroxyls into immediate coordination sphere.[62]

Consequently, the study of how catalysts are mounted onto the support surface is of significant interest to Johnson Matthey. Insight into preferential binding sites, structural morphology and speciation can all aid the development of the materials. Thus, utilising solid state NMR a study of several support materials has been undertaken. The aims of the study are to utilise NMR to probe the catalyst support interactions and propose avenues of potential research interest. Studies have focused on metal oxides derived from metal nitrate solutions via calcination on α-alumina, γ-alumina, silica and titania. The metal catalysts chosen were platinum and nickel, the use of the latter allowed for a more sensitive study of nitrate species since the precursor could be isotopically labelled. This cannot be carried out for platinum materials due to technical difficulties. The use of ^{195}Pt solid state NMR has already been demonstrated to be a power tool for catalyst applications and has been used to provide insight from the catalyst perspective.[12]

Chapter 2 Theory and Techniques

2.1 Introduction to Nuclear Magnetic Resonance

Nuclear magnetic resonance NMR relies upon the intrinsic property of nuclear spin, which is represented by the quantum number *I*. This is related to the nuclear dipole moment (μ),

$$\underline{\mu} = \gamma \hbar \underline{I} \qquad \text{(Equation 2-1)}$$

where $\hbar$ = h/2π, h is the Planks constant and γ is the gyromagnetic ratio which is nuclei specific. It is the nuclear dipole moment which interacts with the applied magnetic field, this is the basis for the NMR experiment (see Section 2.1.1.1). Almost all elements have at least one naturally occurring magnetically active isotope making most of the periodic table accessible by the technique. The only magnetically silent elements with no overall spin, $I = 0$ are Ar and Ce.[63]

A plethora of information regarding the atomic scale becomes available via NMR. The challenge is understanding how the numerous interactions can affect the solid-state NMR spectrum and how to deconvolute them. Research has utilised ^{59}Co NMR which not only produces convoluted spectra, as will be shown, but perturbs the NMR spectra of the nuclei around it. The aim of this chapter is to provide insight into the terminology of the technique, introduce the common interactions encountered and their influence with one another.

2.1.1 Single and Convoluted Interactions

The NMR Hamiltonian, H_{tot}, is a sum of all interactions which act to perturb the nuclear system. By understanding the Hamiltonian of each interaction information

about the nuclear environment can be obtained. For the studies undertaken a concise NMR Hamiltonian is presented,

$$\widehat{H}_{Total} = \widehat{H}_Z + \widehat{H}_{CS} + \widehat{H}_D + \widehat{H}_Q^{(1)} + \widehat{H}_Q^{(2)} + \widehat{H}_J + \cdots, \quad \text{(Equation 2-2)}$$

where $\widehat{H}_Z$ is the Zeeman interaction between the magnetic moment and the external applied magnetic field. The use of sufficiently high magnetic field allows for the secular approximation where by all others are perturbations of the Zeeman interaction. The chemical shielding represented by $\widehat{H}_{CS}$ arises from the electrons responding to the applied field which perturbs the field around the nucleus. Two magnetic dipoles in close enough proximity will also interact, accounted for via $\widehat{H}_D$. The non-spherical charge distribution of some nuclei gives rise to an electric quadrupole moment which interacts with electric field gradient (EFG) about the nucleus. This can be significant in magnitude and for an accurate analysis of the NMR spectrum both first order ($\widehat{H}_Q^{(1)}$) and second order ($\widehat{H}_Q^{(2)}$) effects may be needed to be accounted for. The final interaction to be discussed is the J-coupling, a quantum mechanical through bond effect $\widehat{H}_J$. However, the Hamiltonians presented in Equation 2-2 are not exhaustive. Effects from paramagnetism and the Knight shift (due to effects of conduction electrons) can also arise. These have not been observed in the research presented here but descriptions can be found in the literature.[64]

2.1.1.1 Zeeman interaction

In the presence of an external magnetic field, $B_0 = (0, 0, B_z)$, as is the case in NMR a magnetic moment will classically experience a torque. The resultant force causes a precessional motion at an angular frequency ω_0, known as the Larmor frequency:

$$\omega_0 = \gamma B_z \quad \text{(Equation 2-3)}$$

From the quantum mechanical perspective, it has been shown that the Zeeman Hamiltonian, mentioned previously, also relies on the same characteristic frequency:

$$\widehat{H}_Z = -\gamma \hbar I_z B_z = -\hbar I_z \omega_0 \quad \text{(Equation 2-4)}$$

The Larmor frequency corresponds to the energy difference between two energy levels which in the presence of a magnetic field are no longer degenerate as shown by Figure 2-1. The lifting of the degeneracy can be thought of as the spin aligning with or against the magnetic field. A population difference arises due to alignment of spin against the field being energetically less favourable. For quadrupolar nuclei which have a higher I, such as a spin $I = 7/2$ nuclei which ^{59}Co is will experience 8 energy levels ($2I + 1$). Typically, the Zeeman interaction is significantly stronger than any of the internal interactions and allows for a simplified analysis of $\widehat{H}_{Total}$.[64,65]

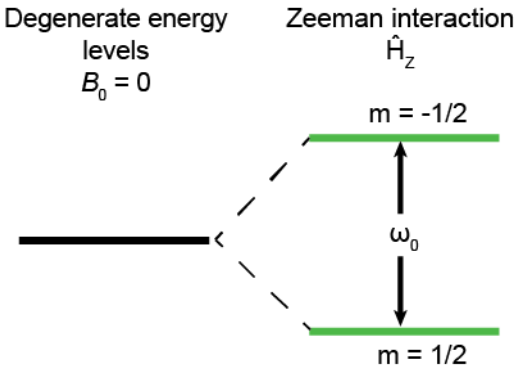

Figure 2-1: schematic representation of how the two spin states of a $I = 1/2$ nuclei split due to the Zeeman interaction, where the magnitude of the splitting is the Larmor frequency (proportional to the applied magnetic field B_0).

2.1.1.2 Dipolar Interaction

The dipolar interaction acts directly through space along an internuclear vector (r). The Hamiltonian $\widehat{H}_D$ introduced in Equation 2-2 can be expressed between two spins I and S, such:

$$\widehat{H}_D = \frac{\mu_0}{4\pi}\frac{\gamma_I \gamma_S \hbar}{r^3}\left(\underline{I}\cdot\underline{S} - \frac{3(\underline{I}\cdot\underline{r})(\underline{S}\cdot\underline{r})}{r^2}\right) \qquad \text{(Equation 2-5)}$$

where μ_0 is the permeability of free space. Typically, Equation 2-5 can be expressed in spherical tensor coordinates, as shown elsewhere.[64,65] Although it is important to note that when this is done the terms relevant to NMR are found to have a $3\cos^2\theta$ –

1 dependency which makes the interaction reducible via magic angle spinning (MAS) (see Section 2.2.3).[64]

The relationship with r seen in Equation 2-5 means that manipulation of the dipolar coupling can be used to probe internuclear distances, such is carried out in protein studies.[3] Furthermore, magnetisation transfer techniques such as cross polarisation MAS (CPMAS) are mediated via the dipolar interaction.[65]

2.1.1.3 Chemical Shielding

The perturbation of the Zeeman interaction via the chemical shielding is unique to each chemical environment. Physically the chemical shielding is a response of the electrons surrounding the nucleus to the external magnetic field. However, this response can vary depending on diamagnetic or paramagnetic contributions, reducing or adding to the effective field respectively.[65] The Hamiltonian $\widehat{H}_{CS}$ can be summarised:

$$\widehat{H}_{CS} = \gamma \underline{I} \cdot \boldsymbol{\sigma} \cdot \underline{B}_0 \qquad \text{(Equation 2-6)}$$

where the chemical shielding tensor ($\boldsymbol{\sigma}$) is a second rank tensor and describing the orientation dependence of the electron distribution. For a sufficiently fine powder sample it is often assumed all orientations are equally represented, this yields characteristic lineshapes.[65] Since the chemical shielding is related to the electron distribution the interaction is sensitive to chemical bonding environment.[66] Furthermore, the interaction is proportional to B_0, thus if anisotropic components need to be reduced then going to lower magnetic fields can provide useful.

Experimentally, difficulties measuring unshielded nuclei mean the chemical shift (δ) is a more accessible parameter rather than chemical shielding. Variations in B_0 between different experiments or different species of equipment have been circumvented by normalising with respect to a reference sample. Thus, the chemical shift is related to the shielding such:

$$\delta = \frac{(\sigma_{ref} - \sigma_{sample})}{(1 - \sigma_{ref})}(\times 10^6) = \frac{\nu_{sample} - \nu_{ref}}{\nu_{ref}}(\times 10^6) \qquad \text{(Equation 2-7)}$$

The frequencies (ν) of the sample and reference material (denoted by subscripts) which allow for the experimental determination of the chemical shift. Thus, rather than discuss the chemical shielding tensor the related chemical shift tensor is more appropriate. As mentioned the chemical shift can yield anisotropic components which are measured as anisotropies of chemical shift, better names chemical shift anisotropy (CSA).

Frames of reference become important when discussing NMR interactions, with the experimentalists frame termed the "LAB" frame defining the z axis to be parallel to the applied magnetic field. However, an orientation dependant interaction like CSA utilises the principle axis system of the interaction, in this system the off-diagonal components are by definition 0, thus:

$$\delta^{PAS} = \begin{pmatrix} \delta_{11} & 0 & 0 \\ 0 & \delta_{22} & 0 \\ 0 & 0 & \delta_{33} \end{pmatrix} \qquad \text{(Equation 2-8)}$$

Defining the principle components of Equation 2-8 is carried out such $\delta_{11} \geq \delta_{22} \geq \delta_{33}$ as seen in Figure 2-2, where δ_{11} is the least shielded and is the most shielded (see Figure 2-3). The isotropic chemical shift (δ_{iso}) is the average of the three principle components as shown:

$$\delta_{iso} = \frac{\delta_{11} + \delta_{22} + \delta_{33}}{3} \qquad \text{(Equation 2-9)}$$

The definition of the principle components outlined in Equation 2-8 and 2-9 together are the standard convention for the CSA. However, two other conventions are regularly used which are the Herzfeld-Berger and Haeberlen conventions, both define the δ_{iso} the same as the standard convention.[67] However, Herzfeld-Berger via two parameters, firstly is the span Ω, which describes the breadth of the lineshape, such:

$$\Omega = \delta_{11} - \delta_{33}, \Omega > 0 \qquad \text{(Equation 2-10)}$$

The second parameter is the skew κ, a measure of the symmetry of the tensor and can be seen via the location of δ_{22}. The κ is defined such:

$$\kappa = \frac{3(\delta_{22}-\delta_{iso})}{(\delta_{11}-\delta_{33})}, (-1 \leq \kappa \leq 1) \qquad \text{(Equation 2-11)}$$

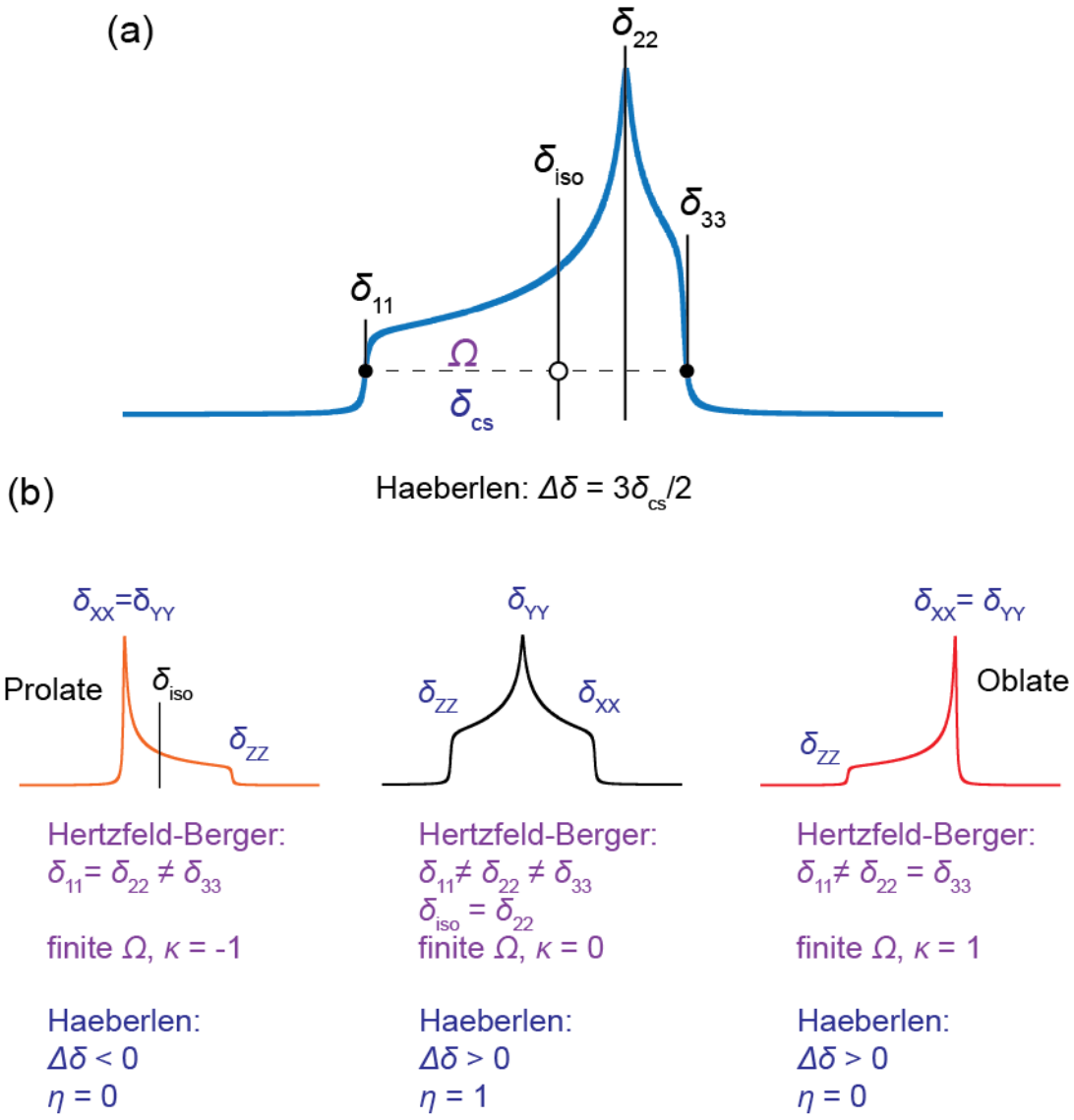

Figure 2-2: A summary of how CSA parameters are defined, (a) shows the standard convention parameters via solid lines. The span Ω can also be seen in (a) defined by the difference between δ_{11} and δ_{33} (the solid circles) and the reduced anisotropy δ_{cs} defines the difference in this case between δ_{11} and δ_{iso} (left hand solid and the hollow circles). Examples of CSA lines are shown in (b) the prolate and oblate lines being examples of axially symmetry.

A change in notation of the principle components has been carried out to distinguish the differences key differences between the conventions. Rather than keeping the components in order from high frequency to low frequency the Haeberlen convention defines them by the magnitude of the difference from the δ_{iso}, thus:

$$|\delta_{ZZ} - \delta_{iso}| \geq |\delta_{XX} - \delta_{iso}| \geq |\delta_{YY} - \delta_{iso}| \qquad \text{(Equation 2-12)}$$

Examples of how this second notation is applied can be seen in Figure 2-2(b), where a change in δ_{ZZ} from high frequency to low frequency can be seen for the prolate and oblate lineshapes. As stated before the δ_{iso} is still an average of the three principle components in Equation 2-12. However, there are now two anisotropy parameters which will be labelled reduced anisotropy and anisotropy to try and remove some of the ambiguity, firstly the reduced (δ_{cs}):

$$\delta_{cs} = \delta_{ZZ} - \delta_{iso} \qquad \text{(Equation 2-13)}$$

The NMR software dmfit[68] for lineshape analysis provides a value of δ_{cs}, although this is easily confused this with the anisotropy ($\Delta\delta$):

$$\Delta\delta = \frac{\delta_{ZZ} - (\delta_{XX} + \delta_{YY})}{2} = \frac{3\delta_{cs}}{2} \qquad \text{(Equation 2-14)}$$

The final parameter required to describe the deviation from axial symmetry is the asymmetry parameter (η), such:

$$\eta = \frac{(\delta_{YY} - \delta_{XX})}{\delta_{cs}}, (0 \leq \eta \leq 1) \qquad \text{(Equation 2-15)}$$

The limits of η define axial symmetry at 0 and its deviation from it at greater values, it cannot discern oblate or prolate though as seen with the κ (see Figure 2-2(b)). Standard, Herzfeld-Berger and Haeberlen conventions will be in the summary tables of the experimental chapters, however, Herzfeld-Berger will be the convention used mostly due to its relative clarity.

Finally, Figure 2-3 shows a visual demonstration of the terminology often found in NMR literature. Some terms such as those due to increasing and decreasing B_0 are no longer accurate with the use of static external magnetic fields. The terminology is

from when the NMR measurements were undertaken using electromagnets by starting at a high magnetic field and by removing the current B_0 could be varied.

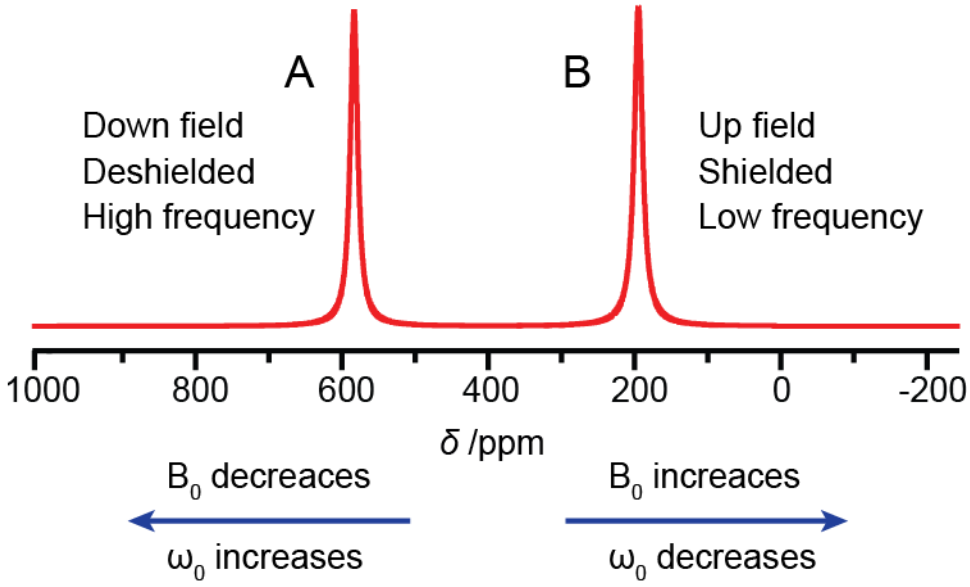

Figure 2-3: NMR terminology used to describe the position of resonances. Some terms are historical, surviving from when field sweep method was used rather than the modern Fourier-Transform method.

2.1.1.4 Quadrupolar Interaction

In addition to the CSA the quadrupolar interaction, from a nucleus with $I > 1/2$, can dominate spectra. Characteristic lineshapes are present if the magnitude of the interaction is large enough. The non-spherical charge distributions have an associated quadrupole moment which interacts with the electric field gradient (EFG). The EFG can be generated from local nuclei but also from chemical effects beyond the immediate coordination sphere. The significant magnitude of the quadrupolar interaction requires expansion of the Hamiltonian to the second order, such:[69]

$$\hat{H}_Q = \hat{H}_Q^{(1)} + \hat{H}_Q^{(2)} \qquad \text{(Equation 2-16)}$$

From an illustrative perspective, the first order quadrupolar interaction shifts the 1/2 to -1/2 central transition (CT) maintaining the characteristic splitting, shown in Figure 2-4. It is the second order interaction which characteristically perturbs the

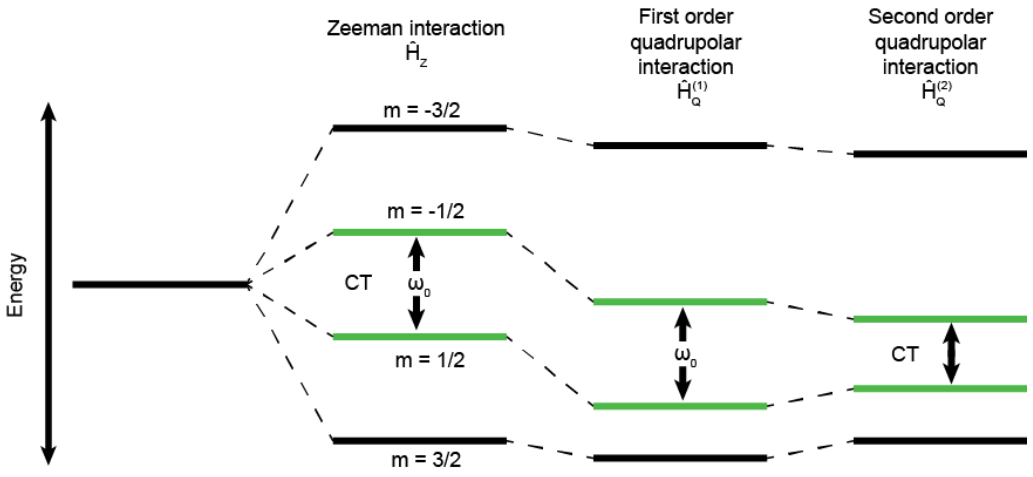

Figure 2-4: Energy level splitting for a quadrupolar nucleus, $I = 3/2$ illustrating how the energy levels are perturbed by the first and second order quadrupolar interactions. The central transition is highlighted in green.

central transition, as shown in Figure 2-4, where the CT has been highlighted in green. A general form of the Hamiltonian for the quadrupolar interaction can be expressed such:[65]

$$\widehat{H}_Q = \frac{eQ}{2I(2I-1)\hbar} \underline{I} \cdot \boldsymbol{V} \cdot \underline{I} \qquad \text{(Equation 2-17)}$$

Where e is the electric charge and Q is the nuclear quadrupole moment. Finally, $\boldsymbol{V}$ is the EFG described by a second rank tensor which in the PAS has a comparable form to Equation 2-8 (where the off diagonal components are all zero). The principle components of the EFG are labelled such $|V_{ZZ}| \geq |V_{YY}| \geq |V_{XX}|$, furthermore the quadrupole interaction has no isotropic component, thus the trace (sum of the diagonal) is zero. The tensor can be expressed via two variables the first being the quadrupole coupling constant (C_Q) which describes the magnitude of the interaction, such:

$$C_Q = \frac{eQV_{ZZ}}{h}. \qquad \text{(Equation 2-18)}$$

The variables of Equation 2-18 are as defined before note the use of the standard Plank's constant, C_Q has units of hertz. The second parameter is the asymmetry

parameter (η_Q), not to be confused with the similar parameter of the Haeberlen convention for CSA,

$$\eta_Q = \frac{V_{YY} - V_{XX}}{V_{ZZ}} \ . \qquad \text{(Equation 2-19)}$$

Thus, NMR of quadrupolar nuclei are reported quoting a δ_{iso}, C_Q and the unit less η_Q. Where $0 \leq \eta_Q \leq 1$, with 0 being axially symmetric tensor for the EFG in the PAS. As illustrated before, the first order quadrupolar interaction does not perturb the CT. Thus, discussion will focus on the second order perturbation ($\hat{H}_Q^{(2)}$) since this is what will be observed experimentally. This is not an exhaustive derivation of the origin of quadrupolar lineshapes, but aims to introduce the complexity contained within the measurements to be undertaken, for a detailed derivation the reader is directed elsewhere.[69-71] The second order Hamiltonian can be expressed as a Cartesian tensor commuting with the lab frame which has been shown to be of the form:

$$\hat{H}_Q^{(2)} = -\frac{1}{\omega_0}\left(\frac{eQ}{4I(2I-1)\hbar}\right)^2 \left\{2\left(V_{xz} - iV_{yz}\right)\left(-V_{xz} - iV_{yz}\right)\hat{I}_z\left[4I(I+1) - 8\hat{I}_z^2 - 1\right] + 2\left(\frac{1}{2}\left(V_{xx} - V_{yy}\right) - iV_{xy}\right)\left(\frac{1}{2}\left(V_{xx} - V_{yy}\right) + iV_{xy}\right)\hat{I}_z\left[2I(I+1) - 2\hat{I}_z^2 - 1\right]\right\} \qquad \text{(Equation 2-20)}$$

The consequences of Equation 2-20 are the formation of an orientation dependant lineshape in the NMR spectrum. The lineshapes broaden more significantly in low field spectra since $\hat{H}_Q^{(2)}$ is proportional to the inverse of B_0. Following the derivation shown in literature[69], Equation 2-20 can be used to calculate the shift of the Zeeman splitting due to the second order effects. The expression of the frequency shift in terms of the PAS in the observation frame is achieved utilising the Wigner rotation matrix. The Wigner rotation matrix allows for a spherical tensor such as the EFG tensor to be expressed in a different coordinate frame via three positive rotations θ, ϕ, and χ (this also applies to $\boldsymbol{\delta}^{PAS}$ expressed in the EFG PAS or lab frames). Thus, the second order quadrupolar frequency shift of the CT using the definitions given in Equations 2-17 and 2-18 is given as:

$$\omega^{(2)}_{-\frac{1}{2},\frac{1}{2}} = -\frac{1}{6\omega_0}\left(\frac{3C_Q}{4\pi I(2I-1)\hbar}\right)^2\left[I(I+1)-\frac{3}{4}\right]\left[A(\theta,\eta_Q)\cos^4\phi + B(\theta,\eta_Q)\cos^2\phi + C(\theta,\eta_Q)\right] \quad \text{(Equation 2-21)}$$

The variables $A(\theta, \eta_Q)$, $B(\theta, \eta_Q)$ and $C(\theta, \eta_Q)$ are defined in Equations 2-21 to 2-23:

$$A(\theta,\eta_Q) = -\frac{27}{8} + \frac{9}{4}\eta_Q\cos 2\theta - \frac{3}{8}(\eta_Q\cos 2\alpha)^2 \quad \text{(Equation 2-22)}$$

$$B(\theta,\eta_Q) = \frac{30}{8} - \frac{1}{2}{\eta_Q}^2 - 2\eta_Q\cos 2\theta + \frac{3}{4}(\eta_Q\cos 2\theta)^2 \quad \text{(Equation 2-23)}$$

$$C(\theta,\eta_Q) = -\frac{3}{8} - \frac{1}{3}{\eta_Q}^2 - \frac{1}{4}\eta_Q\cos 2\theta + \frac{3}{8}(\eta_Q\cos 2\theta)^2 \quad \text{(Equation 2-24)}$$

The third angle χ for the Wigner rotation matrix does not play a role in Equation 2-21 due to the B_z being a symmetry axis. Also, Equation 2-21 is for a static single

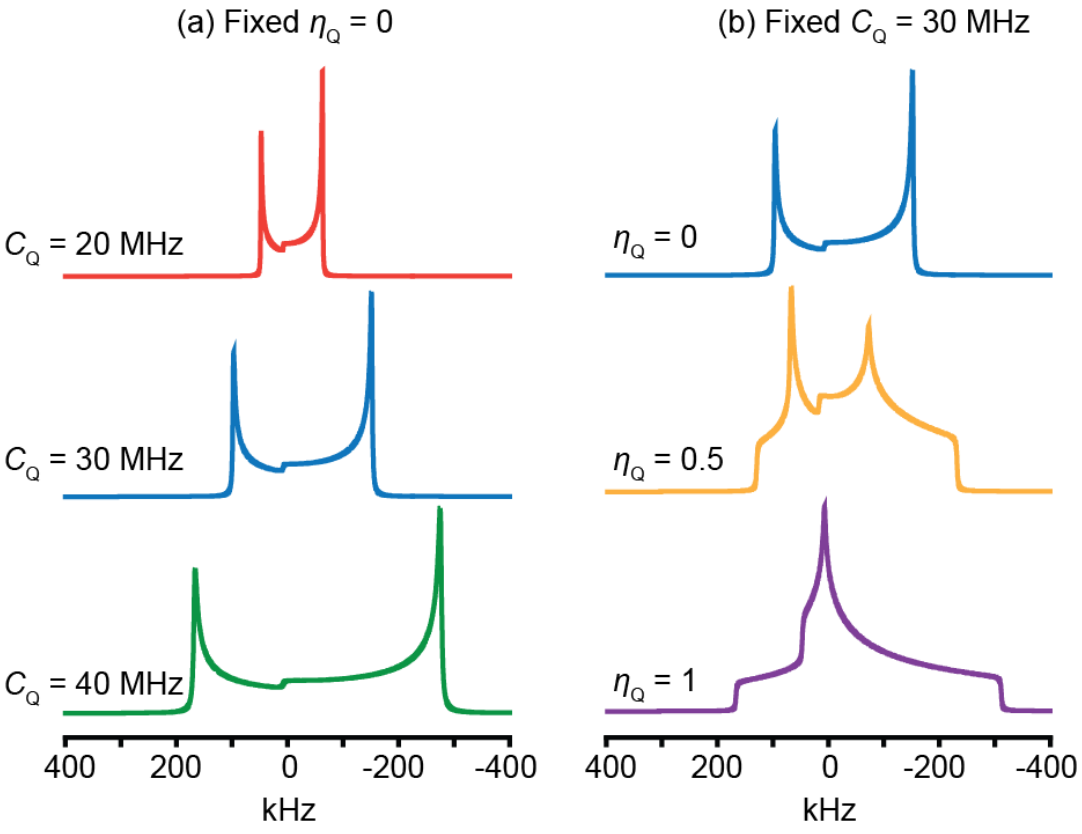

Figure 2-5: Examples of how C_Q (a) and η_Q (b) effect the NMR lineshape. All parameters were kept the same except the parameter labelled including the spectral window.

crystal at a single orientation. Thus, to reproduce the NMR static lineshape of a powder all orientations of the EFG PAS must be accounted for.

Examples of the quadrupolar interaction can be seen in Figure 2-5, the increase of C_Q in Figure 2-5(a) shows the linewidth increasing. Furthermore, if two nuclei of different spins such as 3/2 and 5/2 were to be compared for the same C_Q the 3/2 would be broader as shown in Equation 2-20 and 2-21 due to the second order perturbation being inversely proportional to I. However, it is clear η_Q indicates the location of shoulders and features which are characteristic of the interaction.

2.1.1.5 Convoluted Quadrupolar and CSA Interactions

Both quadrupolar and CSA interactions have been introduced. As stated previously both interactions can induce a broadening on the order of kilohertz (or even megahertz), due to the orientation dependence of the PAS with respect to B_0. Magic angle spinning (MAS) which will be expanded upon in Section 2.2.3 is of little use being unable to reach the rotation speeds required to increase resolution. Further complication arises when measuring nuclei which exhibit both interactions.[64,72]

Thus, the lineshapes generated are a convolution of the two interactions. Extraction of the NMR parameters out lined previously (δ_{iso}, Ω, κ, C_Q and η_Q) is not trivial. A general mathematical description of the lineshapes for a non-axially symmetric system was first reported by Baugher *et al.*[73] However, the treatment required the principle components of the two interactions to align within the same PAS. For systems where the PAS of both interactions is noncoincidence general derivations have been carried out by Power *et al.*[70] and Cheng *et al.*[71]

To simulate the NMR lineshape when PAS were noncoincident requires the relative orientation of the two interactions which are described by the Euler angles α, β and γ. Thus, eight parameters are required to define a NMR resonance measurement which contains both CSA and quadrupolar interactions (nine if the standard convention is used to define the CSA). Rotation conventions though have not been standardised and care is required when comparing reported Euler angles. For example

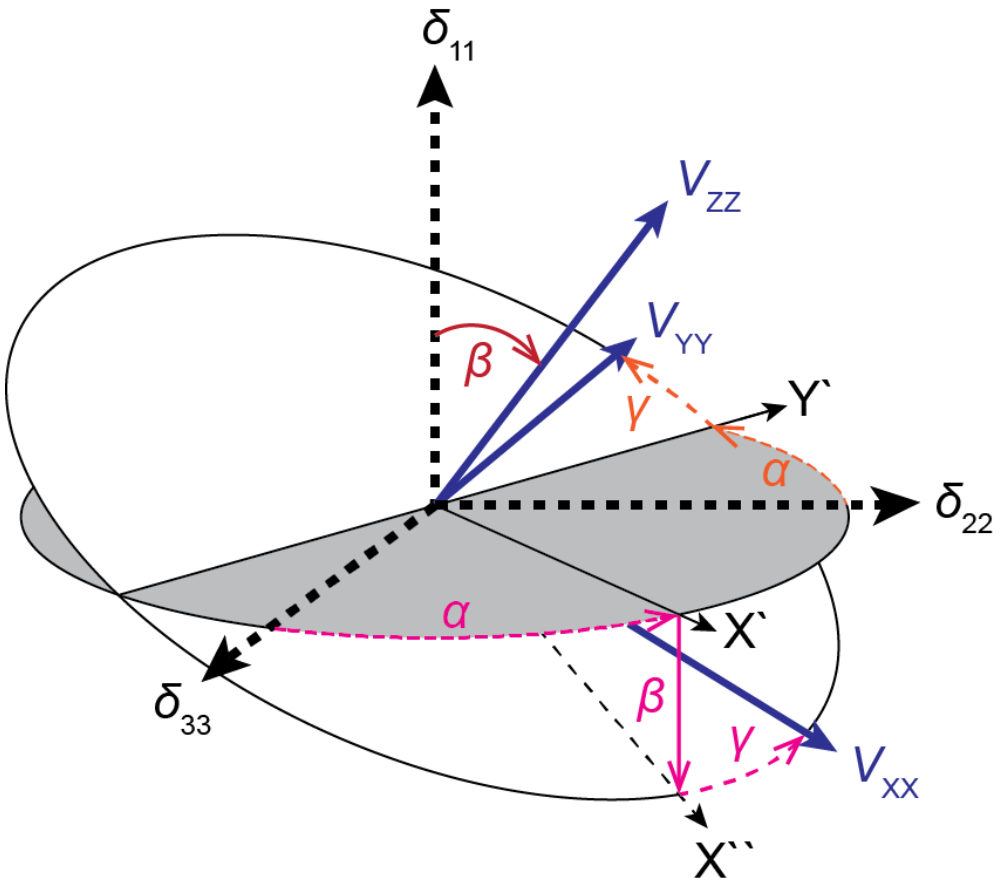

Figure 2-6: Rotation about axes of the order ZYZ' described by the Euler angles α, β and γ used to define the transformation between the CSA and quadrupolar principle axis systems. Thick axes highlight the two interaction systems and thin axes for intermediates. Rotations involving α are dashed with small gaps verses γ which uses dashes and gaps of equal size.

the derivations by Baugher *et al.*[73] and Power *et al.*[70] use the rotation convention about Z, then X and finally about Z', ZXZ', such the principle components only make a single reorientation. However, the simulation software used in this thesis (dmfit[68] and WSolids[74]) use a ZYZ' rotation convention which is the same as the simulation software SIMPSON[75], this convention is shown in Figure 2-6.

The rotations illustrated in Figure 2-6 describe the transformation from the CSA PAS to the quadrupolar PAS, the determination of which can be achieved by fitting the experimental lineshape via an iterative process (such as dmfit is capable of). The rotations of α (dashes with small gaps) and γ (equally sized dashes and gaps) align the minor axes of the CSA and quadrupole ellipsoids, there angles vary between 0˚

and 360˚. However, if one of the interactions is axially symmetric or close to ($\delta_{33} \approx \delta_{22}$ or $V_{YY} \approx V_{XX}$) then these rotations will have little to no effect on the NMR spectrum. Thus, exact determination can be difficult under the axial symmetric conditions. Furthermore, if β is close to zero or 180˚, α and γ would be reduced to a single rotation. Alignment of the largest components of each interaction can be seen to be described as a single rotation defined by β. Thus, β is the most sensitive of the Euler angles between the two interactions and due to symmetry varies between 0˚ and 180˚.

An example of a mixed quadrupole and CSA lineshape has been presented in Figure 2-7 where the field dependence of the two interactions is apparent. Through the simulation of spectra, the CSA and quadrupolar parameters have not been changed, the CSA contribution is presented above the convolution of the interactions and the quadrupole contribution below. Furthermore, all spectra are presented over a set arbitrary frequency range. Figure 2-7(a) shows a high field spectrum, where the CSA is the dominant interaction, demonstrating a lineshape similar to those seen in Section 2.1.1.3. Variation of the angles α, β and γ at high field demonstrates the dominance of the CSA which is observed from the lineshape maintaining the same general features. This can also occur for the quadrupole interaction at low magnetic fields. The angles α and γ are equal requiring a non-zero β to distinguish them. The simulations presented in Figure 2-7 have normalised intensities. This fails to demonstrate that the angle changes of α and γ also alter the l intensity of the spectrum.

A simulation at an intermediate field strength is shown in Figure 2-7(b), the CSA and quadrupole interactions are similar in magnitude. The comparable interaction strength is seen due to the loss of the characteristic CSA lineshape seen at high field. All Euler angles can also be seen to have a much greater effect on the spectrum where shoulders and features shift. The most drastic change though is seen in β where the angle drastically changes the lineshape. The simulation of β changed quickly increasing from 0˚, the transition from which generates a significant number of distinct lineshapes.

Finally, a low field simulation (Figure 2-7(c)) was carried out where the quadrupolar line width is greater than the CSA. As was observed with the Euler angles of the intermediate field strength all angles cause a significant perturbation of the NMR

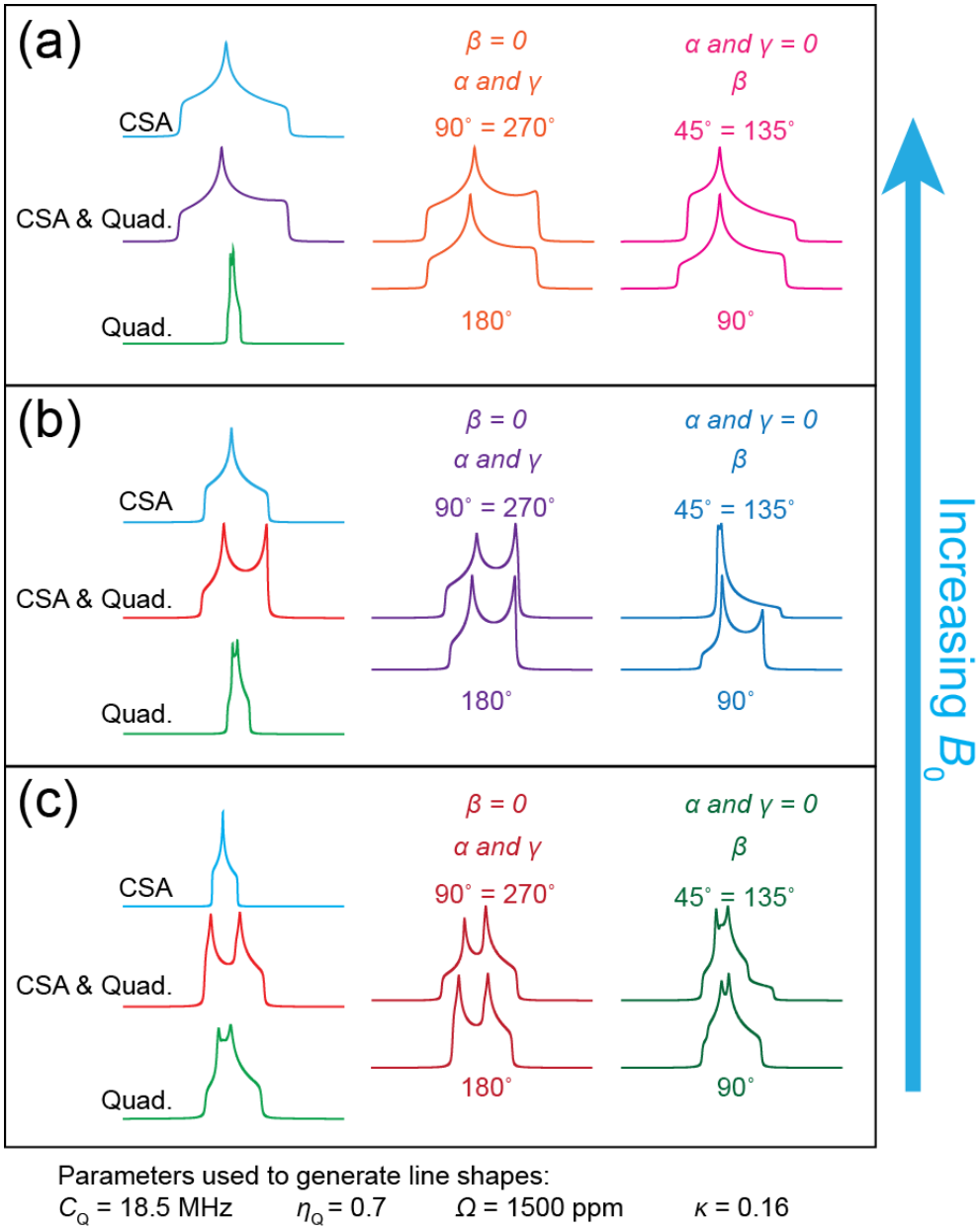

Figure 2-7: Examples of how a lineshape experiencing CSA and quadrupolar broadenings changes with field, (a) was simulated at 20.0 T, (b) at 11.7 T and (c) at 4.7 T. All simulations presented maintained the same frequency window so breadths of resonances can be discussed in terms of Hz. Finally, several Euler angles describing the rotation of the PAS for CSA to quadrupolar interactions and their effect on lineshape have been presented.

lineshape. This demonstrates the continued presence of the CSA interaction, as was observed in the ^{59}Co solid state NMR measurements undertaken in Chapter 3. Furthermore, with the low field simulation it is apparent the width of the resonance can also be effected by the Euler angles. Thus, as a quantitative analysis a direct comparison of line breadths of different materials may not necessarily indicate which has the larger CSA or quadrupolar interaction (as can be the case when a single interaction is present).

The extraction of NMR parameters from static NMR measurements of nuclei presenting both CSA and quadrupolar interactions is challenging. However, several observations from the theory can aid the analysis. Firstly, measurements at different magnetic fields is imperative, with eight parameters several false combinations are likely to be possible if a measurement at a single magnetic field was attempted. If only two fields were to be used, these should be at the greatest extremes possible to minimise one of the interactions in each case. Thus, from the field extremes estimates of the CSA (Ω and κ) and quadrupole (C_Q and η_Q) can be made. However, to determine accurate Euler angles an intermediate field would be desirable if the interactions have been successfully removed previously. The first angle to fit should be β, due to it being the most sensitive. An initial fit could then be attempted across the multifield spectra.

Utilising iteration approaches should be done carefully, high field spectra should use quadrupole parameters from the low field spectra (and *vice versa* for the CSA parameters). It is imperative to use the separate fields as constraints for one another, and the fitting of each field should be undertaken simultaneously. Thus, the relative parameters to be communicated amongst the data until all fields converge on a single set of values. Unfortunately, this process of using multiple field measurements as constraints is not a feature of any software normally used for these types of measurements, requiring a manual methodology. Finally, to iterate; the greater the range of intermediate fields the greater the accuracy the fittings would achieve.

2.1.1.6 J-Coupling and the Perturbation from Quadrupole Nuclei

Unlike the dipolar interaction mentioned previously, which acts through space, J-coupling (also referred to as scalar coupling, indirect coupling or spin-spin interaction) is a quantum mechanical through bond effect. The effect is typically only seen over a few chemical bonds, these must be covalent in nature.[64,69] The general form of the Hamiltonian $\widehat{H}_J$ between two spins I and S is given by:

$$\widehat{H}_J = h\boldsymbol{J}_{IS}\underline{I} \cdot \underline{S} \qquad \text{(Equation 2-25)}$$

Where $\boldsymbol{J}_{IS}$ is the scalar coupling which is a second rank tensor and thus has an anisotropic component. However, this is typically ignored due to the magnitude of the effects being so much smaller than the other interactions. Furthermore, observations of J-coupling in solid state are typically rare with anisotropies rarer.[76]

If J-coupling occurs between spins $I = 1/2$ and $S > 1/2$ the effects can be drastic. The first report of the theory of the coupling between a $I = 1/2$ and a quadrupolar nucleus was carried out by Menger *et al*.[77] A rigorous treatment has also been presented by Harris *et al*.[78] The reader is referred to these primary sources since each case observed can be treated with different sets of assumptions. For example, previous studies of ^{59}Co coupling to ^{15}N and ^{13}C[76,79] have required the full treatment reported by Harris *et al*.[78] However, this is carried out by the software WSolids and for an introduction to the effects seen in NMR a first order approximation is sufficient which is valid when,

$$\left|\frac{{C_Q}^2}{(4S(2S-1))^2\nu_S}\right| \ll 1. \qquad \text{(Equation 2-26)}$$

Where ν_s is the Larmor frequency of the coupled quadrupolar nucleus. Furthermore, it will be assumed there is no anisotropy in J_{IS}, this has been presumed in other experimental reports.[76,79,80] The spin-spin coupling often cannot be seen on the quadrupole nucleus; however, the $I = 1/2$ nucleus will produce a multiplet of $2S+1$ splittings. Thus, the frequency of a specific transition (ν_m) of the multiplet under

MAS is dependent on the indirect spin-spin coupling constant J and the full description is reported as:

$$\nu_m = \nu_{iso} - m_s J + \left(\frac{S(S+1)-3m_s^2}{S(2S-1)}\right)\left(\frac{3C_Q R_{DD}}{20\nu_s}\right)\left((3\cos^2\vartheta - 1) + \eta_Q \sin^2\vartheta \cos 2\varphi\right)$$

(Equation 2-27)

where m_s = -S, -S+1, …, S and ϑ and φ are the angles between V_{33} and the internuclear vector (**r**, see Section 2.1.1.2). The R_{DD} is the residual dipolar coupling constant with units of Hz, it has been shown[78] the interaction carries the quadrupole information which has the same field dependency as when directly observed. The R_{DD} is defined in Equation 2-28, such:

$$R_{DD} = \left(\frac{\mu_0}{4\pi}\right)\frac{\gamma_I \gamma_S h}{4\pi^2 r^3}\,. \qquad \text{(Equation 2-28)}$$

The residual dipolar coupling is also referred to as the direct coupling between the two nuclei. As a note for interpretation, J is usually written as ^{a}J(X, Y) and has units of Hz, the superscript a is the number of bonds between nuclei X and Y. Furthermore, from Equation 2-27, it is shown the separation of the splittings is proportional to C_Q and R_{DD}, this has been illustrated in Figure 2-8, where simulations of coupling to a S = 7/2 quadrupole nucleus is presented.

An ideal case where the C_Q is negligible (0 or sufficiently faraway) only pure J-coupling would be observed. This is shown initially in Figure 2-8 where each splitting of the multiplet is equally spaced by J. The quadrupolar nature of the splittings can be seen in the theoretical simulations, where powder average lineshapes are seen and are subject to shift due to the quadrupole interaction, as shown. Since the residual dipolar coupling transfers the quadrupole information an increase in R_{DD} (decrease in internuclear distance, see Equation 2-28) or an increase in C_Q have the same effect on the spectra.

It should be noted as the multiplet is perturbed the central lines shift the opposite direction to the outer ones and maintain the J spacing. This information is lost however when lines begin to cross one another as would happen after the final

simulation of Figure 2-8. Furthermore, the shifting of each line causes a "grouping" of the splittings which can occur at either high or low frequency side of the spectrum. The side the grouping occurs is indicated by the sign of the C_Q. If the product of $-C_Q R_{DD}/\nu_s$ is negative the grouping occurs at high frequency and low frequency if positive. The sign dependency of C_Q cannot be achieved from direct observation of the quadrupolar nucleus.[78]

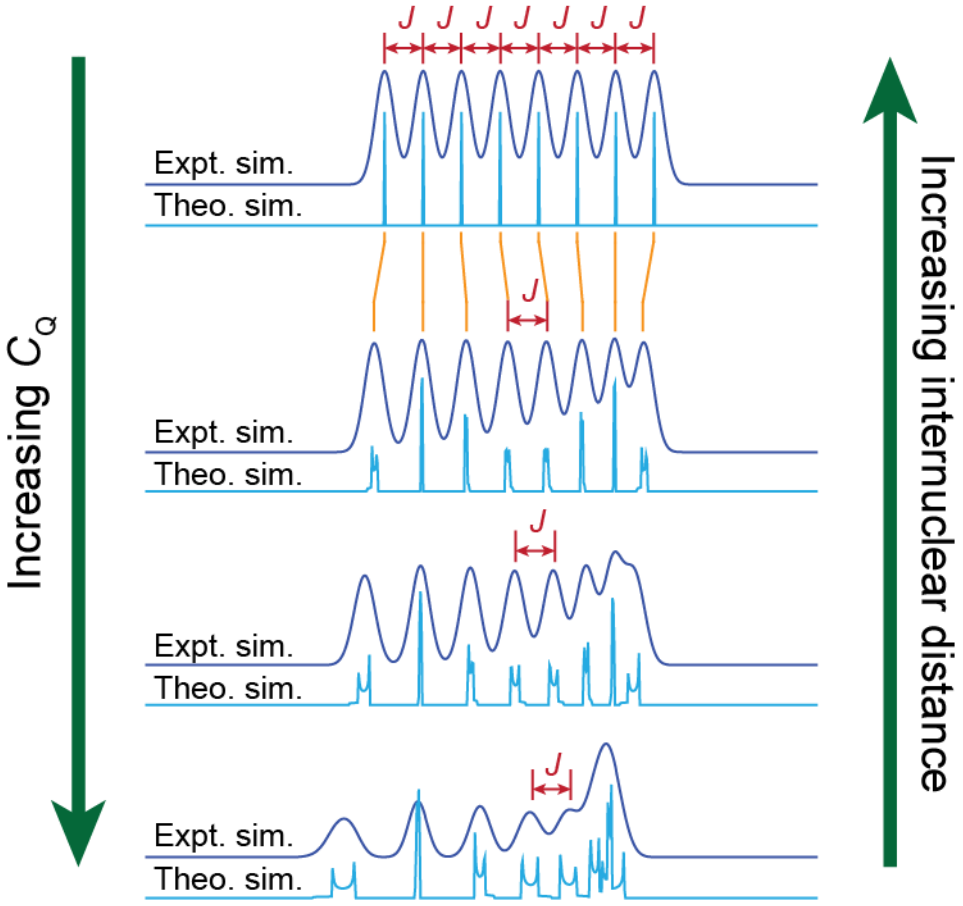

Figure 2-8: Schematic representation of spins $I = 1/2$ directly (dipole) and indirectly (spin-spin) coupled to an $S = 7/2$ nucleus. All spectra are simulations with the experimental simulations (Expt. Sim.) including line broadening to emulate actual measurements. Theoretical simulations (Theo. Sim.) demonstrate the quadrupolar lineshapes associated with each transition.

2.2 NMR Spectroscopy

The following sections aim to introduce some general NMR concepts and a concise approach to some of the general considerations required, when undertaking NMR experiments. Where the previous part of the chapter has focused on the individual spin, discussion will continue in terms of the bulk magnetisation and the vector model, whereby $I = 1/2$ will be considered as a vector. Thus, in a large external magnetic field, the sample of study contains a significant number of individual nuclei of spin I which align with or against B_0. The spin aligned with B_0 can be described by an overall vector $\underline{M}$, the bulk magnetisation. This is due to a population difference favouring the alignment of spin with B_0.

2.2.1 Excitation and the Radio Frequency Pulse

The application of a radiofrequency (rf) pulse at the Larmor frequency (ν_0) is orientated in the NMR experiment to transfer bulk magnetisation into the xy plane. Where the xy plane is perpendicular to the applied magnetic field. The application at

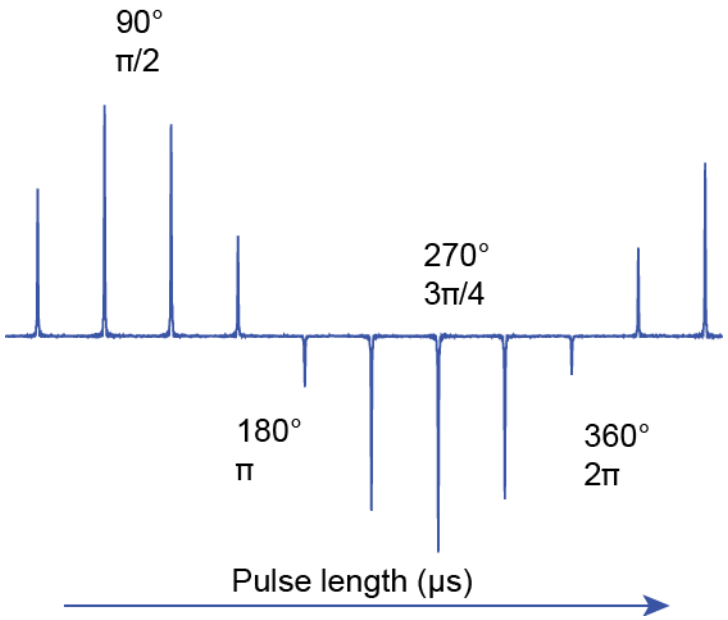

Figure 2-9: Example of an experimental nutation curve, inversion of the signal occurs at π and 2π.

ν_0 means that in the frame of the magnetisation, which would be precessing about B_0 at ν_0 cause the rf pulse to appear as a static field, defined as B_1, this is the rotating frame.

Depending on the period of time the magnetisation is subject to B_1 defines the flip angle, this is shown in Figure 2-9. To transfer the maximum magnetisation into the xy plane, which corresponds to the maximum signal, a $\pi/2$ pulse is require. However, experimentally the $\pi/2$ point can shift on the nutation curve.[64] Zero points are more robust to calibrate than a minima or maxima. Thus, calibration should be carried out via the π or 2π crossing points and a $\pi/2$ pulse can be calculated. The excitation width of a pulse is calculated from $1/(4\tau_p)$, where τ_p is the pulse length. As an example, a $\pi/2$ pulse which takes 1 μs will excite 250 kHz uniformly.[81]

The situation is slightly different for quadrupole nuclei. If the strength of the rf-field is much weaker than the quadrupole interaction then the nutation rate of the CT is increased. Thus, a shorter $\pi/2$ (selective) pulse would be required. This is found by first calibrating a non-selective pulse on a reference solution or reference material with a negligible C_Q. The non-selective pulse is then calculated by dividing the non-selective pulse length by the Rabi factor (I + ½). Thus, a $\pi/2$(non-selective) can be converted into a $\pi/2$(selective).[81]

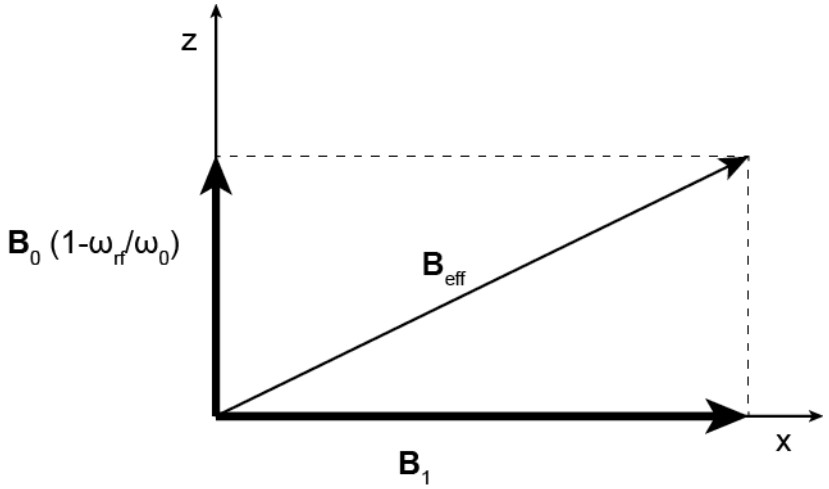

Figure 2-10: Illustrative diagram of the magnetic fields in the rotating frame upon the application of a rf pulse. Along z it is shown the Larmor frequency is reduced by the nutation frequency.

Typically, the resonance condition ($\nu_0 = \nu_{rf}$) may not be fully met. Deviation of the condition causes the magnetisation to be subject to multiple magnetic fields, as shown in Figure 2-10.[65] Thus, a remnant of B_0 remains in the rotating frame as resonance is lost and the magnetisation would precess about and effective field (B_{eff}). Whilst $\nu_{eff} \approx \nu_0$ the consequences are accountable for via the NMR spectrometer. However, if $\nu_{rf} >> \nu_0$ or $\nu_{rf} << \nu_0$ then it is apparent that the magnetisation will not tip into the xy plane and no signal would be achieved. This can cause phasing and partial excitation problems in wide line solid state NMR applications.[64,65,81]

2.2.2 Relaxation

After the application of the rf pulse the magnetisation will decay from the transverse plane back to the equilibrium alignment with B_0. The two main forms of relaxation to be considered are the longitudinal and transverse relaxation. These are described by the Bloch equations[64]:

$$\frac{dM_Z}{dt} = \frac{M_0 - M_z}{T_1} \qquad \text{(Equation 2-29)}$$

$$\frac{dM_x}{dt} = \frac{-M_x}{T_2}, \frac{dM_X}{dt} = \frac{-M_y}{T_2} \qquad \text{(Equation 2-30)}$$

Longitudinal relaxation describes the return of the magnetisation to the alignment with B_0 and is characterised by the time constant T_1. For the magnetisation to return to equilibrium the NMR experiments require a period of $5T_1$ between repeat measurements (transients). Thus, if many thousands of transients are required for a single measurement the experimental time can be extremely long. By varying the recycle delay (time between pulses) an estimation of $5T_1$ can usually be made if the signal arises quickly.[64,81]

The transverse relaxation describes how the magnetisation dephases in the xy plane (which is the plane the magnetisation is measured in), and is characterised by the time constant T_2. Experimentally this can be observed by the rate at which the free induction decay (FID), which is the NMR signal, declines (although this can be convoluted due to dipolar effects).[64] Broad NMR lines have a short T_2 and so the FID

decays rapidly and *vis versa* narrow lines have long T_2 and decay slowly. Truncation occurs when the recording of the signal is cut off before it has fully decayed. The effect is likely for very narrow NMR resonances should be avoided for accurate measurements.

2.2.3 MAS

Magic Angle Spinning (MAS) is a standard technique to increase the resolution of solid state NMR spectra. Reducible interactions include the dipolar coupling, CSA and first order quadrupole interactions, which, upon frame transformations from PAS systems to the Lab frame all contain a $3\cos^2\theta$-1 dependencies (to the first order). By physically spinning a sample at 54.74˚ (θ_R) to B_0 anisotropic interactions are averaged out. This is because the average orientation of a single PAS to the magnetic field (defined by θ) would average to zero upon whole rotor rotations as:

$$\langle 3cos^2\theta - 1\rangle = \frac{1}{2}(3cos^2\theta_R - 1) \times \frac{1}{2}(3cos^2\beta - 1) \qquad \text{(Equation 2-31)}$$

Where β is the angle from the PAS system to the rotation axis. Spinning speeds (v_r) must be larger than the interaction which is to be averaged out.[65] Thus, significant CSA or quadrupolar broadening cannot be reduced, such is the case with the ^{59}Co and ^{195}Pt NMR measurements undertaken in this thesis. The effect of MAS on second order interactions and higher effects is not being explored here, due to the predominant use to increase resolution of I = 1/2 measurements. However, effects of MAS are of significant importance to other experimental approaches.[69]

2.2.4 NMR Single Pulse and Echo Experiments

The most basic NMR experiment is the single pulse experiment and in principle follows the outline of the previous sections. An rf pulse is used to transfer the magnetisation into the xy plane and the decay back to equilibrium produces a current in the NMR coil, observed as an FID. From the time resolved FID a Fourier transform is used to convert data into the frequency domain. The frequency resolved spectrum is referenced to a standard as discussed in Section 2.1.1.3 converting the NMR scale

to ppm. Thus, measurements at different magnetic fields and from different research groups can be compared.[64]

However, distortion of the NMR spectrum can occur from experimental limitations. When T_2 is short, as is the case with broad lines experiencing significant CSA or quadrupolar interactions, the first few data points of the FID are vital to the spectrum. These can be lost or distorted due to the dead time of the spectrometer. Where the dead time is a period after pulse generation when NMR acquisition can't occur prior to the receiver turning on. Furthermore, after the application of an rf pulse mechanical and re-radiation effects can cause significant distortion of the early part of the FID (ringing). Both effects can significantly reduce the accuracy of broad resonances measurements.[64,81]

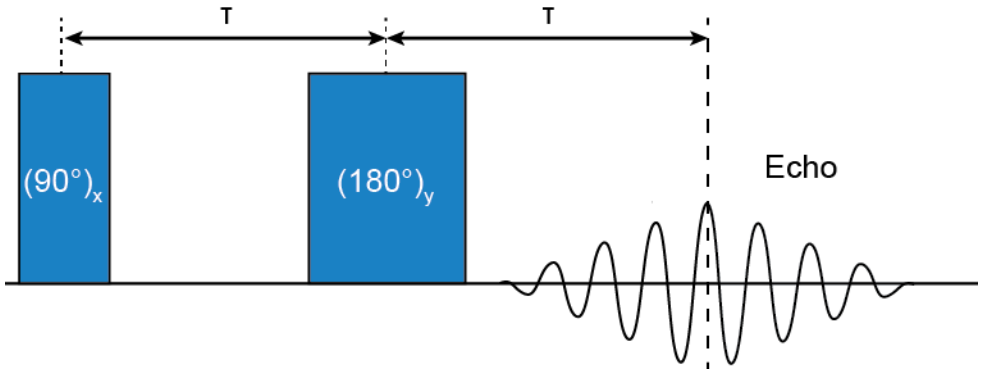

Figure 2-11: Spin-echo pulse sequence consisting of two radio frequency pulses which tip the magnetisation 90° allows for the magnetisation to evolve for a period τ prior to a refocusing 180° pulse.

To acquire an undistorted FID of broad resonances an echo experiment can be used as depicted in Figure 2-11. For a spin, $I = 1/2$ nucleus the 90°-τ-180° sequence shown acts to firstly place magnetisation in the xy plane, allow it to dephase with T_2 before using a 180° to refocus the magnetisation. The refocusing causes the beginning of the FID to appear a time period τ after the 180° pulse. Experimentally a whole echo as depicted will not necessarily be acquired, however, some of the magnetisation build up prior to τ should be obtained to ensure accurate determination.[81]

For quadrupolar nuclei, a solid echo pulse sequence should be used.[7,64] This second echo scheme replaces the 180° pulse with a 90° pulse. The shorter second pulse

allows for a broader excitation in conjunction with selective pulses. It should be noted it care is to be taken if quantitative information is required with echoes.[82]

2.2.5 Variable Offset Cumulative Spectroscopy

When the interactions cause the NMR resonance to exceed the excitation profile of the pulses being used a wide line method is required. Variable offset cumulative spectroscopy (VOCS) is an accurate way to reconstruct broad lineshapes. The method relies on stepping the frequency offset of the pulse until the entire lineshape can be equally excited and a reconstruction can be made from the individual slices. To minimise any distortions within the lineshape these frequency steps should be no more than 75% of the excitation profile apart. Furthermore, the probe tuning should be constant across the acquisition region, thus, the greatest drawback is the requirement for retuning of the NMR probe between slices.[72,83]

2.2.6 CPMAS

Acquisition of low natural abundance nuclei such as ^{13}C, ^{15}N and ^{29}Si can be difficult, this can be in conjunction with long T_1 as well. A cross polarisation magic angle spinning (CPMAS) experiment can be used to enhance signal and use the T_1 of the protons. The experiment transfers polarisation from the abundant and sensitive ^{1}H nucleus to the less abundant X nucleus, as shown in Figure 2-12.[65] The experiment transfers ^{1}H polarisation into the xy plane, then by matching a spin lock pulse on the proton channel with a contact pulse on the X channel magnetisation can be transferred. For the transfer to occur the Hartmann-Hahn match[65] condition must be met which requires both nuclei to experience the same nutation this is experimentally set up using B_1 the magnetic field applied by the rf pulse, such:

$$\gamma_H B_1\left(^{1}H\right) = \gamma_X B_1(X) \qquad \text{(Equation 2-32)}$$

The magnetisation transfer occurs via the dipolar coupling, thus if the interaction is fully removed by MAS the CP will not occur. Furthermore, the transfer is a through space process and depends on the separation of protons and target nucleus. The signal

is detected on the X channel; however, the signal intensity is no longer proportional to the number of X nuclei but rather it reflects the number of nearby ^{1}H nuclei. Furthermore, decoupling is applied to the proton channel during acquisition, this constant irradiation removes heteronuclear dipolar coupling ensuring a well resolved X spectrum. Thus, CPMAS allows for an enhancement of dilute nuclei and measurements can be repeated as a function of the proton T_1.[64]

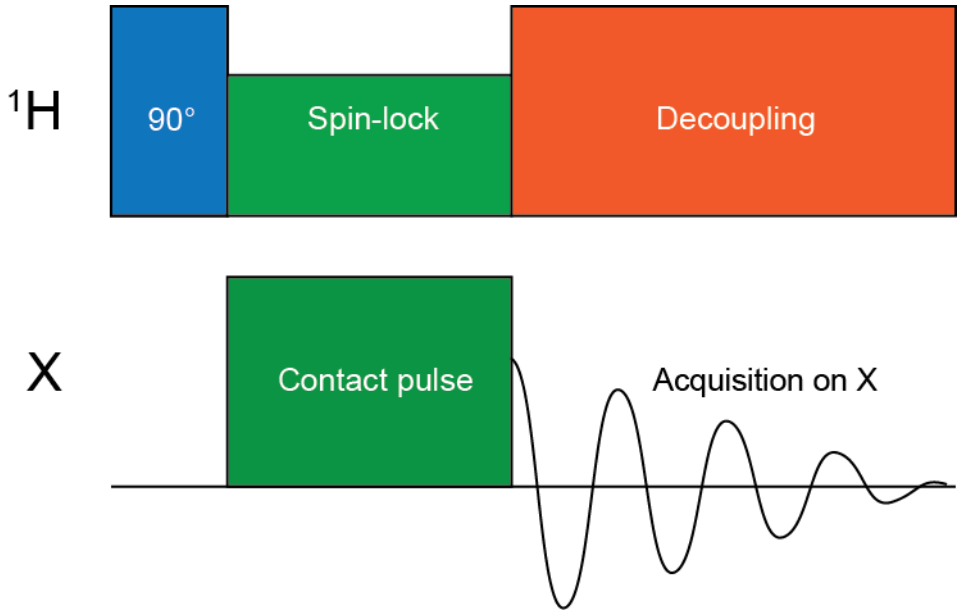

Figure 2-12: Pulse diagram of a cross polarisation MAS experiment which transfers magnetisation from ^{1}H to another nucleus X which can then be observed.

Chapter 3 Solid State Characterisation of Co(III) Ammine Complexes

3.1 Background

As outlined previously (Section 1.2.2) Johnson Matthey have reported a method of making highly dispersed cobalt (HDC) catalysts for Fischer Tropsch (FT) reactions from an ammine carbonate complex. Although the catalyst has high metal loadings, high activity and good dispersion it was not understood how the cobalt oxide nanoparticles evolve from the ammine complex.[39-41]

The synthesis liquor is known to be a complex and dynamic system which makes deconvolution of the process difficult. However, pure isolated solid state materials can be extracted directly from the synthesis. Furthermore, Figure 1-1 proposed a hypothetical route to cobalt oxide via Werner's complex which can be made stepwise. These individual steps are suited to solid state analysis yielding further pure single complex materials with additions made from relevant literature[84-86]. The suite of solid state samples relevant to the HDC liquor have been characterised by multinuclear NMR and where possible single crystal X-ray diffraction (courtesy of the national facility at Southampton University).

The solid-state NMR characterisation of the nine Co(III) ammine complexes have aimed to establish the variation of δ_{iso} with oxo coordination. Furthermore, the varying counter ion and types of oxo coordination should allow for a variation of NMR parameters. It is important to understand the potential for variation in δ_{iso} as it is expected direct comparison of solid state to solution state will not be exact. The isolation of complexes in solid state also enables the characterisation of ligands which

aids both explaining ^{59}Co observations in solid state and informs ligand substitution reactions in solution state.

The complexes of interest have been studied via ^{59}Co, ^{15}N, ^{13}C and ^{1}H NMR to generate a usable chemical shift reference scale which can be compared to industrial samples where the precise structure was previously unknown. Utilising ^{59}Co NMR provides several key advantages when comparing similar compounds. Firstly, its significant chemical shift range of 20 000 ppm means slight changes in the nuclear environment are easily detected. Although, chemical shift anisotropy (CSA, see Section 2.1.1.3) significantly broadens NMR signals it is sensitive to chemical bonding. Finally, the ^{59}Co nucleus possess a spin of $I = 7/2$ and a quadrupole moment of 420 mb, therefore, is subject significant quadrupolar broadening of the central transition (-1/2 to 1/2).[87] The combination of these two interactions is a convoluted lineshape which can be on the order of kilohertz to megahertz in width.[7] However, as discussed previously (Section 2.1.1.5) deconvolution of the NMR parameters provides an extremely sensitive probe into the chemical bonding, symmetry and insight into the second order coordination sphere.[87]

By utilising ^{1}H, ^{13}C and ^{15}N solid state NMR insight into ligands and surrounding effect allows for a detailed discussion of the complexes. Of the NMR active nuclei ^{15}N, which has a spin $I = 1/2$, has been proven used previously for monitoring structural changes.[24] However, with a low natural abundance of only 0.368% and a gyromagnetic ratio of -2.7126 (~1/10th that of ^{1}H) acquiring spectra at natural abundance is challenging.[88] Similarly, ^{13}C has a low natural abundance of only 1.07% but a larger gyromagnetic ratio ($\gamma = 6.7283 \times 10^7$ rad T^{-1} s^{-1}). Utilising the sensitive ^{1}H nuclei (which has a $\gamma = 26.7522 \times 10^7$ rad T^{-1} s^{-1} and a natural abundance of 99.99%) cross polarisation MAS (CPMAS) can be used to enhance the ^{15}N and ^{13}C signals.[88]

The study of Co(III) complexes via ^{59}Co solid state NMR is limited especially with the application to ammine complexes where only monoclinic structures have been analysed.[80,89] Despite the convoluted nature of ^{59}Co NMR the analysis of static

lineshapes has been proven effective at providing more information than is obtainable via solution state where an isotropic interactions are removed due to random tumbling. In solution the magnitude of the quadrupolar interaction has been estimated from the NMR linewidths[90], however it has been demonstrated by Medek *et al*. that this is not necessarily an accurate method.[91]

Previous ^{59}Co solid state NMR studies have been limited, two studies have characterised comparable ammine complexes previously: A general study of Co(III) complexes by Kirby *et al*[89] as well as a second isomerisation study by Ooms *et al*.[80] However, these have typically been restricted in their variation of external magnetic fields (the importance of which was discussed in Section 2.1.1.5). Thus, any previously reported materials will benefit from the greater range of magnetic fields presented here. Furthermore, all previous studies have been limited to monomeric complexes, Werner's complex has not been seen reported via ^{59}Co solid state NMR previously.

3.2 Experimental

3.2.1 Synthesis

The Co(III) carbonatotetramminecobalt(III) complexes studied were as follows: $[Co(NH_3)_4CO_3]Br$, $[Co(NH_3)_4CO_3]NO_3{\cdot}0.5H_2O$, $[Co(NH_3)_4CO_3](SO_4)_{0.5}{\cdot}1.5H_2O$ these were prepared via methods reported previously which report that the counter ion can be controlled by the Co(II) salt used.[42] An extensive catalogue of complexes can be found in the Inorganic Syntheses series book series, where the majority of the complexes characterised here can be found. Synthesis of the $[Co(NH_3)_4CO_3](SO_4)_{0.5}{\cdot}1.5H_2O$ was carried out with ^{13}C and ^{15}N labelled $(NH_4)_2CO_3$ and ^{15}N labelled (NH_3). An unlabelled carbonatotetramminecobalt(III) sulphate sample was then converted into Werner's complex $[Co((\mu{-}OH)_2Co(NH_3)_4)_3](SO_4)_3{\cdot}9H_2O$ during the conversion samples of $[Co(NH_3)_4(H_2O)_2](SO_4)_{1.5}{\cdot}1.5H_2O$ were also obtained.[43] An alternative Werner's complex preparation can also be found in Inorganic Syntheses.[86]

From $[Co(NH_3)_4(H_2O)_2](SO_4)_{1.5}\cdot 1.5H_2O$ preparation of $[Co(NH_3)_4(H_2O)(OH)](BF_4)_2$ and $[(NH_3)_4Co(\mu\text{-}OH)_2Co(NH_3)_4](BF_4)_4$ were to be produced from a method found in Inorganic Syntheses with tetrafluoroborate in place of sodium dithionate.[92] However, washing is thought to have removed the BF_4. From ICP and CHN carried out internally at Johnson Matthey, these complexes are of the form $[Co(NH_3)_4(H_2O)(OH)](SO_4)\cdot H_2O$ (found: 21.3% Co, 20.3% N, 6.2% H, 11.6% S, calculated: 22.0% Co, 20.6% N, 5.8% H, 11.6% S) and $[Co(NH_3)_4(\mu\text{-}OH)_2](SO_4)_2\cdot H_2O$ (found: 23.7% Co, 22.5% N, 5.7% H, 12.9% S, calculated: 23.9% Co, 22.5% N, 5.4% H, 12.8% S).

A sample of red precipitant was isolated from each of the HDC synthesis routes (from $CoCO_3$ or cobalt metal) used in the batch manufacture of cobalt nanoparticles. Using a cobalt metal precursor, a mixture of 200 ml of water and 280 ml of ammonium hydroxide solution was used to dissolve 40.5 g (0.42 mol) of ammonium carbonate prior to the addition of 15 g (0.26 mol) of cobalt metal powder. Submersion of a plastic tube allowed for air to be gently bubbled through the solution overnight whilst being stirred (requiring an overhead stirrer due to the magnetic nature of cobalt metal). Oxidation of the solution was achieved characterised by a red/purple solution, and at this stage a solid of the same colour precipitated out which shall be shown to be $[(Co(NH_3)_3)_2(\mu\text{-}OH)_2(\mu\text{-}CO_3)](CO_3)\cdot 5H_2O$. Once collected and excess solution was filtered off using a Buchner funnel and the sample was left to dry in the ambient room conditions.

The method using cobalt carbonate was carried out using 22.5 g (0.23 mol) of ammonium carbonate dissolved in 225 mL of ammonium hydroxide and 200 ml of water. 24.6 g (0.21 mol) of cobalt carbonate was added turning the solution brown as it dissolved. Oxidation of the solution used 30 ml (0.265 mol) of hydrogen peroxide added drop wise over several minutes changing the colour to a red/purple whilst producing effervescence. The reaction was allowed to complete over the course of an hour with stirring maintained throughout. Solid precipitant was obtained by stopping the stirring although yield was reduced compared to the metal prep. Treatment of the solid was the same as with the sample from the metal preparation.

3.2.2 Single Crystal XRD

Single crystal measurements were undertaken by the National Crystallography Service at the University of Southampton. The following experimental details were provided for the structures presented. Data collection was collected on a Rigaku AFC12 diffractometer equipped with an enhanced sensitivity (HG) Saturn724+ CCD detector mounted at the window of an FR-E+ *SuperBright* rotating anode generator (Mo Kα, λ = 0.71075 Å) with VHF *Varimax* optics (70 μm focus).[93]

CrysalisPro[3] software was used for data processing. Unit cell parameters in all cases were refined against all data. The crystal structures were then solved by direct methods with SHELXT[4] and refined on F_o^2 by full-matrix least-squares refinements using ShelXL[5] within the OLEX2 suite.[94]

3.2.3 Solid State NMR

To extract robust and accurate NMR parameters from the static broad line ^{59}Co measurements the greatest span of magnetic fields possible is required to deconvolute the CSA and quadrupolar contributions, including their relative orientations (see Section 2.1.1.5). Thus, measurements were carried out at 7.1 T (Varian Infinity Plus-300), 11.7 T (Bruker Avance II+-500), 14.1 T (Bruker Avance II+-600) and 18.8 T (Varian CMX Infinity Plus-800) operating at the corresponding ^{59}Co Larmor frequencies of 71.59, 118.65, 142.23 and 201.73 MHz. Two Bruker static solids probes (high and low field variants) were used with a 5 mm coil orientated perpendicular to the magnetic field; these probes use changeable capacitors to allow for use on a range of systems. All experimental ^{59}Co data was acquired using a solid echo pulse sequence θ-τ- θ-τ-(acquire) where θ = π/2 (selective pulse) and τ was 30 μs at ambient temperature. Experiments were referenced to 0 ppm with a 0.56 mol/L aqueous solution of $K_3Co(CN)_6$, the IUPAC standard reference.[88] A non-selective 4 μs π/2 pulse ($\tau_{p(nonsel)}$) was calibrated on the primary ^{59}Co reference and then a selective pulse ($\tau_{p(sel)}$) was calculated for ^{59}Co using the Rabi factor (see Section 2.2.1).

To characterise the ^{59}Co environments of the Co(III) complexes via NMR require accurate determination of the CSA and the electric field gradients (EFG) tensors described by the associated parameters δ_{iso}, C_Q, η_Q, Ω, κ and the Euler angles α, β and γ (see section 2.3.1 for definitions). Due to the convoluted nature of the quadrupole and CSA interactions further complication arises in the analysis, however, the magnetic field dependencies for each interaction are different (CSA dominates high field and quadrupole dominate the low field). Thus, for robust analysis spectra over the greatest range of B_0 possible are required.

However, the challenge extends further still, as for accurate determination of the NMR parameters via lineshape analysis an undistorted central transition (-1/2 to 1/2) must be obtained. This becomes difficult if the observable signal spans a range greater than the excitation profile being used (for a 1 μs selective π/2 pulse it can be estimated ~250 kHz is uniformly excited). Variable Offset Cumulative Spectroscopy (VOCS) where by the frequency offset is stepped (uniformly) and a set of sub spectra are collected which can then be used to reconstruct an undistorted lineshape.[7,32,33,95]

The ^{13}C and ^{15}N cross polarisation, magic angle spinning (CPMAS) data were acquired using a 11.7 T Bruker Avance II+-500 spectrometer with a Bruker two channel 4 mm MAS triple resonance probe used. For both ^{13}C and ^{15}N measurements samples were packed into 4 mm rotors and spun at 12 kHz. Both experiments used a ^{1}H π/2 pulses = 2.5 μs with contact times of 1 ms and 5 ms, respectively, which could be set up on a doubly labelled (^{13}C and ^{15}N) complex of $[Co(NH_3)_4(H_2O)_2](SO_4)_{1.5}$, during the acquisition high power spinal ^{1}H decoupling was used.[96] ^{13}C was referenced such that Me_4Si was 0 ppm and ^{15}N was referenced to $MeNO_2$ at 0 ppm using singly labelled histidine (-191 ppm).

Corresponding ^{1}H measurements were undertaken at 14.1 T on a Bruker Avance II+-600 spectrometer. Bruker 2.5 mm HX and HXY MAS NMR probes were used which enabled MAS frequencies (ν_r) of 30 kHz. Pulses were calibrated on α-Alanine which was a secondary reference, where the CH_3 peak was calibrated to 1.1 ppm with respect to Me_4Si IUPAC reference.[88]

3.3 Results and Discussion

3.3.1 Single Crystal Measurements of Selected Complexes

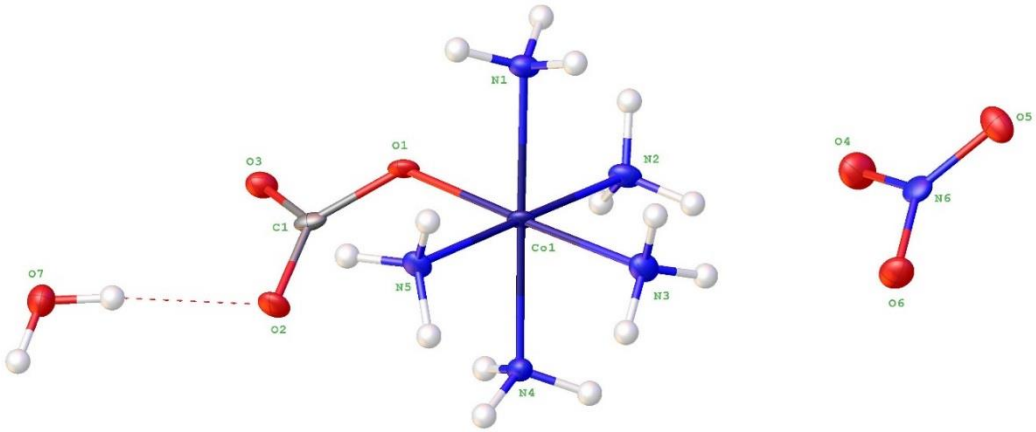

Figure 3-1: Molecular structure of $[Co(NH_3)_5CO_3]NO_3 \cdot H_2O$ atomic displacement ellipsoids represent 50% probability.

Table 3-1: Selected bond lengths and bond angles for $[Co(NH_3)_5CO_3]NO_3 \cdot H_2O$. All bond lengths and angles with protons not listed were found to be N–H of 0.89 Å and an H–N–H angle of 109.5 ° respectively.

Bond lengths (Å)		Bond lengths (Å)	
Co1–O1	1.939(7)	O2–C1	1.272(13)
Co1–N1	1.979(9)	O3–C1	1.265(12)
Co1–N2	1.976(10)	O4–N6	1.255(13)
Co1–N3	1.958(8)	O5–N6	1.252(13)
Co1–N4	1.942(10)	O6–N6	1.258(12)
Co1–N5	1.954(9)	O7–H7A	0.8501
O1–C1	1.334(13)	O7–H7B	0.85
Bond Angles (°)		Bond Angles (°)	
O1–Co1–N1	88.0(3)	N4–Co1–N5	91.2(4)
O1–Co1–N2	85.9(4)	N5–Co1–N1	89.2(4)
O1–Co1–N3	177.8(4)	N5–Co1–N2	179.2(5)
O1–Co1–N4	92.5(3)	N5–Co1–N3	88.2(4)
O1–Co1–N5	93.9(4)	C1–O1–Co1	128.8(6)
N2–Co1–N1	91.6(4)	O2–C1–O1	120.7(9)
N3–Co1–N1	91.5(4)	O3–C1–O1	116.3(8)
N3–Co1–N2	92.0(4)	O3–C1–O2	123.1(10)
N4–Co1–N1	179.4(4)	O4–N6–O6	119.2(12)
N4–Co1–N2	88.1(4)	O5–N6–O4	119.7(10)
N4–Co1–N3	88.0(4)	O5–N6–O6	121.1(11)

When possible, single crystal measurements were undertaken to validate the synthesis products. However, this was not always possible due to crystallite size and structural integrity of the samples which were often affected by disorder. Previous studies of similar complexes have been reported[75,76], however some of these are ~50 years old more updated data, characterisation and insights are required.

An ORTEP diagram of the $[Co(NH_3)_5CO_3]NO_3{\cdot}H_2O$ is presented in Figure 3-1, the structure has a monoclinic crystal system and a $P2_1$ space group. From the synthesis, the complex was thought to contain one H_2O per two cations, however, this was not seen in the single crystal measurements here or in powder measurements reported previously.[97] The five ammine ligands and monodentate carbonate ligand sit in a distorted octahedra with variation on all six ligands, as seen in Figure 3-1. The bond lengths are summarised in Table 3-1, Co–N ranged from 1.942–1.979 Å and the Co–O bond was 1.939 Å, demonstrating similar distances to each other. Although the immediate coordination with the Co nucleus is in good agreement with the structure proposed by Zhu *et al.*[97] there are discrepancies in the bond distances of the monodentate carbonate ligand due to the limitations of the *ab initio* X-ray powder diffraction technique used.

In the previously reported structure for $[Co(NH_3)_5CO_3]NO_3{\cdot}H_2O$ the C–O bonds range from 1.222 Å to 1.322 Å. However, as seen in Table 3-1 from single crystal measurements a range of 1.265 Å to 1.334 Å was determined. The O–C–O angles are also more obtuse between the unbound oxygen than in the previous reporting.[97] Over all, the direct single crystal measurement presented here will be used for continued comparisons.

Table 3-2: Hydrogen bonding for $[Co(NH_3)_5CO_3](NO_3){\cdot}H_2O$ shown in Figure 3-1.

D–H···*A*	*d*(*D*–H) (Å)	*d*(H···*A*) (Å)	*d*(*D*···*A*) (Å)	∠(*D*H*A*) (°)
O7–H7A···O2	0.85	1.95	2.796(11)	175.0
O7–H7B···O4^{i}	0.85	1.95	2.796(12)	175.3
Symmetry transformations used to generate equivalent atoms: (i) –x,y–1/2,–z				

Table 3-3: Selected bond lengths and angles for $[Co(NH_3)_4CO_3]_2(SO_4)\cdot 3H_2O$ shown in Figure 3-2 protons not listed were found to be N–H of 0.91 Å and an H–N–H angle of 109.5 ° respectively.

Bond lengths (Å)		Bond lengths (Å)		Bond lengths (Å)	
Co2–O4	1.9030(13)	Co1–O1	1.9029(13)	S1–O7	1.4723(14)
Co2–O5	1.9199(14)	Co1–O2	1.9178(13)	S1–O8	1.4717(14)
Co2–N5	1.9608(16)	Co1–N1	1.9620(15)	S1–O9	1.4767(14)
Co2–N6	1.9538(15)	Co1–N2	1.9534(16)	S1–O10	1.4945(14)
Co2–N7	1.9474(16)	Co1–N3	1.9441(16)	O12–H12A	0.8699
Co2–N8	1.9655(18)	Co1–N4	1.9519(17)	O12–H12B	0.8701
Co2–C2	2.3238(19)	Co1–C1	2.3268(19)	O13–H13A	0.87
O4–C2	1.318(2)	O1–C1	1.320(2)	O13–H13B	0.8701
O5–C2	1.317(2)	O2–C1	1.324(2)	O11–H11A	0.8701
O6–C2	1.236(2)	O3–C1	1.228(2)	O11–H11B	0.87
Bond Angles (°)		Bond Angles (°)		Bond Angles (°)	
O4–Co2–O5	69.03(6)	O6–C2–O5	125.31(17)	O3–C1–O1	124.37(18)
O4–Co2–N5	88.48(6)	O1–Co1–O2	69.21(6)	O3–C1–O2	125.26(18)
O4–Co2–N6	89.03(6)	O1–Co1–N1	88.64(6)	O7–S1–O9	109.00(8)
O4–Co2–N7	168.75(6)	O1–Co1–N2	90.59(6)	O7–S1–O10	109.89(8)
O4–Co2–N8	98.12(6)	O1–Co1–N3	166.93(6)	O8–S1–O7	110.37(8)
O4–Co2–C2	34.54(6)	O1–Co1–N4	97.00(6)	O8–S1–O9	110.43(8)
O5–Co2–N5	89.73(6)	O1–Co1–C1	34.55(6)	O8–S1–O10	108.68(8)
O5–Co2–N6	88.93(6)	O2–Co1–N1	91.19(6)	O9–S1–O10	108.45(8)
O5–Co2–N7	99.74(6)	O2–Co1–N2	90.66(6)	-	-
O5–Co2–N8	167.13(6)	O2–Co1–N3	97.76(6)	-	-
O5–Co2–C2	34.52(6)	O2–Co1–N4	166.18(6)	-	-
N5–Co2–N8	89.19(7)	O2–Co1–C1	34.67(6)	-	-
N5–Co2–C2	87.78(6)	N1–Co1–C1	89.25(6)	-	-
N6–Co2–N5	177.47(7)	N2–Co1–N1	177.60(7)	-	-
N6–Co2–N8	91.63(7)	N2–Co1–C1	91.41(6)	-	-
N6–Co2–C2	89.90(6)	N3–Co1–N1	90.63(7)	-	-
N7–Co2–N5	92.27(7)	N3–Co1–N2	90.63(7)	-	-
N7–Co2–N6	90.08(7)	N3–Co1–N4	96.04(7)	-	-
N7–Co2–N8	93.12(7)	N3–Co1–C1	132.39(7)	-	-
N7–Co2–C2	134.25(7)	N4–Co1–N1	89.34(7)	-	-
N8–Co2–C2	132.61(7)	N4–Co1–N2	88.50(7)	-	-
C2–O4–Co2	90.49(11)	N4–Co1–C1	131.55(7)	-	-
C2–O5–Co2	89.77(11)	C1–O1–Co1	90.58(11)	-	-
O4–C2–Co2	54.97(9)	C1–O2–Co1	89.82(11)	-	-
O5–C2–Co2	55.71(9)	O1–C1–Co1	54.86(9)	-	-
O5–C2–O4	110.61(16)	O1–C1–O2	110.35(16)	-	-
O6–C2–Co2	175.39(14)	O2–C1–Co1	55.51(9)	-	-
O6–C2–O4	124.03(17)	O3–C1–Co1	177.07(14)	-	-

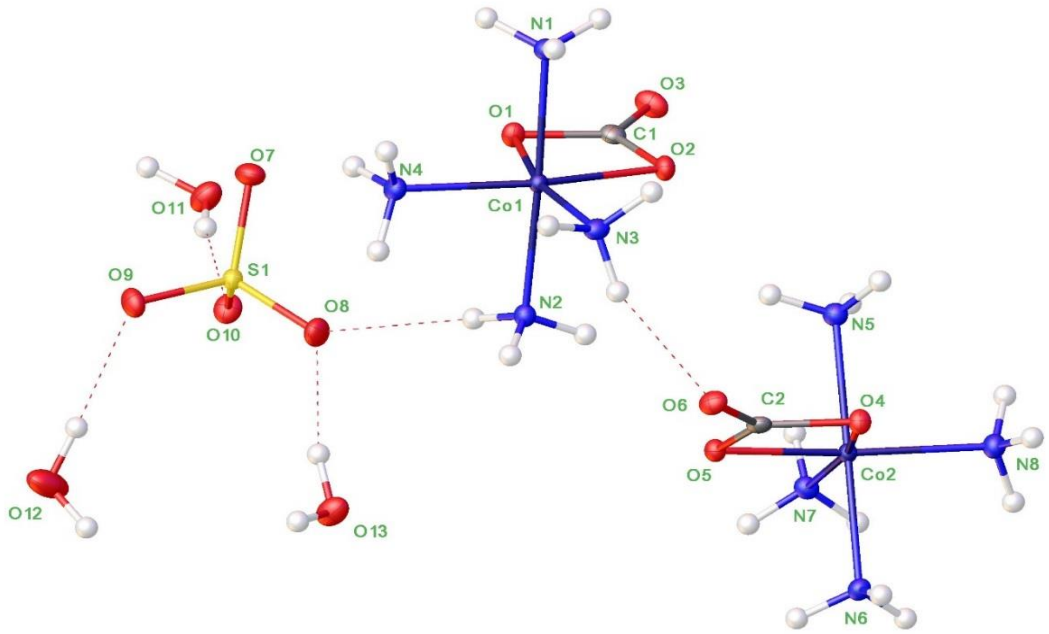

Figure 3-2: Molecular structure of $[Co(NH_3)_4CO_3]_2(SO_4)\cdot 3H_2O$. Atomic displacement ellipsoids represent 50% probability.

Finally, the H-bonding has been shown in more detail than the previous reporting and is summarised in Table 3-2. This further corroborates the role of linking crystallographic water with the anion, however, any ammine bonding with these units was not obtained.

Figure 3-2 shows the crystal structure for the charge neutral complex of $[Co(NH_3)_4CO_3]_2(SO_4)\cdot 3H_2O$, referred to from this point forwards as $[Co(NH_3)_4CO_3](SO_4)_{0.5}\cdot 1.5H_2O$. The crystal occupies the $P2_1/c$ space group. The

Table 3-4: Hydrogen bonding for $[Co(NH_3)_4CO_3]_2(SO_4)\cdot 3H_2O$ shown in Figure 3-2.

D–H···*A*	*d*(*D*–H) (Å)	*d*(H···*A*) (Å)	*d*(*D*···*A*) (Å)	∠(*DHA*) (°)
N3–H3C···O6	0.91	1.99	2.860(2)	158.6
O12–H12A···O9	0.87	1.91	2.778(2)	174.4
O12–H12B···O11^{i}	0.87	2.01	2.825(2)	155.0
O13–H13A···O8	0.87	1.88	2.739(2)	167.4
O13–H13B···O10^{i}	0.87	1.99	2.847(2)	169.0
O11–H11A.···O10	0.87	1.88	2.736(2)	167.4
O11–H11B···O7^{ii}	0.87	2.03	2.888(2)	167.1

Symmetry transformations used to generate equivalent atoms:
i) –x,y–1/2,–z (ii) –x+1,y–1/2,–z+1/2

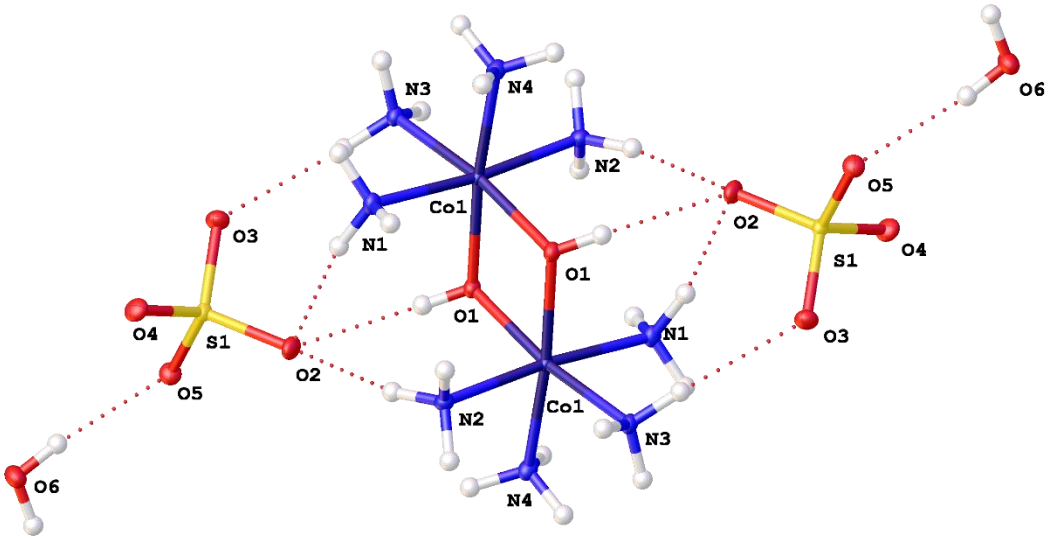

Figure 3-3: Molecular structure of $[(Co(NH_3)_4)_2(\mu\text{-}OH)_2](SO_4)_2{\cdot}2H_2O$ found amongst Werner's complex solid precipitant.

bond angles and lengths summarised in Table 3-3, but it can be seen from the parameters that the two Co(III) complexes are charge balanced by a single sulphate. However, the molecular arrangement distorts the two complexes differently.

With the carbonate ligand now in a bidentate coordination, the Co–O bond lengths have now significantly shortened (by ~0.020 Å), with an average of 1.912(2) Å versus the Co–N average of 1.9578(3) Å (Co2 is the example). This creates a "flattening" of the octahedral on one of the edges about the Co nucleus. There is also a significant strain on the carbonate group, where the O–C–O angle was ~120° for the pentammine it is now ~110°. The sulphate structure is comparable to that reported before by Macikenas *et al.*[98], however, proton positions and a hydrogen bonding scheme were not included.

Differences in the CO_3 groups for the two sulphate complexes (bond lengths ranging from 1.236(2) to 1.318(2) Å and 1.228(2) to 1.324(2) Å) may give rise to inequivalence in the Co environments. This is very similar to what is seen in the reported structure of $[Co(NH_3)_4CO_3](NO_3){\cdot}0.5H_2O$ where the complexes and anions form layers with a small amount of crystallographic H_2O bonding with the NO_3.[99]

The carbonatotetrammine complex has been shown to be versatile, forming with a variety of counter ions. The structure of $[Co(NH_3)_4CO_3]Br$ has been reported multiple times, the study by Barclay and Hoskins being the most accurate.[100,101] Without crystallographic water, it is structurally different to other carbonatotetrammine complexes and occupies the Pcmn space group. The two ammine ligands *trans* to one another H-bond either to the Br counter ion or to two of the carbonates O. Without water in the hydrogen bonding network the Co–N bond lengths have much more variation ranging from 1.93 to 2.03 Å, the longest being a *cis* ammine group (defined as planar to the oxygen coordinated ligands).[101] The greater distortion of the octahedron may have a significant effect on the NMR parameters.

As shown in section 3.2.1 $[Co(NH_3)_4CO_3](SO_4)_{0.5}\cdot 1.5H_2O$ was converted to Werner's complex $[Co((\mu\text{-}OH)_2Co(NH_3)_4)_3](SO_4)_3\cdot 9H_2O$, however, an intermediate was found whilst attempting to collect a suitable crystal. The structure of this intermediate, $[(Co(NH_3)_4)_2(\mu\text{-}OH)_2](SO_4)_2\cdot 2H_2O$, is shown in Figure 3-3. To the best

Table 3-5: Selected bond lengths and angles for $[(Co(NH_3)_4)_2(\mu\text{-}OH)_2](SO_4)_2\cdot 2H_2O$ Figure 3-3 the protons were described such N–H was 0.89 Å with an H–N–H angle of 109.5 ° respectively.

Bond lengths (Å)		Bond lengths (Å)	
Co1–Co1[*1]	2.9205(11)	Co1–N4	1.964(3)
Co1–O1	1.923(3)	S1–O2	1.485(3)
Co1–O1[1]	1.922(3)	S1–O3	1.475(3)
Co1–N1	1.954(4)	S1–O4	1.478(3)
Co1–N2	1.962(4)	S1–O5	1.473(3)
Co1–N3	1.962(3)	-	-
Bond Angles (°)		Bond Angles (°)	
O1–Co1–Co1[1]	40.55(9)	N1–Co1–N4	86.50(15)
O1[1]–Co1–Co1[1]	40.57(9)	N2–Co1–Co1[1]	92.20(11)
O1[1]–Co1–O1	81.13(13)	N2–Co1–N4	90.08(15)
O1[1]–Co1–N1	90.10(14)	N3–Co1–Co1[1]	132.16(11)
O1–Co1–N1	94.90(14)	N3–Co1–N2	88.94(15)
O1–Co1–N2	89.01(14)	N3–Co1–N4	95.19(15)
O1[1]–Co1–N2	94.33(14)	N4–Co1–Co1[1]	132.61(11)
O1[1]–Co1–N3	172.04(14)	Co1[1]–O1–Co1	98.87(13)
O1–Co1–N3	91.69(14)	O3–S1–O2	109.40(18)
O1[1]–Co1–N4	92.06(14)	O3–S1–O4	110.24(18)
O1–Co1–N4	173.04(14)	O4–S1–O2	109.18(18)
N1–Co1–Co1[1]	93.29(11)	O5–S1–O2	108.87(18)
N1–Co1–N2	174.50(15)	O5–S1–O3	110.32(18)
N1–Co1–N3	87.08(15)	O5–S1–O4	108.80(18)

[*]Internuclear distance, not a bond;[1]1-x, 1-y, 1-z

Table 3-6: Hydrogen bonding scheme for $[(Co(NH_3)_4)_2(\mu\text{-}OH)_2](SO_4)_2\cdot 2H_2O$.

D–H···*A*	*d*(*D*–H) (Å)	*d*(H···*A*) (Å)	*d*(*D*···*A*) (Å)	∠(*DHA*) (°)
O1–H1···O2	0.77(6)	2.09(7)	2.839(4)	164(6)
N1–H1C···O5[1]	0.89	1.98	2.854(5)	167.5
O6–H6A···O5	0.79(7)	2.01	2.746(5)	173(6)
O6–H6B···O2[2]	0.81(7)	1.96(7)	2.784(5)	174(6)

Symmetry transformations used to generate equivalent atoms:
[1] 1+x,+y,+z [2] -x,-y,1-z

of the authors knowledge, there are no comparable structures reported in the literature. This would be understandable considering that the formation of Werner's complex occurs at ambient pressure and temperature, indicating "significant" reactivity. However, dimeric bromide and iodide structures with three hydroxyl bridges have been reported by Andersen in 1967.[102] The study showed the two octahedra about the

Co centres shared a similar face. Interestingly the Co–N (1.92 to 2.18 Å) and Co–O (1.90 to 1.98 Å) these bond distances have significantly larger extremes than anything seen in the data collected here.

With the Co octahedra sharing a vertex rather than a face a much higher point symmetry appears to exist. The structure was generated such the two Co are equivalent. The three longer Co–N bonds can be seen ~1.963 Å plus a short one at 1.954(4) Å. The Co–O lengths though are shorter at 1.922(2) Å causing a flattening of the octahedra similar to that discussed previously for the carbonato-tetramminecobalt complex. However, compared to the triple OH bridge found in literature, these bond lengths vary much less and sit roughly in the middle of the ranges of what was previously reported.[102]

A detailed hydrogen bonding scheme can be seen in Table 3-6 where it was found ammine and hydroxyl ligands bond to the anion the distances of which are very short. The hydrogen bonding network is stereotypical of these types of octahedral complexes.[103]

Table 3-7:Selected bond lengths and distances for $[Co((\mu\text{-}OH)_2Co(NH_3)_4)_3](SO_4)_3 \cdot 9H_2O$, Werner's complex shown in Figure 3-4.

Bond lengths (Å)		Bond lengths (Å)			
Co1–Co2*	2.8678(11)	Co2–Co1^2	2.8678(11)	-	-
Co1–O1	1.930(6)	Co2–O1^2	1.920(6)	-	-
Co1–O2	1.902(6)	Co2–O1	1.920(6)	-	-
Co1–N1	1.969(8)	Co2–O1^1	1.920(6)	-	-
Co1–N2	1.965(8)	Co2–O2^2	1.900(6)	-	-
Co1–N3	1.941(8)	Co2–O2	1.900(6)	-	-
Co1–N4	1.944(8)	Co2–O2^1	1.900(6)	-	-
Bond Angles (°)		Bond Angles (°)		Bond Angles (°)	
O1–Co1–Co2	41.72(17)	N4–Co1–N2	93.6(3)	O2^2–Co2–Co1^2	41.05(18)
O1–Co1–N1	91.2(3)	Co1–Co2–Co1^1	119.987(2)	O2^2–Co2–Co1	91.94(18)
O1–Co1–N2	85.6(3)	Co1^1–Co2–Co1^2	119.987(2)	O2–Co2–Co1^1	91.94(18)
O1–Co1–N3	94.8(3)	Co1–Co2–Co1^2	119.987(2)	O2^1–Co2–Co1	134.57(19)
O1–Co1–N4	174.1(3)	O1^1–Co2–Co1^1	41.98(17)	O2–Co2–Co1	41.05(18)
O2–Co1–Co2	41.00(18)	O1^1–Co2–Co1^2	135.99(18)	O2^1–Co2–O1^1	83.0(2)
O2–Co1–O1	82.7(2)	O1^2–Co2–Co1	135.99(18)	O2^1–Co2–O1^2	89.4(2)
O2–Co1–N1	86.5(3)	O1^2–Co2–Co1^2	41.98(17)	O2^2–Co2–O1^1	175.6(2)
O2–Co1–N2	92.5(3)	O1–Co2–Co1^2	92.43(18)	O2–Co2–O1	83.0(2)
O2–Co1–N3	177.2(3)	O1^2–Co2–Co1^1	92.43(17)	O2^1–Co2–O1	175.6(2)
O2–Co1–N4	91.4(3)	O1^1–Co2–Co1	92.43(17)	O2–Co2–O1^1	89.4(2)
N1–Co1–Co2	88.5(2)	O1–Co2–Co1^1	135.99(18)	O2^2–Co2–O1^2	83.0(2)
N2–Co1–Co2	88.7(2)	O1–Co2–Co1	41.99(17)	O2^2–Co2–O1	89.4(2)
N2–Co1–N1	176.8(3)	O1^1–Co2–O1^2	94.1(2)	O2–Co2–O1^2	175.6(2)
N3–Co1–Co2	136.5(3)	O1^1–Co2–O1	94.1(2)	O2–Co2–O2^2	93.6(3)
N3–Co1–N1	92.3(3)	O1–Co2–O1^2	94.1(2)	O2^2–Co2–O2^1	93.6(3)
N3–Co1–N2	88.5(3)	O2^2–Co2–Co1^1	134.56(19)	O2–Co2–O2^1	93.6(3)
N3–Co1–N4	91.0(3)	O2–Co2–Co1^2	134.57(19)	Co2–O1–Co1	96.3(3)
N4–Co1–Co2	132.4(2)	O2^1–Co2–Co1^2	91.94(18)	Co2–O2–Co1	97.9(3)
N4–Co1–N1	89.5(3)	O2^1–Co2–Co1^1	41.05(18)	-	-

*Internuclear distance, not a bond; ^{1}1-y,1+x-y,+z; ^{2}+y-x,1-x,+z

It was not possible to acquire a full structural description of the unit cell for Werner's complex. However, the core complex was obtained and is illustrated in Figure 3-4, the associated bond lengths and angles for the ligands can be seen in Table 3-7. There are 9 crystallographic H_2O molecules in the unit cell coupled with what appeared to be several disordered SO_4 counter ions.[43] It was this disorder which limited the analysis to the main complex. The central cobalt fully oxygen coordinated core sits in a highly symmetric environment but the Co–O bond lengths do differ, being either 1.900(6) Å or 1.920(6) Å. The two different bond lengths are arranged such that all

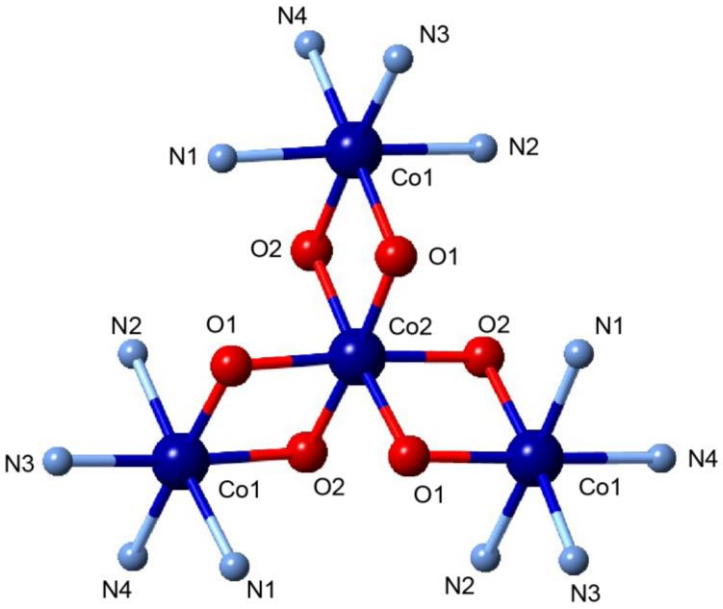

Figure 3-4: Partial structure of Werner's complex, $[Co((\mu\text{-}OH)_2Co(NH_3)_4)_3](SO_4)_3 \cdot 9H_2O$, used to illustrate the configuration of the main complex, disordered sulphate anions hindered the refinement.

those bonds of 1.900(6) Å are *cis* to one another, similarly for those of 1.920(6) Å. This creates an octahedra which has high symmetry but would appear with four of the faces compressed. The OH bridges of Werner's complex are of similar lengths to those seen in the dimeric complex in Figure 3-3. This distortion is different to what has been reported before for nitrate versions reported by Bernal *et al.*[103]

These previously reported structures are for $[Co((\mu\text{-}OH)_2Co(NH_3)_4)_3](NO_3)_5(OH) \cdot 4H_2O$ and $[Co((\mu\text{-}OH)_2Co(NH_3)_4)_3](NO_3)_6 \cdot 2H_2O$.[103] When the hydroxyl anion is no longer present, the central Co nucleus has only two long Co–O bonds of ~1.920(3) Å rather than the three that occur with the sulphate as reported here. A further perturbation of the main complex can be seen in $[Co((\mu\text{-}OH)_2Co(NH_3)_4)_3](NO_3)_6 \cdot 2H_2O$ where only one of the Co–O bonds is ~1.920(3) Å. The varying bond lengths of the central oxygen coordinated cobalt give a clear insight into the far-reaching effects of the second order coordination sphere. The three tetrammine units about the central oxygen coordinated core demonstrate equivalence in terms of ligand

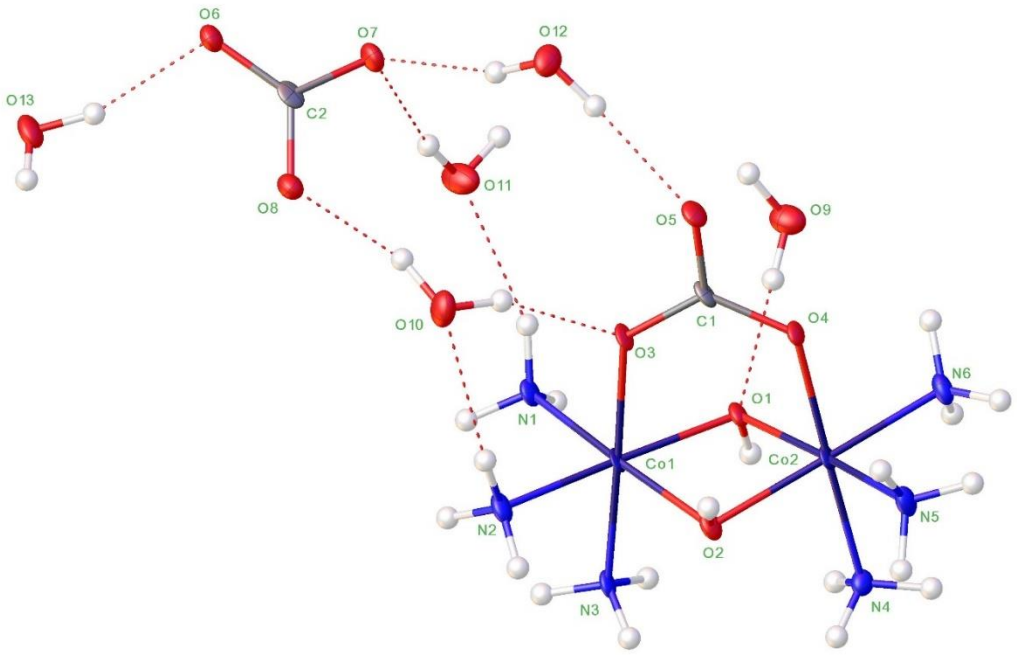

Figure 3-5: Molecular structure of $[(Co(NH_3)_3)_2(\mu\text{-}OH)_2(\mu\text{-}CO_3)](CO_3)\cdot 5H_2O$. Atomic displacement ellipsoids represent 50% probability.

distances. The four ammine ligands sit either 1.944(8) Å, when they are *cis* to all others or 1.965(8) Å, when one sits in a *trans* position.[103]

The final complex to be studied was extracted from the industrial HDC catalyst preparation after oxidation of the solution derived from Co metal via air. The crystals obtained from this method were significantly larger than those from the $CoCO_3$ method. A dimeric triammine complex, $[(Co(NH_3)_3)_2(\mu\text{-}OH)_2(\mu\text{-}CO_3)](CO_3)\cdot 5H_2O$, which has a triple bridge structure via two hydroxyls and a carbonate group, as shown in Figure 3-5, was isolated. The material was pure, verified by the NMR (see Section 3.3.2).

From literature a similar complex has been reported by Churchill *et al.*[104] with a sulphate counter ion which would readily decompose in aqueous solution liberating CO_3 and substituting in two water ligands. The decomposition process is reversible in the presence of sodium bicarbonate.[104] Comparing the immediate coordination of the both Co positions reveals a strikingly similar geometry between $[(Co(NH_3)_3)_2(\mu\text{-}OH)_2(\mu\text{-}CO_3)](CO_3)\cdot 5H_2O$ and $[(Co(NH_3)_3)_2(\mu\text{-}OH)_2(\mu\text{-}CO_3)](SO_4)\cdot 5H_2O$ even with the slightly smaller carbonate anion. The similarities in Co–N bond lengths and

asymmetries of the hydroxyl bridges for these systems can be seen in the work by Churchill *et al.* which contains a more complete structure analysis.[104]

The proposed H-bonding scheme for $[(Co(NH_3)_3)_2(\mu\text{-}OH)_2(\mu\text{-}CO_3)](CO_3)\cdot 5H_2O$ can be seen in Table 3-8. It can be seen all the waters of crystallisation participate in bonding the anion to the main complex. The longest H-bond is from the unbound oxygen of the bridging carbonate at 2.03 Å. The carbonate bridge shares similarities to both the pentammine and tetrammine complexes (which had bidentate carbonate

Table 3-8: Selected bond lengths and angles for $[(Co(NH_3)_3)_2(\mu\text{-}OH)_2(\mu\text{-}CO_3)](CO_3)\cdot 5H_2O$ shown in Figure 3-5.

Bond lengths (Å)		Bond lengths (Å)		Bond lengths (Å)	
Co1–Co2*	2.7914(9)	Co2–O1	1.898(4)	O2–H2	0.87(7)
Co1–O1	1.910(4)	Co2–O2	1.895(4)	O3–C1	1.303(6)
Co1–O2	1.893(4)	Co2–O4	1.915(4)	O4–C1	1.299(7)
Co1–O3	1.918(14)	Co2–N4	1.931(5)	O5–C1	1.250(7)
Co1–N1	1.936(4)	Co2–N5	1.949(5)	O6–C2	1.275(7)
Co1–N2	1.940(5)	Co2–N6	1.941(5)	O7–C2	1.300(7)
Co1–N3	1.939(5)	O1–H1	0.86(8)	O8–C2	1.268(7)
Bond Angles (°)		Bond Angles (°)		Bond Angles (°)	
O1–Co1–Co2	42.70(12)	N3–Co1–Co2	99.93(13)	N4–Co2–N6	90.42(19)
O1–Co1–O3	87.37(16)	N3–Co1–N2	87.93(19)	N5–Co2–Co1	130.91(14)
O1–Co1–N1	92.08(18)	O1–Co2–Co1	43.04(12)	N6–Co2–Co1	134.24(15)
O1–Co1–N2	175.71(18)	O1–Co2–O4	88.04(16)	N6–Co2–N5	93.7(2)
O1–Co1–N3	93.67(17)	O1–Co2–N4	92.88(18)	Co1–O1–H1	110(5)
O2–Co1–Co2	42.57(12)	O1–Co2–N5	173.58(19)	Co2–O1–Co1	94.27(18)
O2–Co1–O1	84.17(17)	O1–Co2–N6	91.89(18)	Co2–O1–H1	106(5)
O2–Co1–O3	91.19(16)	O2–Co2–Co1	42.49(12)	Co1–O2–Co2	94.94(18)
O2–Co1–N1	175.99(19)	O2–Co2–O1	84.42(17)	Co1–O2–H2	117(4)
O2–Co1–N2	91.86(18)	O2–Co2–O4	93.01(16)	Co2–O2–H2	104(4)
O2–Co1–N3	89.87(17)	O2–Co2–N4	87.67(18)	C1–O3–Co1	127.4(4)
O3–Co1–Co2	81.48(11)	O2–Co2–N5	90.11(18)	C1–O4–Co2	125.7(3)
O3–Co1–N1	90.05(17)	O2–Co2–N6	175.76(19)	O4–C1–O3	122.2(5)
O3–Co1–N2	91.10(17)	O4–Co2–Co1	83.15(11)	O5–C1–O3	118.4(5)
O3–Co1–N3	178.59(17)	O4–Co2–N4	178.90(18)	O5–C1–O4	119.3(5)
N1–Co1–Co2	133.99(14)	O4–Co2–N5	88.87(18)	O6–C2–O7	119.2(5)
N1–Co1–N2	91.9(2)	O4–Co2–N6	88.96(18)	O8–C2–O6	121.5(5)
N1–Co1–N3	88.96(19)	N4–Co2–Co1	97.94(14)	O8–C2–O7	119.3(5)
N2–Co1–Co2	133.09(14)	N4–Co2–N5	90.3(2)	-	-

*Internuclear distance, not a bond.

ligands). Firstly, the Co1–O3 and Co2–O4 distances of $[(Co(NH_3)_3)_2(\mu\text{-}OH)_2(\mu\text{-}CO_3)](CO_3)\cdot 5H_2O$ can be seen in Table 3-7 to be 1.918(14) Å and 1.915(4) Å, respectively. These are short compared to the bidentate ligands in the tetrammine complexes. However, by bridging between the two cobalt nuclei the carbonate adopts a more relaxed configuration as seen by the O–C–O angles (close to 120˚) in Table 3-8Table 3-8. The unbound oxygen (O5) is a distance between what was seen in the tetrammine and pentaamine complexes. Thus, it is unclear whether these three carbonate configurations are unique from an NMR perspective, or if there is equivalence.

A summary of bond lengths and internuclear distances between Co (where appropriate) are summarised in Table 3-10. Thus, to reiterate, the Co–O bond lengths are typically shorter than the Co–N except for the pentammine complex, $[Co(NH_3)_5CO_3]NO_3\cdot H_2O$. This complex at inspection demonstrates the highest symmetry in terms of bond lengths. Through the series, Co–O bonds to hydroxyl bridges are generally shorter than those to carbonates. Furthermore, an inspection of

Table 3-9: Hydrogen bonding scheme for $[(Co(NH_3)_3)_2(\mu\text{-}OH)_2(\mu\text{-}CO_3)](CO_3)\cdot 5H_2O$ shown in Figure 3-5.

D–H···*A*	*d*(*D*–H) (Å)	*d*(H···*A*) (Å)	*d*(*D*···*A*) (Å)	∠(*D*H*A*) (°)
N1–H1C···O6^{i}	0.91	1.98	2.868(6)	165.2
N3–H3C···O5^{ii}	0.91	1.99	2.893(5)	174.5
O9–H9A···O1	0.87	1.90	2.766(6)	173.5
O9–H9B···O13^{iii}	0.87	2.06	2.852(6)	151.8
O10–H10A···O8	0.87	1.80	2.641(6)	163.3
O10–H10B···O3	0.87	1.87	2.694(5)	158.4
O11–H11A···O10^{iv}	0.87	2.00	2.786(7)	149.9
O11–H11B···O7	0.87	1.97	2.834(6)	171.9
O12–H12A···O7	0.87	1.89	2.730(6)	162.4
O12–H12B···O5	0.87	1.94	2.781(6)	163.7
O13–H13A···O5^{v}	0.87	2.07	2.793(6)	140.4
O13–H13B···O6	0.87	1.88	2.689(6)	152.9
O2–H2···O9^{vi}	0.87(7)	1.93(7)	2.800(6)	173(6)
O1–H1···O7^{i}	0.86(8)	1.86(8)	2.719(5)	175(8)

Symmetry transformations used to generate equivalent atoms:
^{i}x–1/2,–y+1,z; ^{ii}–x+1/2,y,z+1/2; ^{iii}–x+1,–y+1,z–1/2; ^{iv}x,y+1,z; ^{v}–x+1,–y,z+1/2; ^{vi}x,y–1,z

Table 3-10: Summary of internuclear distances and bond lengths for the Co(III) ammine complexes which were measured using single crystal X-ray diffraction.

Sample	Co–Co (Å)	Co–N (Å)	Co–O (Å)	∠(OCoO) (°)
$[Co(NH_3)_5CO_3]NO_3{\cdot}H_2O$	-	1.942(10) -1.979(9)	1.939(7)	-
$[Co(NH_3)_4CO_3](SO_4)_{1.5}{\cdot}1.5H_2O$	-	1.9441(16) -1.9655(18)	1.9029(13) -1.9199(14)	69.03(6) -69.21(6)
$[(Co(NH_3)_4)_2(\mu\text{-}OH)_2](SO_4)_2{\cdot}H_2O$	2.9205(11)	1.954(4) -1.964(3)	1.923(3)	81.13(13)
$[Co((\mu\text{-}OH)_2Co(NH_3)_4)_3](SO_4)_3{\cdot}9H_2O$	2.8678(11)	1.941(8) -1.969(8)	1.900(6) -1.930(6)	82.7(2)[a]/83.0(2) [b] -93.6(3)[b]
$[(Co(NH_3)_3)_2(\mu\text{-}OH)_2(\mu\text{-}CO_3)](CO_3){\cdot}5H_2O$	2.7914(9)	1.931(5) -1.949(5)	1.893(4) -1.918(14)	84.30(24)[c]

[a]∠(OCoO) for outer ammine coordinated unit; [b]Central oxo coordinated site; [c]Average angle between OH bridges.

the different O–Co–O angles shows the six ligands about the Co cannot all be orthogonal to oneanother. Thus a distortion of the octahedra is immediately apparent for all the complexes reported. The most acute angle between O ligands was seen in $[Co(NH_3)_4CO_3](SO_4)_{1.5}{\cdot}1.5H_2O$ complex, where the bidentate ligand forces the oxygen together shown by the ~69˚ O–Co–O angle.

Finally, of the dimeric materials and Werner's complex seperation of the Co centers can be seen to vary. As a dimer $[(Co(NH_3)_4)_2(\mu\text{-}OH)_2](SO_4)_2{\cdot}H_2O$ has the largest separation at 2.9205(11) Å. With the increased size of the complex more restraint on the structure could explain the reduction of the Co–Co distance within Werner's complex. However, the HDC material $[(Co(NH_3)_3)_2(\mu\text{-}OH)_2(\mu\text{-}CO_3)](CO_3){\cdot}5H_2O$ was observed to have the smallest separation of Co centres due to the presence of the third bridging ligand.

3.3.2 Static ^{59}Co Solid State NMR

The measurement of the central ½ to –½ transition the nine model Co(III) complexes has been undertaken at a range of magnetic fields from 4.7 T to 20 T. Figure 3-6(a) shows the central transition of $[Co(NH_3)_5CO_3]NO_3{\cdot}H_2O$, the multiple field analysis constrains the NMR parameters yielding an δ_{iso} of 8992 ppm. Of particular note is

the changing dominance of the quadrupole and CSA interactions that can be observed as the external field is varied from 4.7 T to 20.0 T. This phenomenon is a characteristic of ^{59}Co studies.

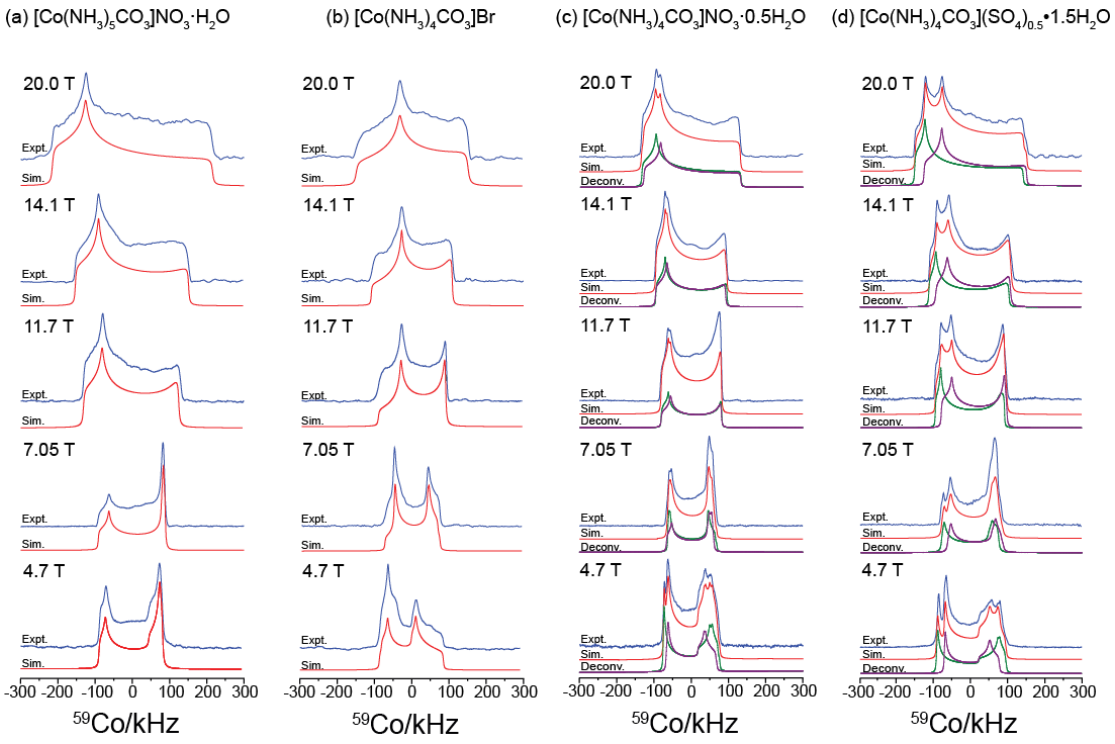

Figure 3-6: Solid state ^{59}Co NMR spectra measured at 4.7, 7.05, 11.7 and 20 T: (a) $[Co(NH_3)_5CO_3]NO_3{\cdot}H_2O$, (b) $[Co(NH_3)_4CO_3]Br$, (c) $[Co(NH_3)_4CO_3]NO_3{\cdot}0.5H_2O$ and (d) $[Co(NH_3)_4CO_3](SO_4)_{0.5}{\cdot}1.5H_2O$.

The NMR parameters for the ^{59}Co measurements are summarised in Table 3-11. The first sample analysed was $[Co(NH_3)_5CO_3]NO_3{\cdot}H_2O$ (pentammine) which had a single O coordinated ligand yielding a δ_{iso} of 8992 ppm. The magnitude of the quadrupolar interaction, related to the C_Q, was 19.3 MHz, comparable to the carbonatotetrammine series shown in Figure 3-6(b-d). Qualitatively this can be seen from the similar line widths at 4.7 T. Furthermore, the interaction is close to axial symmetry, η_Q was measured to be 0.35. Measurements taken at 20.0 T show the CSA of the pentammine sample are different to the carbonatotetrammine series despite having a similar skew (κ) of ~0.5. The difference arises in the span (Ω) which was found to be ~500 ppm larger for the pentammine sample compared to the carbonatotetrammine series. The CSA is known to be sensitive to the chemical bonding, thus this indicates a difference

between the bonding of monodentate carbonate and bidentate carbonate of the other complexes (see section 3.3.3).[66]

A large change in Ω was also seen in pentammine complexes studied by Ooms *et al*.[80] Rather than a carbonate ligand these had a NO_2 group which bonded either via the O (nitrito) or the N (nitro). The two isomers demonstrated either prevalent ionic or covalent bonding, seen by the presence of J-coupling in the ^{15}N measurements.[80] Thus, it is proposed the monodentate and bidentate carbonate ligands of the complexes in Figure 3-6 bond differently too, either ionically or covalently.

Higher oxo coordination has been first been shown by the bidentate carbonate ligand, for $[Co(NH_3)_4CO_3]Br$, Figure 3-6(b) this yielded a δ_{iso} of 9773 ppm. Lacking crystallographic water and the presence of a counter ion without O make this complex unique within the suite of samples. Thus, causing significant differences when compared to the nitrate and sulphate complexes in Figure 3-6(c) and (d). Although, the C_Q was found to be 18.5 MHz and the Ω was 1510 ppm which are similar to the nitrate and sulphate samples. The η_Q was found to be 0.71 showing disparity between the x and y components of the EFG not observed in any other complex. These changes in the components are probably due to perturbations caused by the bromide counter ion. Furthermore, the lack of a large H-bonding scheme (compared to when crystallographic water is present) should be seen in the NMR of the ligands.

A direct comparison of $[Co(NH_3)_5CO_3]NO_3{\cdot}H_2O$ (pentammine) to $[Co(NH_3)_4CO_3]NO_3{\cdot}0.5H_2O$ (tetrammine, Figure 3-6(c)) allows for a more precise description of increasing oxo coordination. With the additional oxygen ligand, the δ_{iso} of the tetrammine was ~9665 ppm equating to an increase of ~670 ppm from the pentammine. Furthermore, with the change of conformation the C_Q and Ω have decreased (Table 3-11) indicating the point symmetry about the cobalt nucleus has increased. A significant change was seen in the quadrupolar asymmetry parameter (η_Q) which differs between the samples by more than 0.3, indicating a change in the EFG about the nucleus. This change would be expected with the reorientation of the charge balancing carbonate ligand. The parameters for these complexes are in good

agreement with those reported before by Kirby *et al*.[89] Due to the greater span in magnetic fields and better sample quality here the parameters have been refined including the Euler angles. Furthermore, two inequivalent sites are resolved for $[Co(NH_3)_4CO_3]NO_3 \cdot 0.5H_2O$.[89]

Comparing the systems shown in Figure 3-6 (c) and (d) demonstrates the effects of the NO_3 and SO_4 anions. This data shows marked similarity in terms of NMR lineshapes with both having two crystallographic inequivalent Co environments in the unit cell. The larger SO_4 anion is associated with more crystallographic water which is thought to be the cause of the greater separation of the two environments in terms of the isotropic chemical shift, δ_{iso}. This is observable as a clear splitting feature on the high frequency side of the spectra. Across the carbonatotetrammine complex series shown in Figure 3-6(b-d) the δ_{iso} only varies by ~100 ppm which is only marginally outside the confidence limit of the measurements. It is the CSA and quadrupole interactions which show significant variation. These parameters are clearly sensitive to the environment beyond the first coordination sphere.

The complex of $[Co(NH_3)_4(H_2O)_2](SO_4)_{1.5} \cdot 1.5H_2O$, shown in Figure 3-7(a), can readily associate into dimeric and Werner's type complexes, as seen in section 3.2.1. The replacement of the bidentate carbonate ligand with the two water ligands yielded a δ_{iso} increase (9826 ppm). The increase of ~300 ppm demonstrates changes in chemical shift is also sensitive to type of oxo coordination. However, this change was not immediately apparent due to the significant Ω of 3042 ppm and C_Q of 43.4 MHz. The large CSA and quadrupole interactions yielded very broad ^{59}Co central transitions. The measurement at 20.0 T lacks a pure CSA lineshape indicating an influence from the quadrupolar interaction was still present even at this very high magnetic field. The η_Q measured was small, indicating a cylindrically symmetric quadrupole interaction, reflective of the charge balancing occurring beyond the immediate coordination sphere. Finally, it has also been observed that the κ altered sign with the changed type of oxo coordination. It is unclear whether the change in sign is due to the removal of CO_3 or the presence of the H_2O ligands.

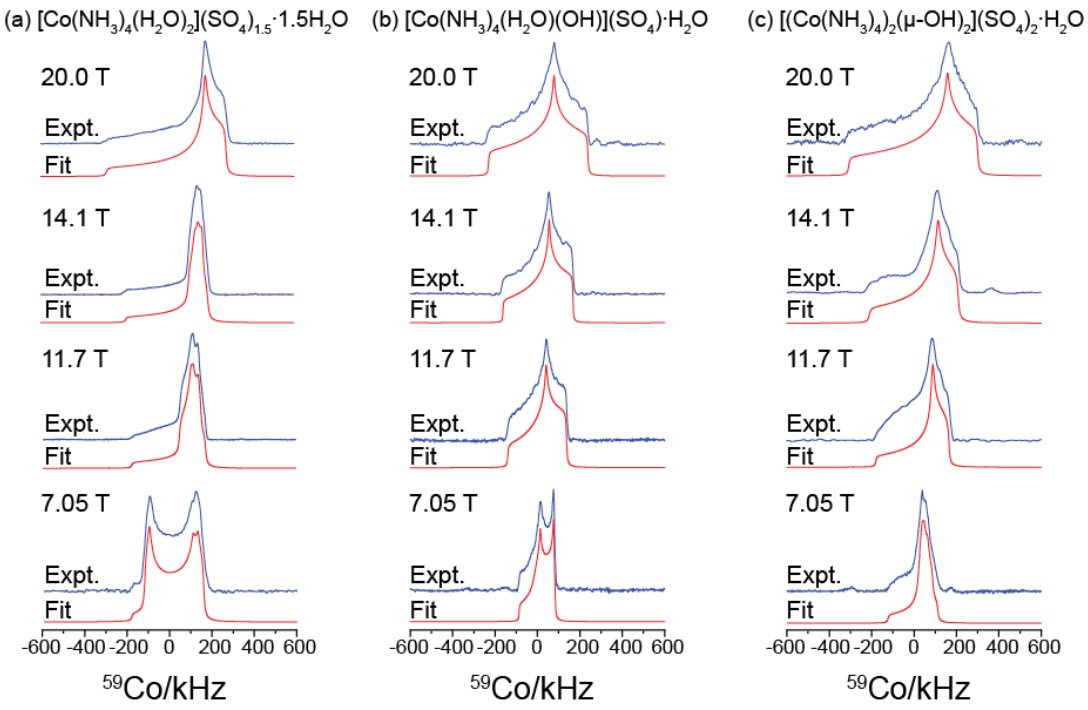

Figure 3-7: ^{59}Co static solid state measurements at 7.05 T, 11.7 T, 14.1 T and 20 T of the Co(III) complexes shown where (a) $[Co(NH_3)_4(H_2O)_2](SO_4)_{0.5}\cdot 1.5H_2O$, (b) $[Co(NH_3)_4(H_2O)(OH)](SO_4)\cdot H_2O$ and (c) $[Co(NH_3)_4(\mu\text{-}OH)_2](SO_4)_2\cdot H_2O$.

Upon deprotonation of one of the water ligand in $[Co(NH_3)_4(H_2O)_2](SO_4)_{1.5}\cdot 1.5H_2O$ to form $[Co(NH_3)_4(H_2O)(OH)](SO_4)\cdot H_2O$ (Figure 3-7(b)) causes a significant downfield shift to a δ_{iso} of 10098 ppm. This observation indicates significantly higher electronegativity influencing the composition. The sample also produced the largest η_Q, 0.81, this may be due to the concentration of charge on the hydroxyl ligand. Although both complexes have oxo ligands which can coordinate separately, the lineshapes fitted were obtained using only a single ^{59}Co environment in both cases. Thus, a single ligand arrangement exists where the oxygen donors are either *cis* or *trans* to one another.

Upon drying the $[Co(NH_3)_4(H_2O)(OH)](SO_4)\cdot H_2O$ complex converted to the dimeric structure of $[Co(NH_3)_4(\mu\text{-}OH)_2](SO_4)_2\cdot H_2O$. Although still hydrated the ratio of Co: H_2O has changes from 1:1 to 2:1, indicating a loss of water. The NMR measurements obtained are comparable to the other tetrammine complexes reported here. The V_{ZZ}

component of the EFG would likely lie close to the internuclear vector between the cobalt since the charged hydroxyl bridges lay wither side of this.

From the synthesis method referred to in Section 3.2.1 it has been shown $[Co(NH_3)_4(H_2O)_2](SO_4)_{1.5}\cdot 1.5H_2O$ can have the carbonate bidentate ligand removed and replaced with two water molecules forming $[Co(NH_3)_4(H_2O)(OH)](SO_4)\cdot H_2O$ which in turn associate into a dimeric structure $[Co(NH_3)_4(\mu\text{-}OH)_2](SO_4)_2\cdot H_2O$ from

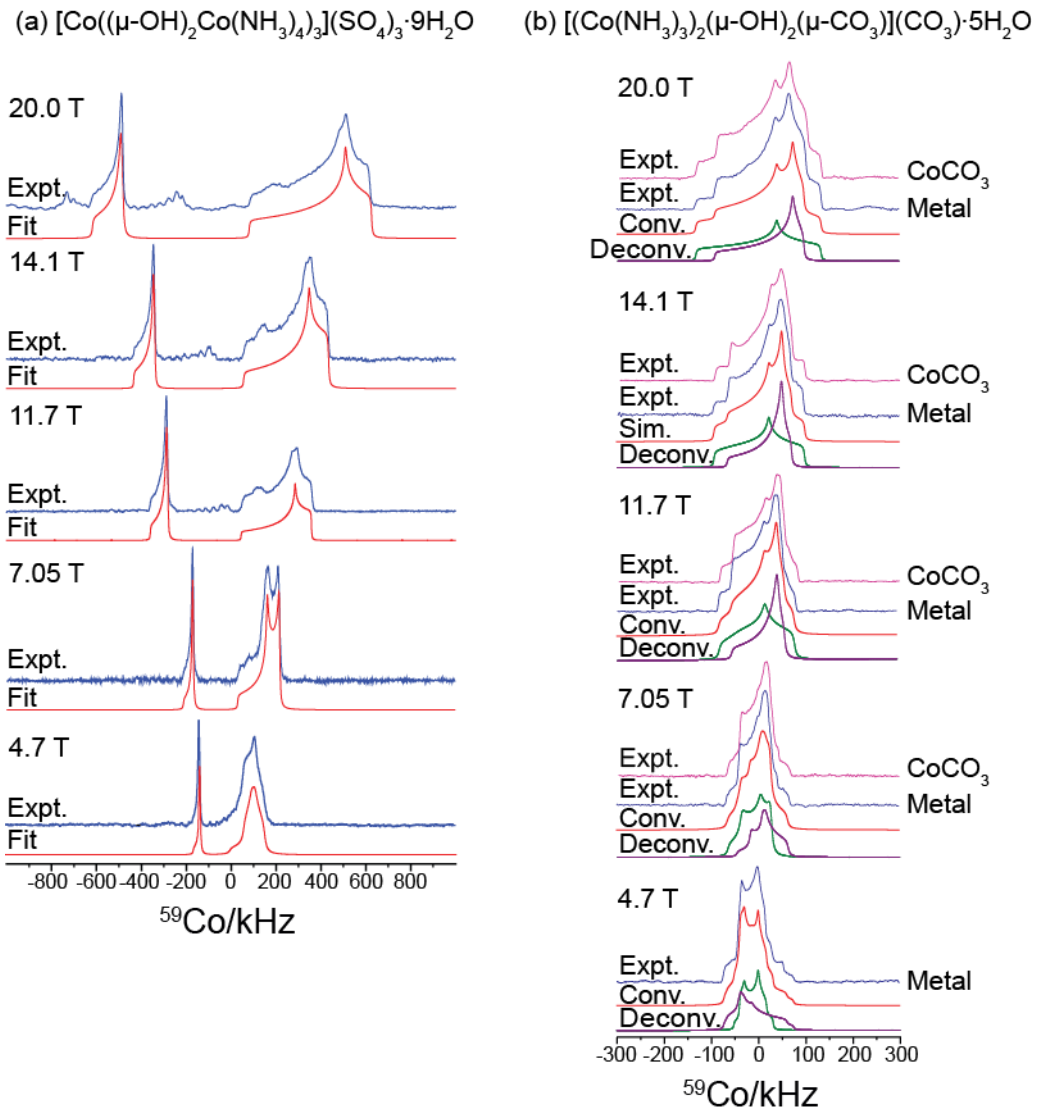

Figure 3-8: ^{59}Co static solids state measurements of the central transition of (a) $[Co((\mu\text{-}OH)_2Co(NH_3)_4)_3](SO_4)_3\cdot 9H_2O$ with a full oxo-coordinated cobalt at the centre of the complex and (b) $[(Co(NH_3)_3)_2(\mu\text{-}OH)_2(\mu\text{-}CO_3)](CO_3)\cdot 5H_2O$.

single crystal observations of $[Co(NH_3)_4(\mu\text{-}OH)_2](SO_4)_2{\cdot}2H_2O$ as determined by the single crystal study, before forming Werner's complex. Disorder in the sulphate anion position makes it difficult to fully analyse Werner's complex structure. The NMR measurements demonstrate a clear separation of the two ^{59}Co environments, presented in Figure 3-8(a), and the parameters for both environments are summarised in Table 3-11.

The three tetrammine units of Werner's complex are of an equivalence, requiring only one ^{59}Co environment to fit the experimental data. The δ_{iso} of 9895 ppm was larger than all the carbonatotetrammine complexes measured but was within the range of those coordinated to water and hydroxyls as shown in Figure 3-7. This is also reflected within the CSA and quadrupole parameters where the larger structure constrains the Ω to 2715 ppm and C_Q to 16.3 MHz. The only significant difference to the dimeric tetrammine $[Co(NH_3)_4(\mu\text{-}OH)_2](SO_4)_2{\cdot}H_2O$ can be seen in the C_Q this could be attributed to the difference in oxo coordination of the neighbouring cobalt nuclei coupled with distances from the anions and other cobalt nuclei which could contribute to the EFG.

The fully oxo coordinated core of Werner's complex was significantly shifted to higher frequencies and was observed at 14518 ppm. The core was clearly separated from the tetrammine resonance. The high point symmetry of this Co position and the associated reduced linewidth at each field make it possible to observe the ±1/2 - ±3/2 satellite transition. Clearest evidence for this can be observed in the data acquired at 20.0 T. The associated NMR parameters are presented in Table 3-11. Without the observation of satellite transition an accurate simulation of the NMR resonance would not be possible due to the small C_Q of 3.5 MHz which is constantly dwarfed by the CSA interaction across all fields. This would be due to the asymmetry of the Co–O bond distances and angles seen in section 3.3.1. Never the less, the CSA is significantly smaller than previously measured with a Ω of 690 ppm reflecting the high symmetry of the all oxo coordination about the Co position.

The final Co(III) complex isolated was the $[(Co(NH_3)_3)_2(\mu\text{-}OH)_2(\mu\text{-}CO_3)](CO_3)\cdot 5H_2O$ which was obtained from the industrial synthesis using cobalt metal and analysed by single crystal XRD in section 3.3.1. No crystals large enough for a similar analysis were obtained from the $CoCO_3$ method. However, the NMR measurements of the solid materials obtained from both synthesis routes shown in Figure 3-8(b) are found to be identical. This material is easily synthesised and readily crystallises out of both industrial HDC production methods. However, at this point it is still unclear how the hypothesised nanoparticle via Werner's complex the HDC precursor material fit together.

There are two unique ^{59}Co environments that characterise dimeric triammine $[(Co(NH_3)_3)_2(\mu\text{-}OH)_2(\mu\text{-}CO_3)](CO_3)\cdot 5H_2O$. The significant differences are due to a combination of effects in the second coordination sphere and the H-bonding scheme. These differences include could include the nature of the bonding in the bridging ligands. It was previously noted that the replacement of the carbonate ligand with water or hydroxyl would change the sign of the κ. This complex has both OH and CO_3 bridges, both ^{59}Co environments exhibit a negative κ indicating this parameter could be used as a sign of OH or H_2O ligands causing oxo coordination, but does not rule out the presence of CO_3.

An illustration of the complexes studied via ^{59}Co NMR can be seen in Figure 3-9 with the associated δ_{iso} found from the multifield analysis. From the pentammine complex up to the central fully oxo coordinated Co position of Werner's complex a stepwise change can be seen with increasing oxygen coordination. Thus, a general rule from this observation is each oxo coordinating ligand causes a shift to higher frequency of ~1000 ppm. It is difficult to comment on potential overlap of regions though. The extensive analysis of the tetrammine series where the two oxygen coordinated ligands have been varied indicates a region of ~1000 ppm.

The carbonato tetrammine series has been represented more generally in Figure 3-9, but includes results from the bromide, nitrate and sulphate complexes. The focus on the tetrammine complexes demonstrates the variation which can be seen within a single compound. The series varied by ~1000 ppm due to type of oxo coordination and anion effects. Focusing just on the carbonatotetrammine series, effects from the second order coordination sphere alone were seen to cause a disparity of ~500 ppm. Extrapolating these observations as a general guide for the addition or subtraction of oxygen coordinating ligands is fundamental for the identification of ^{59}Co complexes in the solution state studies.

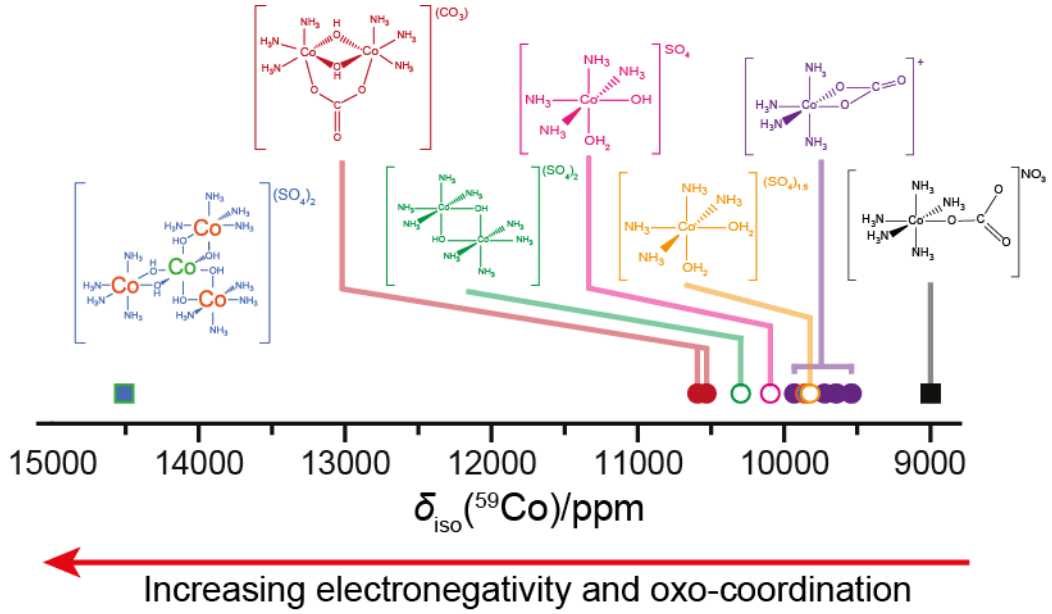

Figure 3-9: Summary of the isotropic chemical shifts for the suite of Co(III) complexes studied via solid state NMR.

Table 3-11: Summary of solid state ^{59}Co NMR parameters extracted from multiple field fittings.

Name	Peak assign-ment	δ_{iso}[a] (ppm) (±50)	δ_{11}[b] (ppm) (±20)	δ_{22}[b] (ppm) (±10)	δ_{33}[b] (ppm) (±20)	Ω[c] (ppm) (±10)	κ[c] (±0.01)	$\Delta\delta$[d] (±20)	η[d] (±0.02)	C_Q[e] (MHz) (±0.3)	η_Q[e] (±0.2)	α[f] (°) (±30)	β[f] (°) (±1)	γ[f] (°) (±50)
$[Co(NH_3)_5CO_3]NO_3{\cdot}H_2O$	-	8992	9819	9390	7767	2051	0.58	-1838	0.35	19.3	0.06	60	1	80
$[Co(NH_3)_4CO_3]Br$	-	9733	10455	9800	8944	1510	0.13	-1183	0.83	18.5	0.71	60	1	122
$[Co(NH_3)_4CO_3]NO_3{\cdot}0.5H_2O$	1	9654	10153	9928	8880	1273	0.65	-1161	0.29	18.1	0.40	37	4	117
	2	9676	10158	9971	8899	1259	0.70	-1166	0.24	18.5	0.20	10	4	46
$[Co(NH_3)_4CO_3](SO_4)_{1.5}{\cdot}1.5H_2O$	1	9700	10213	10072	8823	1390	0.80	-1320	0.16	21.3	0.10	48	5	106
	2	9553	10088	9828	8743	1345	0.61	-1215	0.32	20.8	0.30	233	3	136
$[Co(NH_3)_4(H_2O)_2](SO_4)_{1.5}{\cdot}1.5H_2O$	1	9826	11681	9157	8639	3042	-0.66	2783	0.28	43.4	0.11	154	3	95
$[Co(NH_3)_4(H_2O)(OH)](SO_4){\cdot}H_2O$	1	10098	11392	9842	9061	2331	-0.33	1941	0.6	15.8	0.81	267	12	116
$[(Co(NH_3)_4)_2(\mu\text{-}OH)_2](SO_4)_2{\cdot}H_2O$	1	10300	12116	9764	9021	3095	-0.52	2724	0.41	24.4	0.63	170	9	110
$[Co((\mu\text{-}OH)_2Co(NH_3)_4)_3](SO_4)_3{\cdot}9H_2O$	1	9895	11517	9354	8801	2715	-0.59	2439	0.34	16.3	0.60	106	1	85
	2	14518	14961	14323	14271	690	-0.85	664	0.12	3.5	0.00	0	1	0
$[(Co(NH_3)_3)_2(\mu\text{-}OH)_2(\mu\text{-}CO_3)](CO_3){\cdot}5H_2O$	1	10490	11090	10250	10130	960	-0.75	900	0.2	16.8	0.71	21	115	48
	2	10590	11329	10480	9960	1369	-0.24	1109	0.7	13.0	0.20	96	30	141

[a]–IUPAC isotropic shift convention: $\delta_{iso} = (\delta_{11} + \delta_{22} + \delta_{33})/3$.

[b]– IUPAC shift convention: $\delta_{11} \geq \delta_{22} \geq \delta_{33}$.

[c] – Herzfeld-Berger shift convention: $\delta_{11} \geq \delta_{22} \geq \delta_{33}$ (tensorial representation not shown above), $\delta_{iso} = (\delta_{11} + \delta_{22} + \delta_{33})/3$, $\Omega = (\delta_{11} - \delta_{33})$,

$\kappa = 3(\delta_{22} - \delta_{iso})/ (\delta_{11} - \delta_{33})$ $(1 \geq \kappa \geq -1)$.

[d] – Haeberlen shift convention: $|\delta_{33} - \delta_{iso}| \geq |\delta_{11} - \delta_{iso}| \geq |\delta_{22} - \delta_{iso}|$ (tensorial representation shown above), $\delta_{iso} = (\delta_{11} + \delta_{22} + \delta_{33})/3$, $\Delta\delta = \delta_{33} - 1/2(\delta_{11} + \delta_{22}) = 3/2(\delta_{33} - \delta_{iso})$,

$\eta_\delta = (\delta_{22} - \delta_{11})/ (\delta_{33} - \delta_{iso})$ $(1 \geq \eta_\delta \geq 0)$.

[e] – EFG tensor conventions: $|V_{33}| \geq |V_{22}| \geq |V_{11}|$, $C_Q = e^2qQ/h = eQV_{33}/h$, $\eta_Q = (V_{11} - V_{22})/V_{33}$ $(1 \geq \eta_Q \geq 0)$.

[f]– Angles of orientation between CSA tensor and Quadrupolar tensor in principle axes systems defining, with rotation order being ZYZ.

3.3.3 Solid State MAS Measurements of the Co(III) Complex's Ligands and Related Nuclei

3.3.3.1 ^{13}C CPMAS NMR of Carbonates

The ^{13}C CPMAS NMR data from the carbonato pentammine, tetrammine and triammine complexes are shown in Figure 3-10 with the parameters extracted from peak fitting summarised in Table 3-12. The ^{13}C resonances were observed to experience direct and indirect coupling (see Section 2.1.1.6) from nearby ^{59}Co nuclei. The two bond distance from the Co to the C causes only a small perturbation of the lineshape which lacks the resolution of individual splittings. The orientation of the EFG tensor was not known and J-coupling values presented represent approximations.

Due to the unknown orientation of the EFG simulations of the ^{13}C and ^{15}N CPMAS NMR data that was undertaken has kept α^{D} and β^{D} zero (the Euler angles between the dipolar vector with respect to V_{ZZ} in the PAS). Also, anisotropies in $^{2}J(^{59}\text{Co}, ^{13}\text{C})$ are also assumed to be zero as previous studies have recommended.[80] Thus, some discrepancies are expected but this gives a better estimation of the δ_{iso} and $^{1/2}J(^{59}\text{Co}, \text{X})$ where X is either ^{13}C or ^{15}N.

The single crystal XRD data demonstrated a variation of cobalt ligand distances. In addition, if a complex contained more than one ^{59}Co environment, identified in Section 3.3.2, then it was not possible to assign the corresponding ^{13}C environment. Thus, exact R_{DD} could not be assigned, it was observed lineshapes only required an approximate value, variations of ±20 Hz were still considered acceptable. Thus, for the tetrammine samples an R_{DD} values corresponding to 2.32 Å was used. This distance is comparable to what is seen in the structures for carbonatotetramminecobalt complexes discussed previously. Generic broadening due to dipolar interactions had the greatest control of the features, 18-40 Hz of broadening were used.

Previous studies of ^{59}Co coupling to ^{13}C in cobaltocenium salts by Heise *et al.*[79] showed that at multiple fields a manifold of the splittings can be observed when the

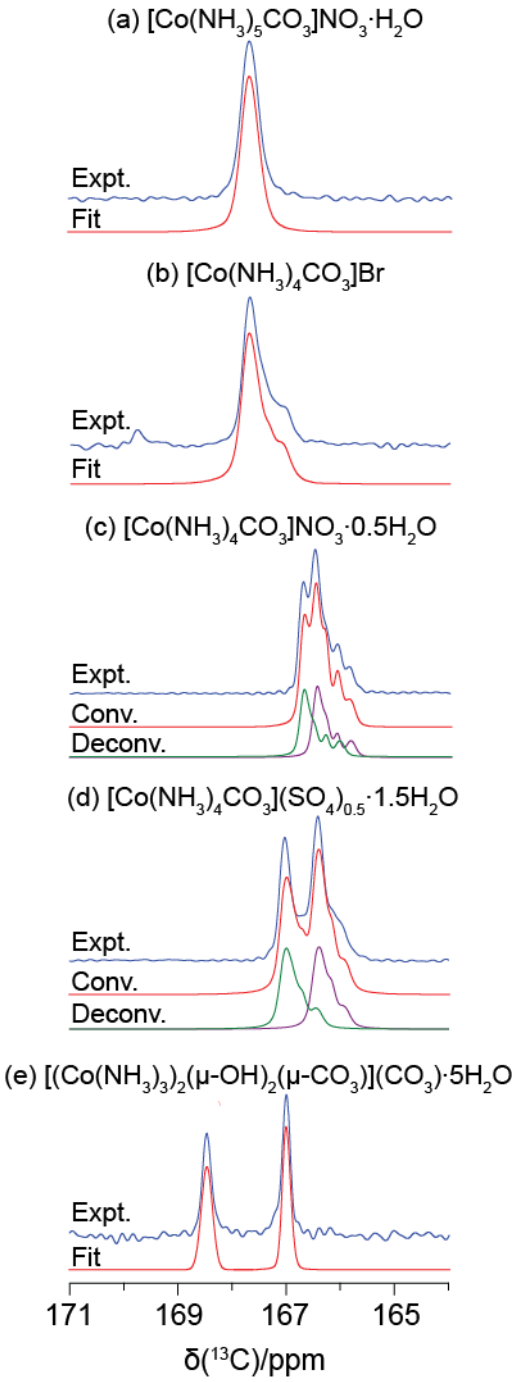

Figure 3-10: ^{13}C CPMAS solid state NMR spectra acquired at 11.7 T at an MAS frequency of 12 kHz, including: (a) $[Co(NH_3)_5CO_3]NO_3{\cdot}H_2O$, (b) $[Co(NH_3)_4CO_3]Br$, (c) $[Co(NH_3)_4CO_3]NO_3{\cdot}0.5H_2O$ and (d) $[Co(NH_3)_4CO_3](SO_4)_{0.5}{\cdot}1.5H_2O$ and (e) $[(Co(NH_3)_3)_2(\mu\text{-}OH)_2(\mu\text{-}CO_3)](CO_3){\cdot}5H_2O$.

Table 3-12: Parameters used to fit the ^{13}C solid state CPMAS data summarised in Figure 3-10.

	Site	$\delta_{iso}(^{13}C)$ (ppm) (±0.04)	R_{DD}[a] (Hz) (±20)	$^2J(^{59}Co, ^{13}C)$ (Hz) (±1)
$[Co(NH_3)_5CO_3]NO_3{\cdot}H_2O$	-	167.68	279	2
$[Co(NH_3)_4CO_3)]Br$	-	167.60	570	10
$[Co(NH_3)_4CO_3]NO_3{\cdot}0.5H_2O$	1	166.31	570	9
	2	166.54	570	10
$[Co(NH_3)_4CO_3](SO_4)_{1.5}{\cdot}1.5H_2O$	1	166.30	570	8
	2	166.88	570	5
$[(Co(NH_3)_3)_2(\mu\text{-}OH)_2(\mu CO_3)](CO_3){\cdot}5H_2O$	1	167.00	297	1
	2	168.46	-	-

[a]– Residual dipolar coupling: $R_{DD}=(\mu_0/4\pi)((\gamma_I\gamma_S h)/(4\pi^2 r^3_{IS})$

C_Q was ~170 MHz, almost eight times larger than that seen in the carbonate complexes presented here.[79]

The ^{13}C measurement of $[Co(NH_3)_5CO_3]NO_3{\cdot}H_2O$ shown in Figure 3-10(a) shows the monodentate carbonate ligand as a single site at 167.7 ppm. The single crystal data indicates a carbonate group which is arranged such the O–C–O angles are strained with one angle being 116.3(8)° coupled with an extension of the C–O bond length by ~0.025 Å could be the cause of the higher shielding than what has been reported previously for a CO_3^{2-} (168.1 ppm).[105] No indirect coupling is observed in the NMR spectrum and would indicate a chemical bonding of the carbonate ligand more ionic than covalent in nature.

With an δ_{iso} of 167.6 ppm (Table 3-12) the carbonate shift of $[Co(NH_3)_4CO_3)]Br$ is much closer to free carbonate despite being under significant strain, with the bidentate nature of the carbonate ligand forcing an O–C–O angle to ~110 °. A study of the tetrammine complexes presented in Figure 3-10 shows that the carbonate is significantly deshielded (Figure 3-10(b)) compared to the nitrate and sulphate complexes. This is not unexpected when the ^{59}Co parameters were also very different, specifically the η_Q which was 0.71. However, the literature reports that this carbonate H-bonds to an ammine group (which has another ammine *trans* to itself) which is

part of a neighbouring complex.[101,106] This H-bonding must deshield the carbonate, compared to the other tetrammine complexes.

From the ^{59}Co measurements the tetrammine complexes with sulphate and nitrate anions were very similar and both contained two ^{59}Co environments. This has been confirmed in the ^{13}C measurements, where as shown in Figure 3-10(c) and (d) the spectra were fitted with two ^{13}C sites. The nitrate complex still maintains features due to the direct coupling to ^{59}Co, this may be due to the smaller nitrate anion and smaller quadrupole interaction. However, as with the ^{59}Co measurements the largest separation between ^{13}C environments is seen in the sulphate complex.

From the structure data discussed in Section 3.3.1 the sulphate material, $[Co(NH_3)_4CO_3](SO_4)_{1.5}\cdot 1.5H_2O$, had C–O distances ~1.320 Å for the bound oxygen of the bidentate carbonate. This distance was similar for both inequivalent complexes. However, the unbound C–O distance was either 1.228(2) Å or 1.236(2) Å. This reflects differences in the H-bonding altering the bond length and thus giving rise to two chemical shifts. A similar comparison for the nitrate cannot be made because the sensitivity of the reported structure is insufficient to accurately quantify the difference in C–O bond lengths which were 1.257(8) Å and 1.243(8) Å.[99]

Finally, the ^{13}C CPMAS measurements of the HDC material, $[(Co(NH_3)_3)_2(\mu\text{-}OH)_2(\mu\text{-}CO_3)](CO_3)\cdot 5H_2O$, can be seen in Figure 3-10(e). Both the bridging CO_3 and anion were observed at 167.0 ppm and 168.5 ppm. The unbound anion is more deshielded than the carbonate anion reported in literature. Thus, electron density has been drawn away due to the H-bonding scheme. It is also this H-bonding scheme which appears to broaden the resonance compared to the bound carbonate.

The carbonate bridge is of interest, from the structure analysis discussed previously (Section 3.3.1), similarities to the carbonate ligands of the pentammine and tetrammine complexes were observed. This is reflected in the chemical shift which is in between both types at 167.0 ppm. However, no spin-spin coupling with the ^{59}Co was observed thus indicating the bonding of this bridging ligand is ionic rather than covalent in nature more so that in the pentammine case due to the decreased

linewidth. The observations of ionic nature for monodentate and when the carbonate is bound to multiple cations and the introduced covalence when in a bidentate configuration is in keeping with previous carbonate studies.[107]

3.3.3.2 ^{15}N CPMAS Measurements of Ammine Ligands

From the ^{15}N CPMAS measurements undertaken all samples exhibited distinct environments due to *cis-trans* effects. The assignment of *cis* and *trans* has been illustrated in Figure 3-11(a) for all tetrammine complexes. For clarity, the pentammine complex, Figure 3-11(b), and the dimeric triammine complex, Figure 3-11(c), assignments were labelled axial and equatorial. The illustration shown in Figure 3-11 does not show an accurate orientation of the ligands as was presented in Section 3.3.1.

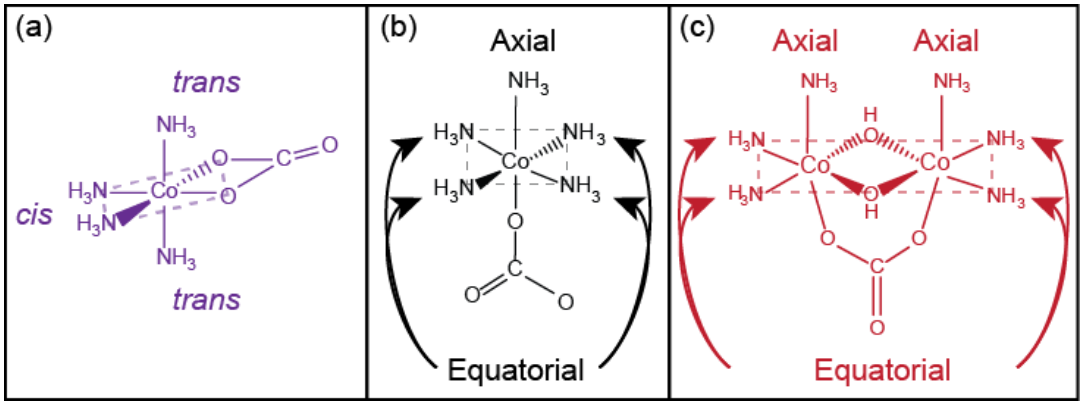

Figure 3-11: An illustrative assignment of ammine groups observed in ^{15}N CPMAS measurements. All tetrammine complexes are assigned the same as (a), where the *cis* ammine groups are in a plane (dashed rectangle) with the oxo coordinated ligands and the *trans* ligands lay out of the plane. The dashed rectangles represent an arbitrary plane and angles of ligands are not accurate. For clarity, the terms 'axial' and 'equatorial' are used for the pentammine complex (b) and the dimeric triammine complex (c).

Acquisition of ^{15}N CPMAS data was acquired for the full suite of Co(III) complexes and is shown in Figure 3-12. Assignment of *cis* and *trans* to the ammine ligands was made such; ligands which have another ammine in a *trans* configuration were more deshielded than those with ammine groups only in *cis* positions. This has been observed by P. Kofod for a range of Co(III) complexes in solution via ^{14}N NMR.[108] The solution ^{14}N data reported previously provides chemical shift information and an

extensive discussion of *cis* and *trans* reporting chemical shifts to be -416.7 ppm and -436.7 ppm respectively for $[Co(NH_3)_4CO_3]^+$. However, the significant full-width-half maximum values measured in solution were attributed to the quadrupolar nature

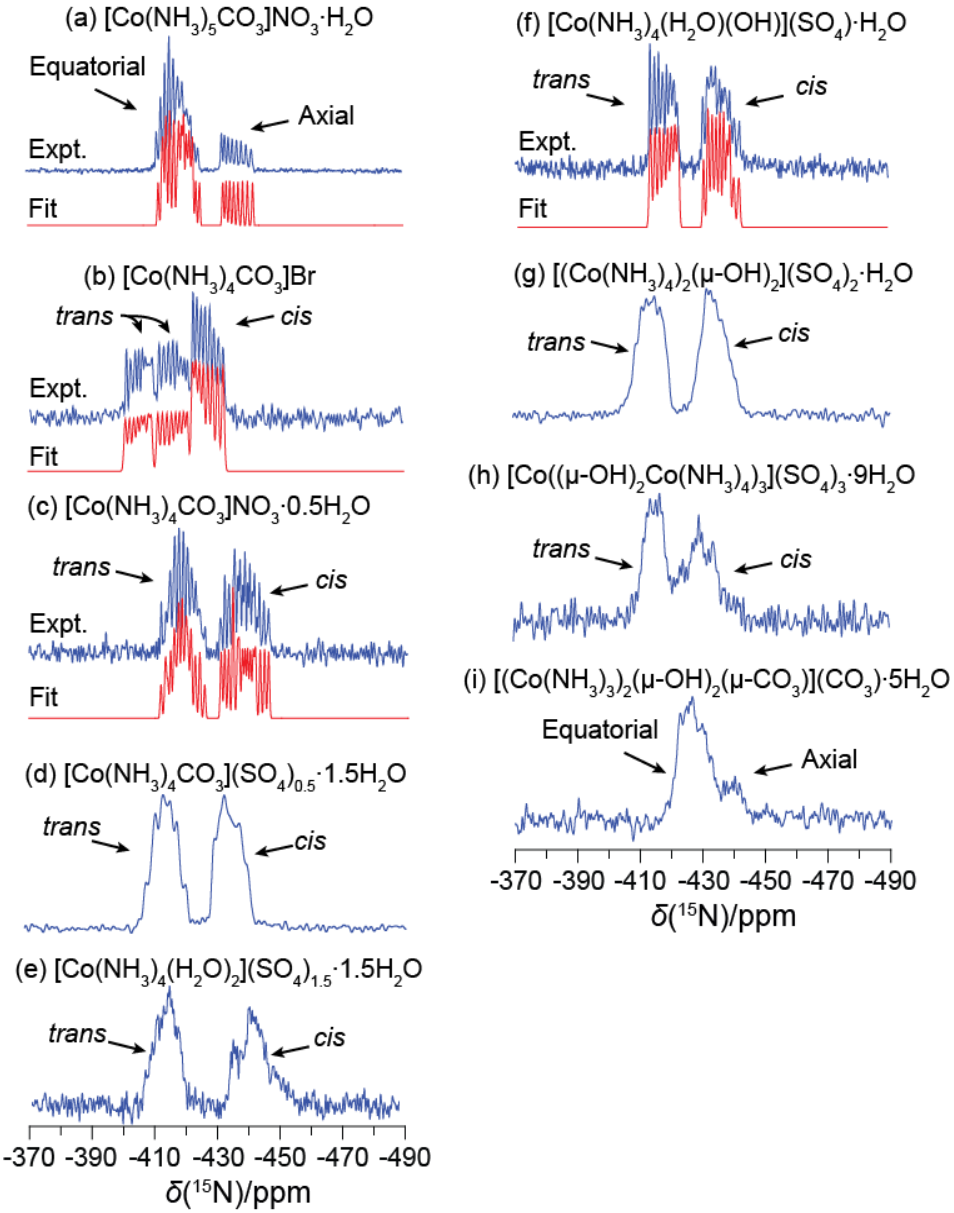

Figure 3-12: ^{15}N CPMAS measurements at 11.7 T and an MAS speed of 12 kHz where possible experimental lines were fitted using WSOLIDS with parameters summarised in Table 3-13. The ^{15}N measurements are shown for: (a) $[Co(NH_3)_5CO_3]NO_3{\cdot}H_2O$, (b) $[Co(NH_3)_4CO_3]Br$, (c) $[Co(NH_3)_4CO_3]NO_3{\cdot}0.5H_2O$, (d) $[Co(NH_3)_4CO_3](SO_4)_{0.5}{\cdot}1.5H_2O$, (e) $[Co(NH_3)_4(H_2O)_2](SO_4)_{1.5}{\cdot}1.5H_2O$, (f) $[Co(NH_3)_4(H_2O)(OH)](SO_4){\cdot}H_2O$, (g) $[Co(NH_3)_4(\mu\text{-}OH)_2](SO_4)_2{\cdot}H_2O$, (h) $[Co((\mu\text{-}OH)_2Co(NH_3)_4)_3](SO_4)_3{\cdot}9H_2O$ and (i) $[(Co(NH_3)_3)_2(\mu\text{-}OH)_2(\mu\text{-}CO_3)](CO_3){\cdot}5H_2O$.

of ^{14}N, where as in the solid state it is clear there is a significant spin-spin coupling interaction between the ^{15}N and ^{59}Co.

The significant linewidths and splittings observed in the ^{15}N of cobalt ammine complexes can be seen to be due to spin-spin coupling between the ^{15}N and ^{59}Co where the eight-predicted components of the $^{1}J(^{59}Co,^{15}N)$ multiplet are clearly resolved in Figure 3-12(a–c) and (f). Often the ligands in the *cis* and *trans* groups were inequivalent causing an overlap of the multiplets thus an accurate value of $^{1}J(^{59}Co,^{15}N)$ was not possible. Furthermore, $^{1}J(^{59}Co,^{15}N)$ typically varied between 60 and 70 Hz, negative signs were assigned to attempt to reproduce intensity variations. However, values should be considered as magnitudes due to the lack of other parameters.

Exact assignment of the ligands from single crystal XRD measurements could not be assigned. As with the ^{13}C CPMAS measurement previously approximate R_{DD} values were used (summarised in Table 3-13). As with the ^{13}C measurements undertaken previously, NMR parameters extracted from the ^{15}N CPMAS data are approximate, but prove to be informative.

Unlike the ^{13}C CPMAS measurements on the carbonate ligand of the pentammine complex, $[Co(NH_3)_5CO_3]NO_3{\cdot}H_2O$, the ^{15}N measurements seen in Figure 3-12(a) show clear indirect spin coupling with an approximate intensity distribution of 4:1. This observation infers that a different bonding arrangement can be distinguished for the NH_3 moieties surrounding the Co position. Thus, the ammine ligands are bonding has been shown to be more covalent in nature than the bonding of the carbonate. The different types of bonding are attributed to the large span (Ω) seen in the ^{59}Co measurements.

The ammine ligand which is axial with the carbonate (*cis* to all other ammine groups) demonstrates all eight quantum transitions resolved with an δ_{iso} of -436.9 ppm. The four ammine ligands in the equatorial positions (shown in Figure 3-11(b)) demonstrate in-equivalence though. Demonstrating the difficulty to distinguish individual sites within the manifold. Inequivalence was observed in the Co–N bond

Table 3-13: Summary of ^{15}N parameters acquired via CPMAS (12 kHz MAS), if fittings are missing in Figure 3-12 then a centre of gravity shift is given rather than an δ_{iso}.

	Site	**δ_{iso}(^{15}N) (ppm)** (±0.2)	**R_{DD}[a] (Hz)** (±30)	**^1J(^{59}Co, ^{15}N) (Hz)** (±3)
$[Co(NH_3)_5CO_3]NO_3{\cdot}H_2O$	1	-416.4	-383	-72
	2	-417.4	-383	-65
	3	-417.8	-383	68
	4	-421.5	-383	56
	5	-436.9	-383	69
$[Co(NH_3)_4CO_3)]Br$	1	-405.6	-402	60
	2	-416.5	-374	-66
	3	-427.0	-376	-70
$[Co(NH_3)_4CO_3]NO_3{\cdot}0.5H_2O$	1	-413.1	-383	58
	2	-413.4	-383	55
	3	-415.9	-383	-56
	4	-417.4	-383	54
	5	-430.7	-392	68
	6	-435.4	-392	-75
$[Co(NH_3)_4CO_3](SO_4)_{1.5}{\cdot}1.5H_2O$	1	-414.1	-	-
	2	-435.1	-	-
$[Co(NH_3)_4(H_2O)_2](SO_4)_{1.5}{\cdot}1.5H_2O$	1	-414	-	-
	2	-443	-	-
$[Co(NH_3)_4(H_2O)(OH)](SO_4){\cdot}H_2O$	1	-418.0	-342	65
	2	-435.0	-360	-62
	3	-436.6	-360	-73
$[(Co(NH_3)_4)_2(\mu\text{-}OH)_2](SO_4)_2{\cdot}\ H_2O$	1	-413.5	-	-
	2	-434.0	-	-
$[Co((\mu\text{-}OH)_2Co(NH_3)_4)_3](SO_4)_3{\cdot}9H_2O$	1	-415.0	-	-
	2	-432.5	-	-
$[(Co(NH_3)_3)_2(\mu\text{-}OH)_2(\mu CO_3)](CO_3){\cdot}5H_2O$	1	-427.2	-	-
	2	-439.3	-	-

[a]– Residual dipolar coupling: $R_{DD}=(\mu_0/4\pi)((\gamma_I\gamma_S h)/(4\pi^2 r^3_{IS})$

lengths (see Table 3-2) which corroborates these differences in which the isotropic shifts which vary by 5.1 ppm. All fitting parameters are summarised in Table 3-13, the $^{1}J(^{59}Co,^{15}N)$ are between 56 Hz and 72 Hz which are comparable to previously reported values.[80]

The only complex to demonstrate three distinct fully resolved ^{15}N resonances was the $[Co(NH_3)_4CO_3]Br$ complex shown in Figure 3-12(b). This is in agreement with a single crystal study which also resolved three unique environments.[106] With an intensity ratio of 1:1:2 the *cis* ligands can be seen to be equivalent with an δ_{iso} of -427.0 ppm even though the Co–N were slightly different in the structure. They are also more deshielded than what was seen in any other complex, due to their proximity to the bromide anion. Thus, one of the *trans* ligand H-bonds to the bromide anion and the other to the oxygen of a neighbouring complex's carbonate group. The ammine H-bonded to the bromide anion is unique within the complex suite and can be assigned to the resonance at -405.6 ppm (the most deshielded ^{15}N resonance observed) and the other *trans* ammine to occupy the middle position at -416.5 ppm.

The final two carbonatotetrammine complexes exhibit structures that appear to be very similar, however, Figure 3-12(c) and (d) show where these complexes begin differ. With two ^{59}Co environments the typical *cis* and *trans* arrangement is complicated with each group containing 2-4 slightly different N environments. This can be observed in Table 3-13, where six sites were required to simulate Figure 3-12(c). The sulphate though could not be similarly treated due to the lack of resolution and defined splittings. The *trans* and *cis* groups appear to be slightly narrower in the sulphate complex potentially indicating $^{1}J(^{59}Co, ^{15}N)$ which would reduce the splitting separation. Thus, reducing the resolvable resolution of the individual splittings.

Apart from the ^{15}N CPMAS measurements of $[Co(NH_3)_4(H_2O)(OH)](SO_4)\cdot H_2O$ (Figure 3-12(f)) it was observed that high resolution data was not achievable for the remaining systems. However, from a qualitative perspective information and insight is still obtainable. Although CPMAS is not strictly a quantitative technique, it is a

good indicator for structural moieties which exhibit similar contact conditions. The removal of the bidentate carbonate and replacement with water ligands can be seen to significantly affect the nitrogen, shown in Figure 3-12(e). Both *trans* and *cis* groups have an intensity ratio of 1:1 such only a configuration with the water ligands *cis* to one another exists. Thus, no isomerisation occurred with the removal of the bidentate carbonate. The low frequency *cis* group may contain two ^{15}N sites which experience very different indirect coupling; a narrow site at ~-443 ppm and one which is highly perturbed by the ^{59}Co. Thus, the Co–N bond distance of the two *cis* ligands may be very different which would indicate they both experience unique residual dipolar couplings (R_{DD}). The observation of a single isomer, with the oxo coordinating ligands in a *cis* configuration, also holds true for the $[Co(NH_3)_4(H_2O)(OH)](SO_4)\cdot H_2O$ complex, Figure 3-12(f).

The dimeric complex $[Co(NH_3)_4(\mu\text{-}OH)_2](SO_4)_2\cdot H_2O$, shown in Figure 3-12(g) was observed to have similar draw backs to $[Co(NH_3)_4CO_3](SO_4)_{0.5}\cdot 1.5H_2O$ with resolution of the indirect coupling being lost and no significant residual dipolar coupling. The narrowing of the ^{15}N groups may be due to longer Co–N bonds as seen in the structure of $[Co(NH_3)_4(\mu\text{-}OH)_2](SO_4)_2\cdot 2H_2O$ which would cause reduced residual dipolar coupling.

Reduction in the N content, and the highly perturbed *cis* resonance limited the resolution of the ^{15}N data of Werner's complex, $[Co((\mu\text{–}OH)_2Co(NH_3)_4)_3](SO_4)_3 \cdot 9H_2O$, shown in Figure 3-12(h). The intensity variation across the *cis* resonance would indicate conditions similar to $[Co(NH_3)_4(H_2O)(OH)](SO_4)\cdot H_2O$ seen in Figure 3-12(e). Thus, two *cis* resonances may exist due experiencing different residual dipolar couplings due to very different Co–N bond distances. The distortion of these bond distances would be due to the complex H-bonding scheme with the nine waters of crystallisation. The disorder of the sulphate anion, seen in the single crystal XRD, may also translate to the ammine ligands through the H-bonding scheme.

Finally, the ^{15}N CPMAS measurement of the industrial sample $[(Co(NH_3)_3)_2(\mu\text{-}OH)_2(\mu\text{-}CO_3)](CO_3)\cdot 5H_2O$ is shown in Figure 3-12(i). The increase in oxo coordination of the complex reduced the difference between the axial and equatorial groups. The reduced distinction between the two groups can be attributed to the ammine groups *cis* configuration. Thus, the differences now arise due to the varying number of oxygen *trans* to the ammine groups. Thus, the intensity is split such the downfield site (2 ammine groups) -427.2 ppm are the equatorial ammines (see Figure 3-11) *trans* to the OH bridges. Finally, the axial ammine group *trans* to the carbonate bridge was observed at ~-439.3 ppm. Differences within these groups would be expected due to the two inequivalent ^{59}Co NMR environments identified previously.

3.3.3.3 ^{1}H MAS Measurements

Single pulse ^{1}H measurements of the Co(III) complexes were undertaken, the data has been summarised in Figure 3-13. Deconvolution of the separate ^{1}H sites has been attempted by quantitatively analysing the ratios of expected proton species of each complex from their chemical formula. The quantitative break down of the experimental fits can be found in Table 3-14. Solution state ^{1}H measurements of Co(III) ammine complexes has been carried out previously identifying *cis-trans* speciation of protons bonded to the ammine ligands.[109] However, the extent of this shift can vary due to influences from the Co nucleus.[110-112]

From the ^{1}H NMR measurements of $[Co(NH_3)_5CO_3]NO_3\cdot H_2O$, $[Co(NH_3)_4CO_3]Br$ and $[Co(NH_3)_4CO_3]NO_3\cdot 0.5H_2O$ shown in Figure 3-13(a-c) several isolated observations can be made, these effects become convoluted later in the data set. Firstly, the pentammine complex, $[Co(NH_3)_5CO_3]NO_3\cdot H_2O$, which contains only H_2O and ammine protons at 3.8 ppm and 5.0 ppm. The decreased intensity of the water resonance (theoretically 11.7%) could be due to saturation of the NMR signal due to insufficient relaxation. Alternatively, the reported synthesis method indicates a crystal with no crystallographic water is possible.[85] Although, the ^{59}Co NMR measurements identified a single environment the ^{1}H NMR is far more sensitive. Thus, the sample may be predominantly hydrated and contain a low abundance

dehydrated phase. This may explain the discrepancy between the $[Co(NH_3)_5CO_3]NO_3{\cdot}0.5H_2O$ compound expected from the synthesis and the

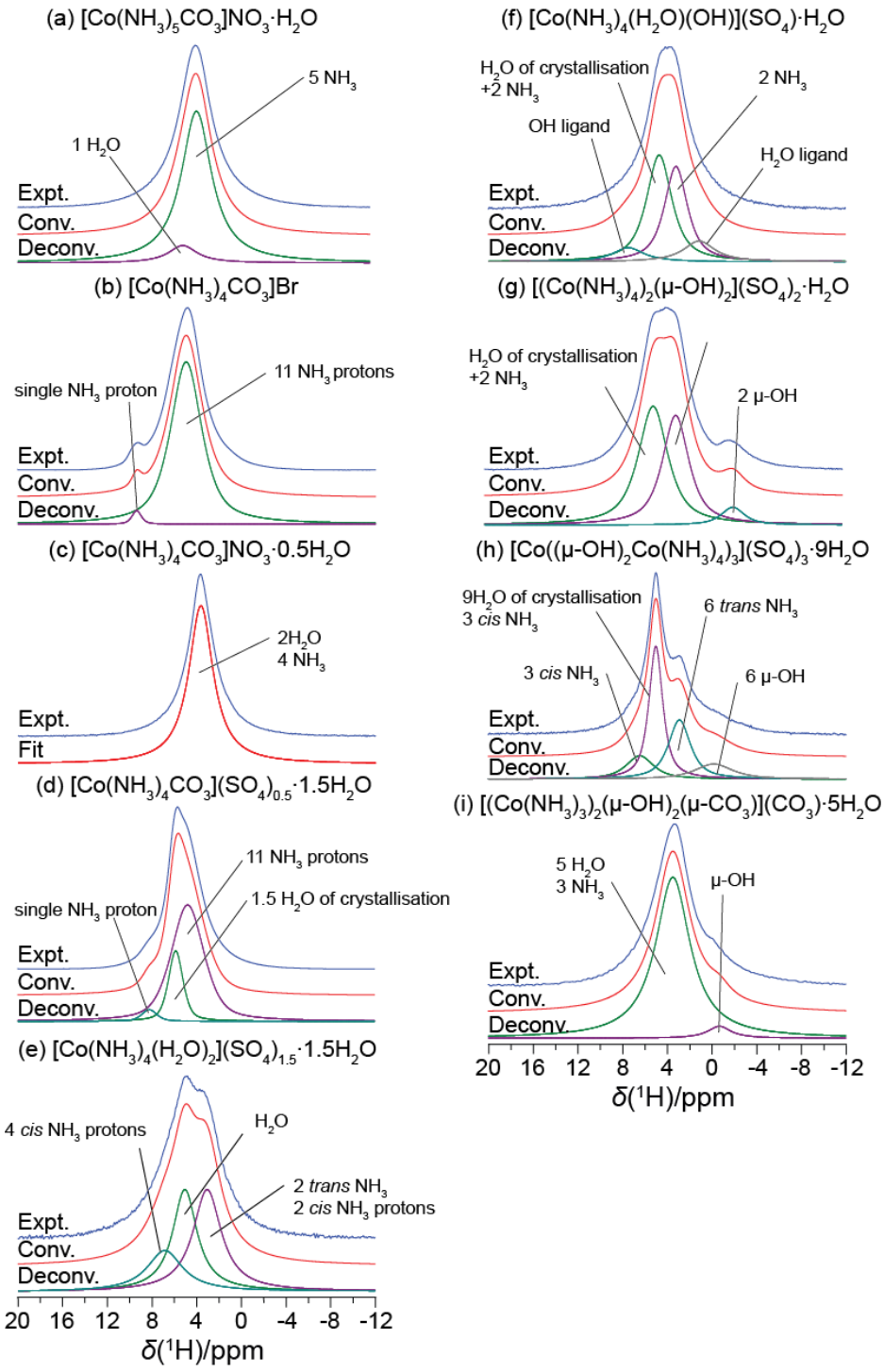

Figure 3-13: Single pulse ^{1}H 30 kHz MAS measurements of Co(III) complexes at 14.1 T of the full complex suite.

$[Co(NH_3)_5CO_3]NO_3{\cdot}H_2O$ verified via single crystal XRD measurements.

Containing no crystallographic water, the complex $[Co(NH_3)_4CO_3]Br$ can be seen in Figure 3-13(b) to have two distinct ^{1}H environments. The ^{15}N CPMAS measurements showed clearly the *trans* ammine ligands were unique. Thus, the resonance at 9.4 ppm is the highly deshielded proton H-bonding to the bromide anion. However, predominantly the ammine protons are observed at 5.0 ppm. Thus, the resolution of the ^{1}H measurements presented here may be insufficient to distinguish the proton resonances from ammine and H_2O (ligands or otherwise). This is clearly demonstrated in $[Co(NH_3)_4CO_3]NO_3{\cdot}0.5H_2O$, Figure 3-13(c), where the only signal observed was at 3.6 ppm. With increased MAS, the homonuclear dipolar broadening may be removed sufficiently to separate the resonances.

Unlike the previous complex $[Co(NH_3)_4CO_3](SO_4)_{0.5}{\cdot}1.5H_2O$, Figure 3-13(d) demonstrates three distinguishable resonances. Firstly, at 4.8 ppm are ammine ligands with no H-bonding, theoretically 73%, H_2O was identified at 5.8 ppm (theoretically 20%) and an ammine proton shifted by H-bonding (6%) at 8.21 ppm. The strong H-bonding seen for $[Co(NH_3)_4CO_3](SO_4)_{0.5}{\cdot}1.5H_2O$, may explain previous NMR observations. For example, the reduced resolution within the ^{13}C and ^{15}N CPMAS data and the greater separation of ^{59}Co environments, relative to the corresponding $[Co(NH_3)_4CO_3]NO_3{\cdot}0.5H_2O$ NMR measurements.

Exchanging the carbonate ligands for water and hydroxyls further complicates the analysis. Firstly, $[Co(NH_3)_4(H_2O)_2](SO_4)_{1.5}{\cdot}1.5H_2O$, shown in Figure 3-13(e), required three proton environments to reproduce the lineshape, with water contributing to 46% of the ^{1}H NMR signal. The output shown in Table 3-14 has been assigned such: at 3.1 ppm are the *trans* ammine ligands including 2 *cis* ammine protons; 5.1 ppm contains the waters of crystallisation and the water ligands; 6.84 ppm is the remaining *cis* ammine protons. Theoretically, this assignment yields relative amounts of 42.1%, 36.8% and 21.1% respectively which is very close to the measured values in Table 3-14.

Shown in Figure 3-13(f), the ^{1}H NMR measurements of the $[Co(NH_3)_4(H_2O)(OH)](SO_4)\cdot H_2O$ complex demonstrate a relatively featureless lineshape. Two and three sites were insufficient to replicate the flattening of the peak and tailing at high and low frequencies. Thus, four sites were required representing the OH ligand, H_2O ligand, crystallised H_2O and ammine ligands. The chemical formula indicates a total of 17 protons making one proton ~6% of the total observed signal. Interestingly, this would make the two extremes a highly-shielded water at 1.10 ppm, and a deshielded hydroxyl at 7.45 ppm. The two central resonances have an intensity spilt of approximately 4:3, and has required two of the protons of the ammine ligands to be split into two groups. From the relative intensities two ammine groups are at 3.2 ppm and the other two ammine groups plus the H_2O of crystallisation are at 4.7 ppm. The separation of the ammine resonance into pairs would indicate *cis-trans* effects.

Table 3-14: Chemical shift and quantitative analysis of the proton speciation, found from the ^{1}H MAS NMR measurements of the Co(III) complex sample suite.

	Peak assignment	**$\delta_{iso}(^{1}H)$/ppm** (±0.1)	**Integrated intensity/%** (±0.5)
$[Co(NH_3)_5CO_3]NO_3\cdot H_2O$	1	3.8	90.2
	2	5.0	9.4
$[Co(NH_3)_4CO_3]Br$	1	5.0	97.7
	2	9.4	2.3
$[Co(NH_3)_4CO_3]NO_3\cdot 0.5H_2O$	-	3.6	100.0
$[Co(NH_3)_4CO_3](SO_4)_{0.5}\cdot 1.5H_2O$	1	4.8	76.0
	2	5.8	20.5
	3	8.2	3.5
$[Co(NH_3)_4(H_2O)_2](SO_4)_{1.5}\cdot 1.5H_2O$	1	3.1	42.2
	2	5.1	36.4
	3	6.8	21.4
$[Co(NH_3)_4(H_2O)(OH)](SO_4)\cdot H_2O$	1	1.1	11.6
	2	3.2	36.0
	3	4.7	44.5
	4	7.5	7.9
$[(Co(NH_3)_4)_2(\mu\text{-}OH)_2](SO_4)_2\cdot H_2O$	1	-2.2	6.0
	2	2.9	43.5
	3	4.9	51.6
$[Co((\mu\text{-}OH)_2Co(NH_3)_4)_3](SO_4)_3\cdot 9H_2O$	1	-0.2	13.2
	2	2.9	29.9
	3	5.0	42.2
	4	6.4	14.6
$[(Co(NH_3)_3)_2(\mu\text{-}OH)_2(\mu CO_3)](CO_3)\cdot 5H_2O$	1	-0.7	4.7
	2	3.5	95.3

It is the *cis trans* effects and symmetry which makes it possible to deconvolute the dimeric compound $[Co(NH_3)_4(\mu\text{-}OH)_2](SO_4)_2\cdot H_2O$ which has been assigned three sites. The resonance at -2.33 ppm is attributed to highly shielded bridging hydroxyls and is in keeping with other complexes which contain them. The ^{59}Co measurements indicated a single environment which means both halves of the dimer will perturb in the same way. Thus, the ratio of 43.5:51.6 for those at 2.9 ppm and 4.9 ppm indicates an ~50/50 split (accounting for the single H_2O at 4.9 ppm). Thus, the ^{1}H are experiencing different shifts whether on a *cis* or *trans* ammine, as seen before.

Werner's complex, $[Co((\mu\text{-}OH)_2Co(NH_3)_4)_3](SO_4)_3\cdot 9H_2O$, shows the most resolution amongst the complex series despite observations made from the ^{15}N CPMAS data. The complex is shown in Figure 3-13(h) and four sites were identified. The OH bridges made up ~10% (theoretically) of the signal were observed at -0.17 ppm and the *trans* ammines were at 2.9 ppm (6 ligands). The Werner's complex ^{15}N CPMAS data alluded to two *cis* ammine ligand species. Thus, the six *cis* ammine ligands are split equally between the resonances at 5.0 ppm and 6.4 ppm supporting the hypothesis of H-bonding perturbing the bond lengths. The partial crystal structure discussed previously did not identify a difference in the Co–N distance where both were reported to be 1.965(8) Å. However, the ^{15}N CPMAS and ^{1}H NMR data indicate a definite difference between the *cis* ammine ligands.

Finally is the industrial $[(Co(NH_3)_3)_2(\mu\text{-}OH)_2(\mu\text{-}CO_3)](CO_3)\cdot 5H_2O$ which is shown Figure 3-13(i). There was no discernible difference between ammine ligands and the H_2O within the structure. However, there is a negatively shifted resonance at -0.7 ppm which is in keeping with what has previously been seen for hydroxyl bridges in the previous Co(III) complexes. Finally, the highly-shielded hydroxyl and water ligands cause the change in the sign on the κ observed in the ^{59}Co NMR data.

3.4 Conclusions

In summary, single crystal XRD studies, identified the dimeric triammine complex $[(Co(NH_3)_3)_2(\mu\text{-}OH)_2(\mu\text{-}CO_3)](CO_3)\cdot 5H_2O$, from the HDC catalyst preparation (Co

metal precursor method). Furthermore, a dimeric complex, $[Co(NH_3)_4(\mu\text{-}OH)_2](SO_4)_2{\cdot}2H_2O$, was identified as an intermediate in the synthesis of Werner's complex, $[Co((\mu\text{-}OH)_2Co(NH_3)_4)_3](SO_4)_3{\cdot}9H_2O$. Across all complexes measured by XRD, Co–N bonds ranged from 1.931(5)-1.979(9) Å, whilst Co–O bonds ranged from 1.893(4)-1.939(6) Å. Thus, an overlap was present in some Co(III) complexes. Although overlap of distances was possible as with $[Co(NH_3)_5CO_3]NO_3{\cdot}H_2O$ typically Co–O were shorter than Co–N in a single complex. Furthermore, it was observed carbonate ligands in monodentate and bridging moieties adopted relaxed configurations (O–C–O angles of ~120˚) compared to bidentate ligands. The sample $[Co(NH_3)_4CO_3](SO_4)_{0.5}{\cdot}1.5H_2O$ for example exhibited an O–C–O angles of ~110˚ between the O bound to the Co centre.

The sensitivity of ^{59}Co NMR was demonstrated where even small distortions of surrounding bond lengths shown by single crystal XRD were observed to influence the CSA and quadrupolar interactions. Utilising ^{59}Co NMR confirmed the Co(III) ammine complex isolated from the $CoCO_3$ precursor HDC catalyst synthesis was also $[(Co(NH_3)_3)_2(\mu\text{-}OH)_2(\mu\text{-}O_3)](CO_3){\cdot}5H_2O$. The pentammine complex was observed at 8992 ppm and full the fully oxo coordinated core of Werner's complex was at 14518 ppm. Thus, each oxygen increased the chemical shift by 700-800 ppm. Thus, oxo coordination was observed to systematically increase the isotropic chemical shift, δ_{iso}, in a stepwise fashion. Focus on the series of tetrammine complexes indicates variation can occur depending on the oxygen donating ligand and from effects beyond the first coordination sphere. Finally, the skew of the CSA interaction, κ, was observed to change signs with the presence of hydroxyl or water ligands compared to when only a carbonate ligand was present.

Sharing many similarities with the tetrammine counterpart, the pentammine complex $[Co(NH_3)_4CO_3]NO_3{\cdot}H_2O$, featured a larger span (Ω) of 2051 ppm. This was attributed to the different bonding nature of the CO_3 ligand where here it was more ionic in nature, supported by the lack of spin-spin coupling observed in the ^{13}C CPMAS data. The lack of spin-spin coupling was also observed in the bridging carbonate of $[(Co(NH_3)_3)_2(\mu\text{-}OH)_2(\mu\text{-}CO_3)](CO_3){\cdot}5H_2O$. However, when in a

bidentate configuration, carbonate ligands experienced spin-spin coupling to the ^{59}Co nucleus was observed indicating the bonding was more covalent in nature.

All ^{15}N CPMAS measurements of ammine ligands were observed to experience spin-spin coupling to the ^{59}Co nuclei indicating the covalency of the bonding. The ammine ligands were also observed to experience *cis*-*trans* groupings. However, within a group ligands were typically inequivalent which caused difficulties deconvoluting the characteristic multiplets. The carbonatotetrammine complex, $[Co(NH_3)_4CO_3]Br$, was significantly different to other Co(III) complexes. Due to the H-bonding of an ammine ligand to the bromide anion a distinction between the *trans* groups was observed. The result was three well separated multiplets with an approximate intensity ratio of 1:1:2.

Furthermore, from the ^{15}N CPMAS data $[Co(NH_3)_4(H_2O)_2](SO_4)_{0.5}\cdot 1.5H_2O$ and Werner's complex were thought to contain two distinct *cis* environments, despite the poor resolution of the spectra. This was corroborated by the ^{1}H MAS NMR, which also demonstrated a possible separation of the corresponding proton resonances, depending on which *cis* ammine they belonged to. Thus, it was concluded one of the *cis* ammine ligands had longer N–H bond lengths than the other, due to stronger H-bonding. Finally, ^{1}H MAS measurements also identified that bridging hydroxyls were highly shielded, demonstrated by negative isotropic chemical shifts. This was contrary to protons of ammine ligands involved in H-bonding which became more deshielded.

Chapter 4 Determination of Co Oxide Nanoparticle Precipitation

4.1 Background

From the study of the Co(III) complexes isolated in the solid state, the NMR characterisation demonstrated the significant influence of H-bonding and effects from the second order coordination sphere. Discussion will continue by focusing on the solid state NMR observations which are transferable to the solution state NMR studies.

4.1.1 Identifying Co(III) Complexes

The two routes to produce HDC catalysts utilise the precursors $CoCO_3$ or Co metal. The solid state studies have shown the Co(III) ammine complex from the highly dispersed Co (HDC) catalyst synthesis was the same in both synthesis methods. This was identified as $[(Co(NH_3)_3)_2(\mu\text{-}OH)_2(\mu\text{-}CO_3)](CO_3)\cdot 5H_2O$ from the solid state studies. The observation of a carbonate bridge may indicate the ligand plays a more significant role in nanoparticle precipitation than previously hypothesised. Characterisation of the complex has been carried out via single crystal XRD, ^{59}Co, ^{15}N, ^{13}C and ^{1}H solid state NMR.

An updated hypothesis for the precipitation of Co oxide nanoparticles is shown in Figure 4-1. The diagram includes both $[(Co(NH_3)_3)_2(\mu\text{-}OH)_2(\mu\text{-}CO_3)](CO_3)\cdot 5H_2O$ and the dimeric complex $[Co(NH_3)_4(\mu\text{-}OH)_2](SO_4)_2$. However, if the production of Co_3O_4 comes from a Werner's type derivative, as hypothesised, it is still unclear where in the synthesis $[(Co(NH_3)_3)_2(\mu\text{-}OH)_2(\mu\text{-}CO_3)](CO_3)\cdot 5H_2O$ occurs, as

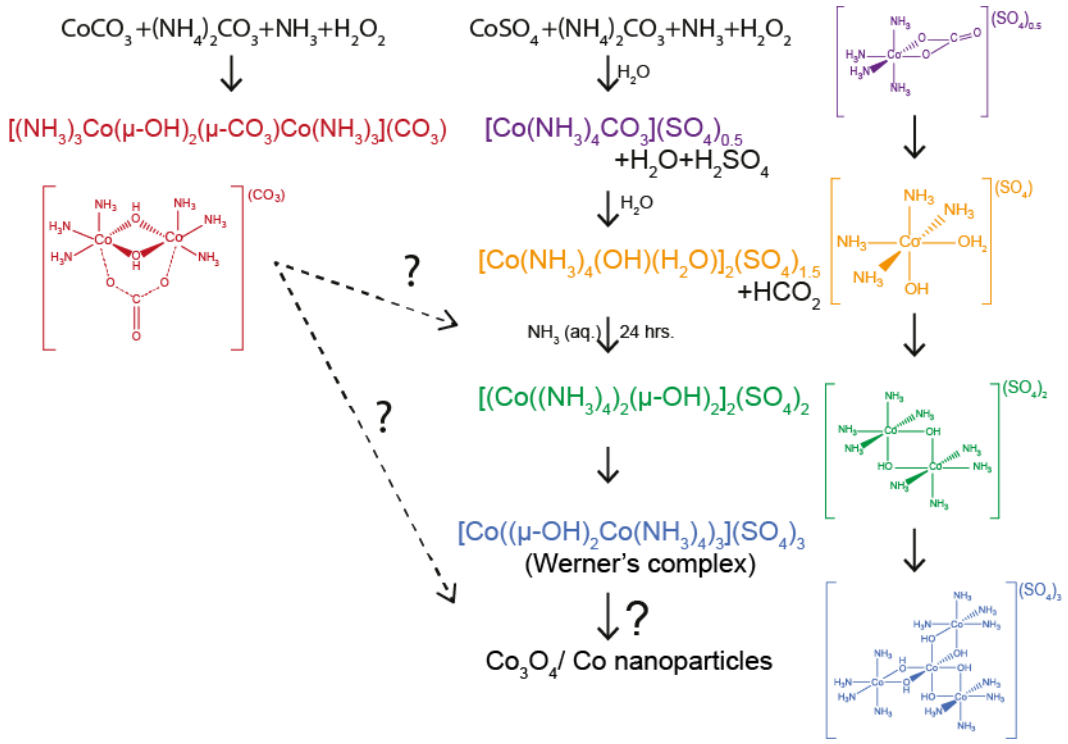

Figure 4-1: Illustration of proposed Co oxide nanoparticle synthesis from Werner's complex and the unknown role of $[(Co(NH_3)_3)_2(\mu\text{-}OH)_2(\mu\text{-}CO_3)](CO_3)\cdot 5H_2O$.

illustrated by the dashed arrows in Figure 4-1. The additional intermediate of $[Co(NH_3)_4(\mu\text{-}OH)_2](SO_4)_2$, seen from single crystal XRD, could provide a potential pathway though.

The ^{59}Co chemical shift scale showing the variation of isotropic chemical shift with oxo coordination has been updated in Figure 4-2. The ionic bonding of the bridging and monodentate carbonate ligands discussed in Section 3.3.3.1 has been shown via dashed lines. Beyond what has been discussed, solid state ^{59}Co NMR studies of Co(III) ammine coordinated complexes have been limited. Further verification of the relationship between oxo coordination and the chemical shift which has been observed can be found from the few examples in literature. A hexammine complex of the form $[Co(NH_3)_6]Cl_3$ has been reported with four discernible sites with δ_{iso} from 7899(2) ppm to 7848(2) ppm.[113] The study of nitrito and nitro pentamminecobalt chloride discussed previously reported a chemical shift of 8650(50) ppm and 7505(5) ppm respectively. The latter examples correspond to a difference of oxo coordination i.e. whether the nitrogen or oxygen was directly bound.

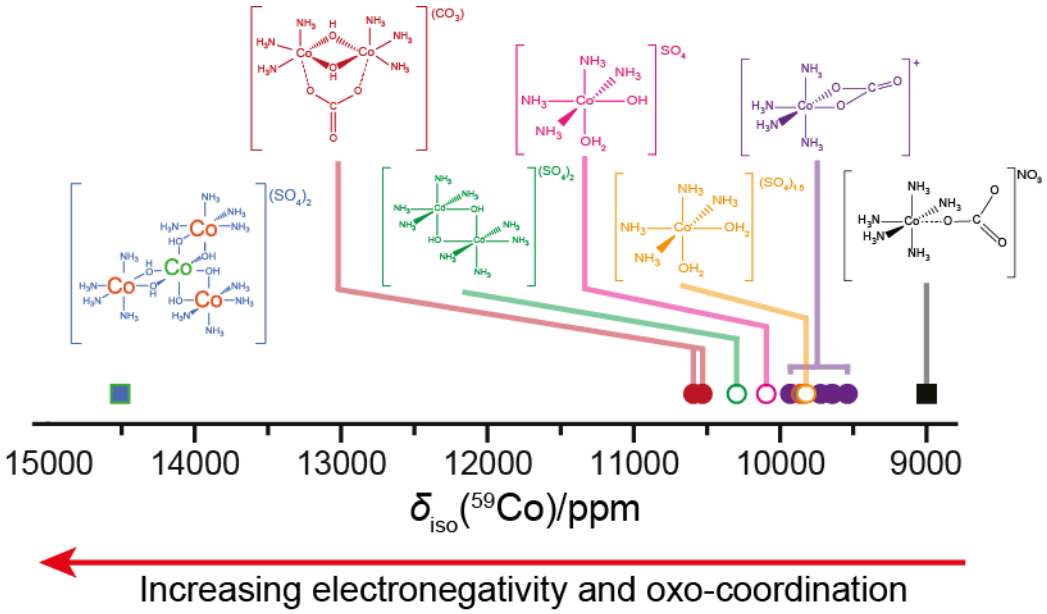

Figure 4-2: Summary of the isotropic chemical shifts for the suite of Co(III) complexes studied via solid state NMR with the inclusion of bonding which was seen to be predominantly ionic in nature, represented by dashed lines.

Solution state NMR chemical shifts have been compared to the solid state shifts previously for some similar ammine complexes, differences typically being ~100 ppm between the states. Interestingly, a solution shift for hexaquacobalt $[Co(OH_2)_6](ClO_4)_3$ has been reported at 15110 ppm, which is distinctly different to the central coordination of Werner's complex, observed at 14518 ppm. Thus, the difference in chemical shift is sufficient to account for the state change, allowing for a confident identification of Werner's complex if observed in the solution studies. Upon the identification of ^{59}Co species, piecing together a coherent scheme for the evolution of the complexes requires an appreciation for ligand exchange reactions.

4.1.2 Equilibria of Bound Carbonates in Cobalt Complexes

From the solid state studies, it was indicated that carbonate ligands were playing a role in the formation and precipitation of Co oxide nanoparticles (this becomes clearer with the data presented later in Section 4.3). The chemistry of carbonato complexes has historically been of great interest, generating a vast number of studies covering diverse experimental conditions, although typically focusing on acid

catalysed reactions.[114] Thus, a review focusing on pH conditions similar to those seen in the HDC synthesis (pH ~7–11) is apt to focus discussion. A detailed review of the broader subject has previously been undertaken by Krishnamurty *et al*.[107] and forms a good basis for the following.

The dominant mechanism for the hydrolysis or decarboxylation of a metal complex occurs via multiple pathways; two mechanisms have been reported to drive the ligand reactions.[107] Firstly, taking a pentammine complex with the carbonate in a monodentate configuration, as was seen previously in the solid-state studies ($[CoNH_3)_5CO_3]NO_3{\cdot}H_2O$), requires the protonation of the carbonate. Thus,

$$Co(NH_3)_5{*}OCO_2H^{2+} \rightarrow Co(NH_3)_5{*}OH^{2+} + CO_2. \qquad \text{(Equation 4-1)}$$

It has been observed that the metal–oxygen bond (denoted by *) is not broken in the reaction.[114] Alternatively, a direct substitution can occur with a hydroxyl:

$$Co(NH_3)_5CO_3^{+} + OH^{-} \rightarrow Co(NH_3)_5OH^{2+} + CO_3^{2-}. \qquad \text{(Equation 4-2)}$$

Furthermore, the carbonate anions undergo exchange reactions within aqueous media such:

$$H_2CO_3 \rightleftharpoons H_2O + CO_2 \qquad \text{(Equation 4-3)}$$

$$HCO_3^{-} \rightleftharpoons OH^{-} + CO_2 \qquad \text{(Equation 4-4)}$$

Thus, carbonates are known to convert to CO_2 and *vice versa*. These reactions also govern the carbonate exchange between the Co(III) complexes and the aqueous media.[107]

For tetrammine complexes containing a bidentate carbonate ligand in the region $7 < pH < 10$, net acid or base hydrolysis is negligible for the initial ligand replacement. Bidentate carbonate ligands require a chelate ring opening process prior to ligand replacement, which readily occurs as a direct reaction with water[115]:

$$Co(NH_3)_4CO_3^{+} + H_2O \rightleftharpoons Co(NH_3)_4(OH)(CO_3H)^{+} \qquad \text{(Equation 4-5)}$$

At this point, acid-base equilibria occur such:

$$Co(NH_3)_4(H_2O)(CO_3H)^{2+} \rightleftharpoons Co(NH_3)_4(OH)(CO_3H)^{+} + H^{+} \quad \text{(Equation 4-6)}$$

$$Co(NH_3)_4(OH)(CO_3H)^{+} \rightleftharpoons Co(NH_3)_4(OH)(CO_3) + H^{+}. \quad \text{(Equation 4-7)}$$

The rate of decarboxylation for $[Co(NH_3)_4(OH)(CO_3H)]^{+}$ and $[Co(NH_3)_4(H_2O)(CO_3H)]^{2+}$, established from Equations 4-6 and 4-7, is very different with the latter being much faster than the prior. Thus, the protonated carbonate of both complexes is liable to decarboxylate in a similar process to Equation 4-1 leaving a hydroxyl ligand and releasing CO_2. However, the decarboxylation is a reversible reaction forming another equilibrium unless CO_2 is removed from the system. Within the HDC catalyst synthesis method the protons released during the reactions shown in Equations 4-6 and 4-7, are expected to readily react with NH_3. This would potentially also limit the reversibility of the reactions.

4.1.3 Binuclear Complexes

The previous observation of the $[(Co(NH_3)_4)(\mu\text{-}OH)_2](SO_4)_2{\cdot}2H_2O$ complex when synthesising Werner's complex, in conjunction with the formation of $[(Co(NH_3)_3)_2(\mu\text{-}OH)_2(\mu\text{-}CO_3)](CO_3){\cdot}5H_2O$ from the HDC synthesis indicates the importance of binuclear complexes.

Several publications have studied the role of hydroxyls and carbonates in Co(III) complexes.[116-118] The work by Koshy *et al*.[116] attempted to synthesise a carbonate bridged complex from a binuclear complex. Although producing a mononuclear compound, several transferable observations were made in the range of $8.26 \leq pH \leq 9.40$. Firstly, carbonate and CO_2 readily react with terminal hydroxyls.[116] However, when hydroxyls are in a bridging position, they become far less reactive.[116] Furthermore, it was concluded that complexes rapidly undergo isomerisation and the ligands involved were no longer adjacent.[119] This was observed to hinder carbonate ligands from forming bridging structures. This isomerisation has also been studied in triammine complexes in halide media.[118] Finally, reaction rate constants indicated hydroxyl bridge cleavage reactions were catalysed in the presence of carbonate, to a point, but were ultimately independent of pH and carbonate concentration.

4.2 Experimental

An A270 MHz BSX 270 Jeol spectrometer located at Johnson Matthey Technology Centre was used to acquire all solution state spectra. The ^{59}Co and ^{13}C measurements were carried out using single pulse experiments with $\pi/3$ pulses of 4 μs and 3 μs respectively and pulse delays of 200 ms (565 transients for ^{59}Co) and 60 s (45 transients for ^{13}C). Referencing was undertaken using the IUPAC references reported in Section 3.2.3.

Preliminary measurements were undertaken by making saturated H_2O solutions from solid samples of $[Co(NH_3)_5CO_3]NO_3 \cdot H_2O$, $[Co(NH_3)_4CO_3]Br$, $[Co(NH_3)_4CO_3](SO_4)_{0.5} \cdot 1.5H_2O$ and $[(Co(NH_3)_3)_2(\mu\text{-}OH)_2(\mu\text{-}CO_3)](CO_3) \cdot 5H_2O$ these were synthesised and characterised previously in Section 3.2. The same method was also used for the reagents of ammonium carbamate ($NH_4[H_2NCO_2]$), ammonium hydrogen carbonate ($NH_4[HCO_3]$) and ammonium carbonate ($(NH_4)_2[CO_3]$) which were acquired from Alfa Aesar. The saturated solutions were then made into a ratio of 4:1 with D_2O to enable the use of the lock function on the spectrometer.

Due to the large ^{59}Co chemical shift range acquisitions were undertaken at offsets of 8300 ppm, 10150 ppm, 11900 ppm and 13650 ppm, however, during time resolved measurements only the latter three were used. Spectra have then been processed using the Delta program native to the spectrometer and presented continuously across the observed chemical shift range, omitting resonances which were folded in at the edges due to the lack of a digital filter.

The syntheses of $Co_3O_4/\gamma\text{-}Al_2O_3$ via the HDC catalyst method was carried out as described in Section 3.2.1 using both precursors. The treatment of the cobalt solutions converges at the point where solid samples were previously isolated. At this point $\gamma\text{-}Al_2O_3$ support was added to the liquor and heating was applied to bring the slurries to a boil. Upon application of heat the syntheses were sampled every ~20 minutes and corresponding temperature, pH and cobalt concentration readings were undertaken. The cobalt concentration was analysed using inductively coupled plasma

mass spectroscopy internally at Johnson Matthey. Samples were taken immediately to the NMR spectrometer where a 4:1 ratio of slurry to D_2O was made and measurements were obtained. The method was repeated until the NMR was unable to detect an appreciable signal in the allotted time (5 minutes per ^{59}Co spectrum, ^{13}C ran over night at 45 minutes per sample). Upon completion of the nanoparticle synthesis a black solid was observed and the solution had decolourised. This was cooled and a Buchner funnel used to collect the catalyst, which was washed with water and dried at 100 ˚C over night.

4.3 Results and Discussion

4.3.1 Preliminary Measurements

Three carbonate compounds were dissolved into saturated solutions and are shown in Figure 4-3. From literature, it is apparent that across the series there are only two species present, with a series of exchange reactions occurring.[120] The ammonium carbamate and ammonium carbonate solutions exhibit a carbamate peak at 165.51(1) ppm and 165.42(1) ppm, respectively (these are comparable to values reported before

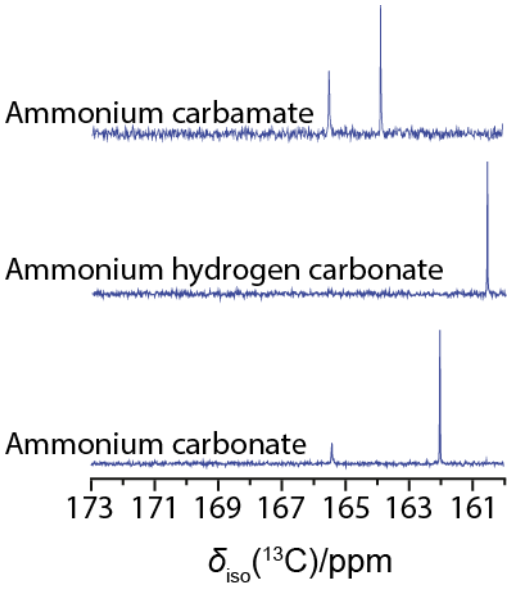

Figure 4-3: ^{13}C solution state NMR of ammonia and ammonium compounds dissolved in H_2O.

166.20-165.56 ppm).[120] The second species at low frequency, is a carbonate/ bicarbonate resonance which is pH dependant due to fast proton exchange. From Figure 4-3, this exchange resonance varies between 160.60(1)–163.85(1) ppm.[120]

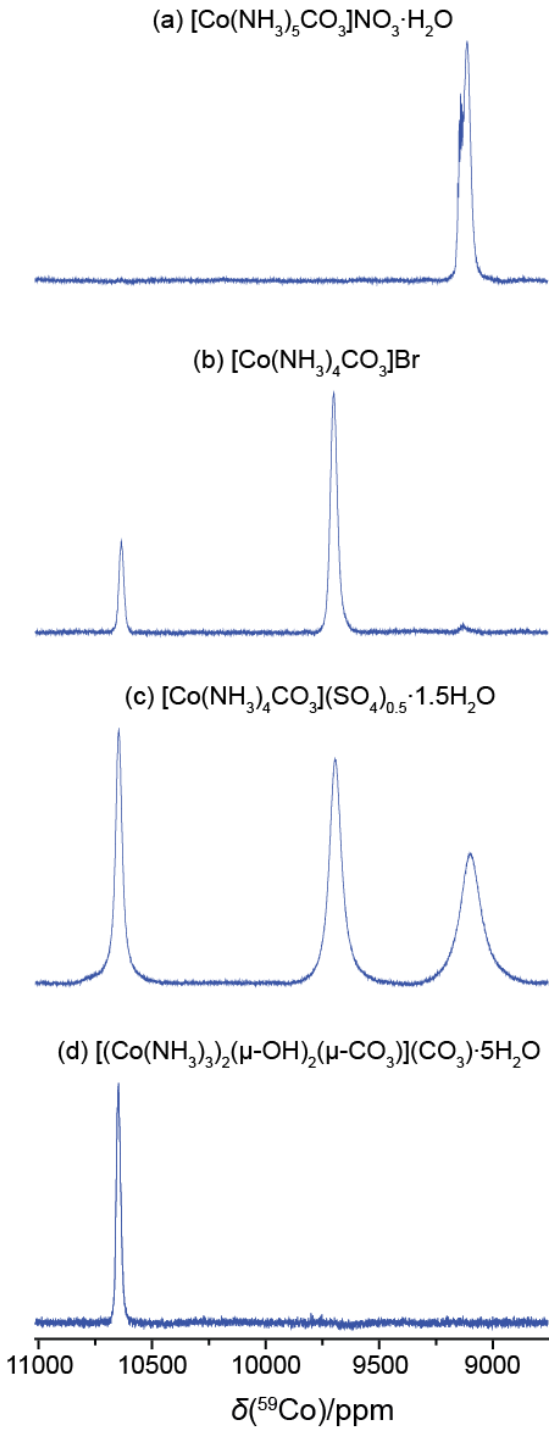

Figure 4-4: ^{59}Co solution state NMR of complexes measured in the solid state after making saturated H_2O solutions. The labels correspond to the solid complex used, such: (a) $[Co(NH_3)_5CO_3]NO_3{\cdot}H_2O$, (b) $[Co(NH_3)_4CO_3]Br$, (c) $[Co(NH_3)_4CO_3](SO_4)_{0.5}{\cdot}1.5H_2O$ and (d) $[(Co(NH_3)_3)_2(\mu\text{-}OH)_2(\mu\text{-}CO_3)](CO_3){\cdot}5H_2O$.

To corroborate the solid state chemical shifts discussed previously, several of the Co(III) complexes studied were made into saturated solutions with H_2O and D_2O as described. The pentammine complex, now of the form $[Co(NH_3)_5CO_3]^+$, is shown in Figure 4-4(a) . The chemical shift was observed at ~9100 ppm in solution, which is slightly more deshielded than in the solid. However, there are two environments present, one to the carbonato complex and the other assigned to $[Co(NH_3)_5OH]^{2+}$ due to direct ligand substitution (Equation 4-2). The J-coupling observed was thought to be due to an increase in resolution, which arises from an increase in molecular motion from the smaller complex.

The bromide and sulphate carbonatotetramminecobalt(III) complexes were also dissolved, as seen in Figure 4-4(b) and (c). Both the bromide and sulphate complexes were observed to convert into $[Co(NH_3)_5CO_3]^+$ and $[(Co(NH_3)_3)_2(\mu\text{-}OH)_2(\mu\text{-}CO_3)]^{2+}$, confirming the reactivity with water which caused a ring opening process, as shown in Equation 4-5. Interestingly, since the complexes were dissolved in H_2O formation of the higher and lower oxygen coordinated complexes indicates an equilibrium occurs due to the availability of NH_3. This limits the amount of higher ammine coordinated complexes, depending on the amount of triammine produced.

The dimeric triammine complex, $[(Co(NH_3)_3)_2(\mu\text{-}OH)_2(\mu\text{-}CO_3)](CO_3)\cdot 5H_2O$, would also require a ring opening reaction to break one of the Co–O bonds, before ligand exchange. It is apparent that it is not the same mechanism as observed in the Figure 4-4(b) and (c) for the $[Co(NH_3)_4CO_3]^+$ complexes, as shown by the single ^{59}Co environment in Figure 4-4(d) at ~10650 ppm. Since the C–O bonds were essentially ionic in nature, seen from the ^{13}C CPMAS solid state NMR data. It is proposed that the removal of the bridging carbonate would be similar to the monodentate of the pentammine complex, due to the comparable ^{13}C CPMAS measurements in the solid state. Thus, reactivity of the ionic carbonate ligands may be due to the exchange reactions of Equations 4-3 and 4-4.

4.3.2 Time Resolved Measurements

The first successful attempts to acquire solution state NMR data in a time resolved fashion, as described in Section 4.2, are shown in Figure 4-5. Initial spectra of the solutions prior to the addition of γ-Al_2O_3 and heating is shown below the 2D plots in Figure 4-5. This state was equivalent to that when the solid precipitant, shown previously to be $[(Co(NH_3)_3)_2(\mu\text{-}OH)_2(\mu\text{-}CO_3)](CO_3)\cdot 5H_2O$ (dimeric triammine), was extracted.

An equilibrium containing a multitude of Co(III) complexes exists. However, the two predominant resonances common to both initial spectra of Figure 4-5(a) and (b) are at ~9100 ppm and ~9700 ppm. These are assigned to $[Co(NH_3)_5CO_3]^+$ (pentammine) and $[Co(NH_3)_4CO_3]^+$ (tetrammine) chemical shifts as found in the solid state and were corroborated by the preliminary solution NMR measurements.

The HDC catalyst synthesis utilising the metal precursor (Figure 4-5(a)), shows two other significant resonances, one at ~8200 ppm and one at ~10650 ppm. The complex at 10650 ppm is assigned to $[(Co(NH_3)_3)_2(\mu\text{-}OH)_2(\mu\text{-}CO_3)]^{2+}$, also shown in the preliminary measurements. The low frequency chemical shift is indicative of a hexammine complex[113], as discussed previously, and is inert in base conditions (remaining after synthesis completion). From the solid state NMR research, the small resonance at ~10300 ppm can be assigned to a complex similar to $[Co(NH_3)_4(\mu\text{-}OH)_2]^{4+}$.

From Figure 4-5(a), an increasing predominance of the complex $[(Co(NH_3)_3)_2(\mu\text{-}OH)_2(\mu\text{-}CO_3)]^{2+}$ was seen in the 2D plot. This increase was clearer in the speciation scatter graph. The increasing predominance of $[(Co(NH_3)_3)_2(\mu\text{-}OH)_2(\mu\text{-}CO_3)]^{2+}$ coincides with the dissolving of a significant amount of the solid state complex $[(Co(NH_3)_3)_2(\mu\text{-}OH)_2(\mu\text{-}CO_3)](CO_3)\cdot 5H_2O$, which previously crystallised out. The uptake was seen to continue until the 40 minutes point where the resonance begins to quickly reduce, indicating the complex readily reacts in the slurry.

The pentammine resonance at ~9100 ppm continuously declines throughout the synthesis. However, the resonance appeared to have two components which were

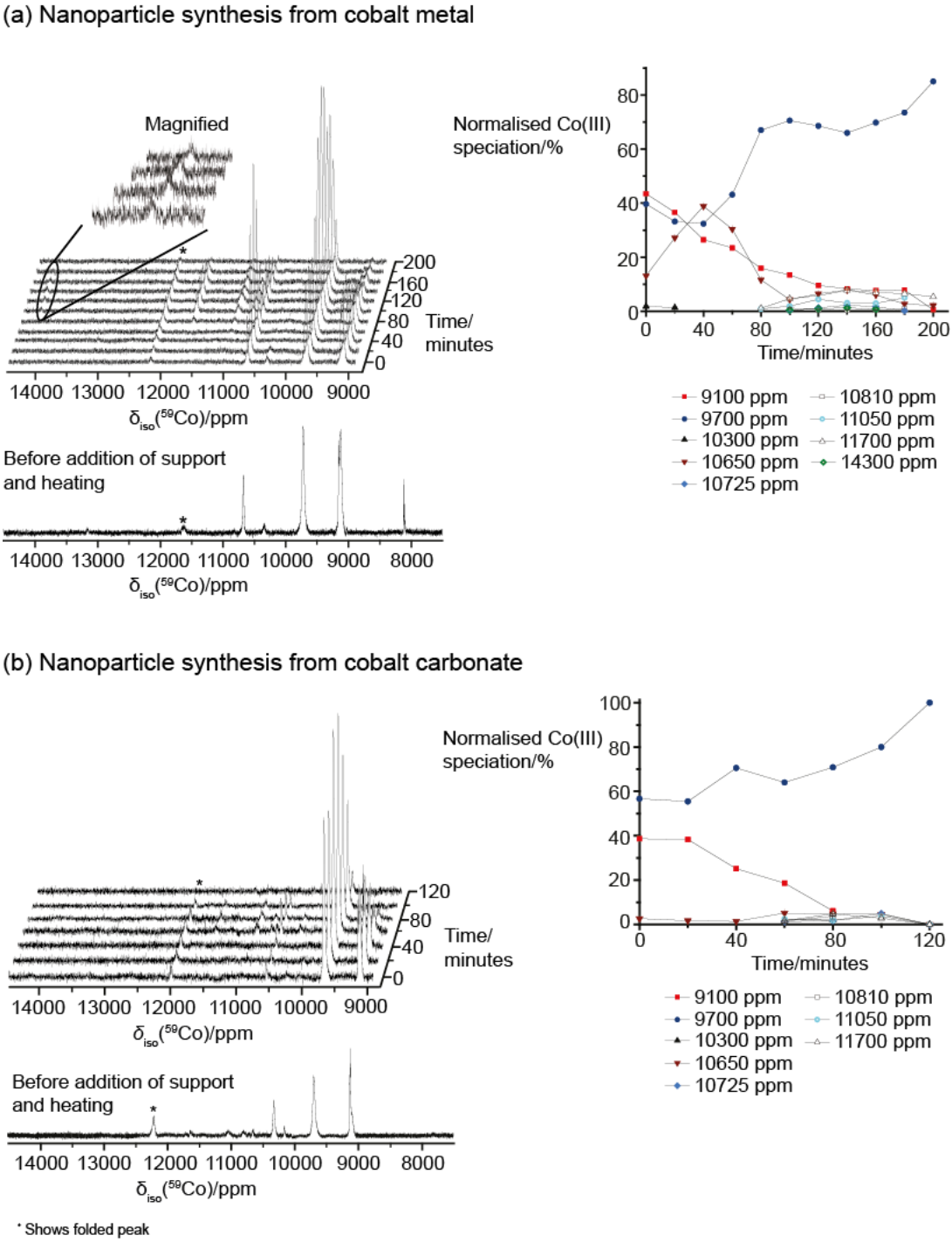

Figure 4-5: Summaries of the spectra acquired with time resolution of the two synthesis methods. Integrated areas of the resolved resonances were normalised and plotted against time demonstrating relevance of different complexes (assigned by chemical shift) through the reaction. The method using cobalt metal precursor is shown in (a) and (b) shows the method from cobalt carbonate.

observed after 80 minutes. The difference is thought to coincide with the type of oxo coordination, beginning with a monodentate carbonate ligand which is removed and replaced by a hydroxyl, as seen in the preliminary measurements. This reaction would potentially be an equilibrium based on carbonate content within the slurry. It is the tetrammine complex, $[Co(NH_3)_4CO_3]^+$ which persists throughout the reaction. This is counter to what was seen in the aqueous media of the preliminary results. Thus, the dominant mechanism of decarboxylation has changed from those seen in the preliminary measurements. As the experiment reached the sensitivity limit of the NMR experiment, the tetrammine was the only resonance still discernible and is thought to be the predominant route to higher oxo coordination.

Furthermore, from the magnified region shown in Figure 4-5(a), a resonance at ~14300 ppm was observed coinciding with a fully oxo coordinated cobalt. This was assigned to Werner's complex from the chemical shift (solid: 14518 ppm) and corroborated by the significant tetrammine resonance. However, the outer tetrammine (with OH bridging ligands) of Werner's complex were not resolvable from the carbonatotetrammine resonance. Thus, the initial hypothesis appears to be correct and Co oxide nanoparticles do precipitate from Werner's complex.

At a comparable time to the precipitation, four additional triammine and diammine complexes can be seen between 10725 ppm and 11700 ppm, indicating that the increase in oxo coordination of the cobalt occurs in a step wise manor. The two or three new triammine complexes seen to appear after 80 minutes would be consistent with bridge cleavage, and the formation of intermediate complexes. The chemical shifts suggest very similar complexes in the region, which may indicate isomerisation occurring. These processes lead to a larger diversity of Co(III) complexes than at other degrees of oxo coordination, due to isomerisation of exposing hydroxyl ligands after bridge cleavage, which are known to be very reactive.[116]

Although the catalysts produced from the two HDC catalyst syntheses are comparable from the point of view of Johnson Matthey, the solutions studied show differences in speciation and their relative amounts. From Figure 4-5(b) it is apparent

that both synthesis routes are similar, although the carbonate precursor method yields a greater diversity of species which are lost in the noise upon shorter acquisition. Significantly less $[(Co(NH_3)_3)_2(\mu\text{-}OH)_2(\mu\text{-}CO_3)]^{2+}$ was present in the reaction and as a solid (the latter being dependant on the time the liquor was left, prior to adding the support and heating). This complex does still play a role however, maintaining a presence in the reaction for a significant proportion of the synthesis. The tetrammine and pentammine complexes behave similar to the metal synthesis.

A comparison of the chemical shifts shows the ^{59}Co species involved in the carbonate synthesis are comparable to that of the metal precursor method. This includes the multitude of triammine species which supports the comparative nature between both routes. Thus, because $[(Co(NH_3)_3)_2(\mu\text{-}OH)_2(\mu\text{-}CO_3)]^{2+}$ is forming in both reactions with differing prominence, it is probably a buffer depending on carbonate content and was not part of the direct route to Co oxide nanoparticles. The reduced signal to noise was due to a reduced amount of cobalt content in the reaction, thus, the resonance of Werner's complex was lost in the baseline. It was assumed all ^{59}Co relaxed rapidly, however this could not be confirmed for the oxo coordinated core of Werner's complex due to the insolubility of the solid.

As demonstrated from the reactions shown in Figure 4-5(a) and (b), the time it takes to complete the synthesis can vary drastically depending on the thermal transfer. Using pH as a point of reference allows for a comparison of repeated syntheses, even when reaction times varied greatly, as shown in Figure 4-6. However, as seen when monitoring the cobalt content of the solutions, the pH tended to decrease with time but this was not stringent and reverses in the trend were also observed.

When monitoring the Co content through the reactions, the preference of the metal method to crystallising out $[(Co(NH_3)_3)_2(\mu\text{-}OH)_2(\mu\text{-}CO_3)]^{2+}$ was clear, as observed in Figure 4-6. Following the metal preparation via the red squares starting at high pH, direct comparison to Figure 4-5(a) can be made. The second point was where the support was added diluting the Co content and heating began. This also corresponds

to the first spectrum of the 2D plot (which was not the case for any other data shown in Figure 4-6 where the first point coincides with the first spectrum).

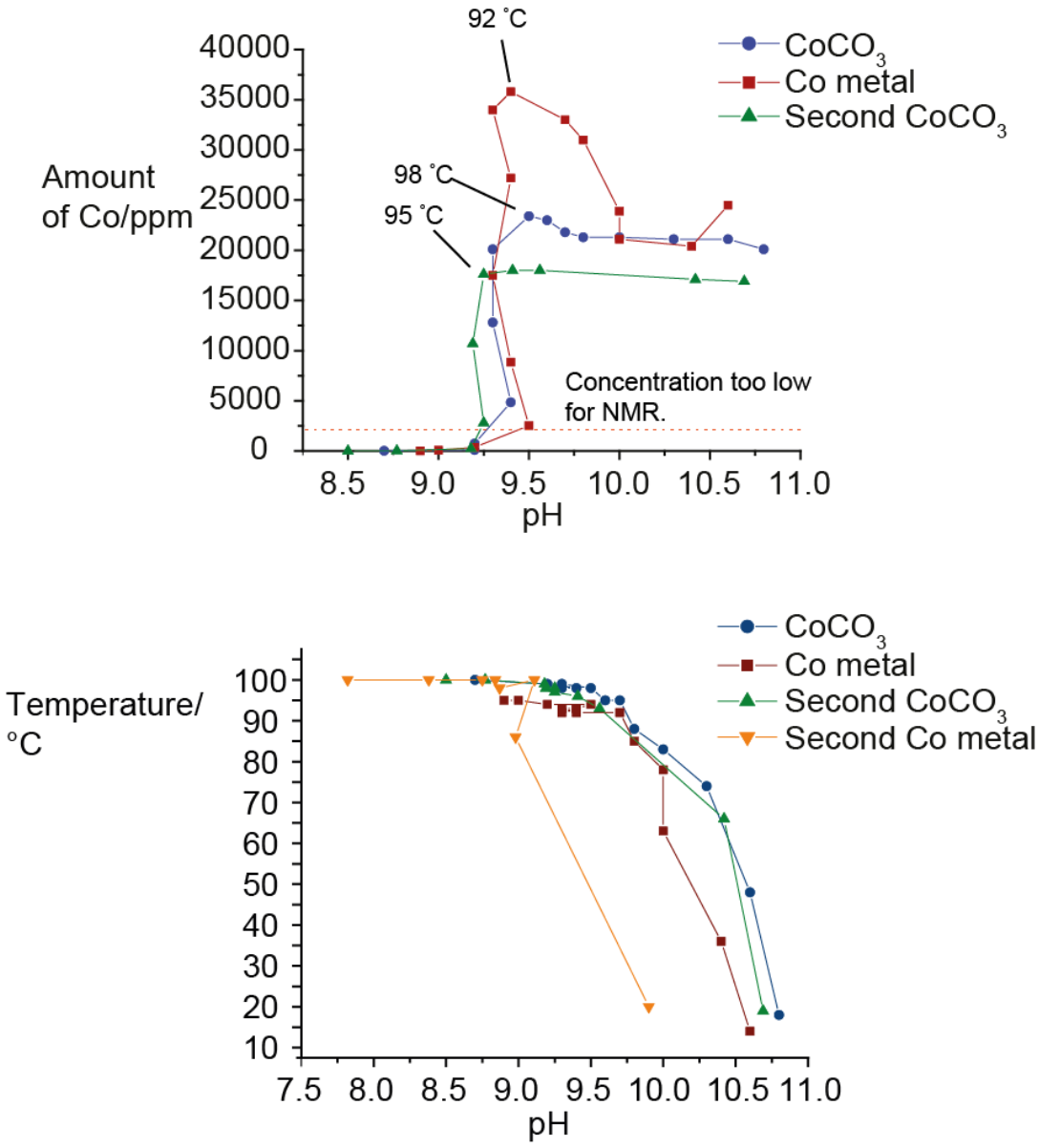

Figure 4-6: Monitoring amount of Co and temperature of liquors with respect to pH for all attempts to obtain time resolution of Co oxide nanoparticle precipitation (one synthesis from cobalt metal did not have ICP analysis of Co content). The concentration and temperature data points correspond to time slices, where time moves from high pH to low pH in intervals of 20 minutes per data point starting at zero minutes. The Co metal data has two zero points, due to measurements before and after support addition.

As heating began, the pH was observed to decrease in Figure 4-6 as the pentammine, tetrammine and dimeric triammine complexes are driven to new equilibria. A conversion of pentammine to tetrammine would be required to maintain the significant resonance at ~9700 ppm seen in Figure 4-5(a). It is unlikely $[(Co(NH_3)_3)_2(\mu\text{-}OH)_2(\mu\text{-}CO_3)]^{2+}$ converts back to the tetrammine complex due to the three bridges, especially the two strongly bound hydroxyl bridges seen in the solid-state measurements which are known to be difficult to cleave. [116]

Through the first 100 minutes of the synthesis, the NMR showed an increasing predominance of the dimeric triammine complex until 40 minutes, where it quickly began to decline. However, the ICP-MS analysis showed cobalt content continued to increase from 40 to 100 minutes. Thus, at 40 minutes although the dimeric triammine was readily dissolved, it decomposed and reacted rapidly. This would explain the differences between the ICP-MS and solution state observations. During this period pH dropped by one as the slurry reached a temperature of 92 ˚C. The decreasing pH would potentially indicate the release of CO_2 as the complex reacted. The first signs of resultant triammine complexes and isomers were observed at 60 minutes. This observation was clearer at 80 minutes in solution state NMR as the products become more prominent (see the speciation graph Figure 4-5(a)). The low sensitivity of the NMR experiment explains the Absence of these complexes and isomers at 40 minutes.

For the carbonate precursor syntheses, the equilibrium was focused predominantly on the pentammine and tetrammine, due to much less prominent presence of the dimeric triammine. From Figure 4-6, two runs were undertaken. The first, represented by blue circles, was the initial run where the methodology was tested. However, the NMR data was incomplete (the total NMR resolvable run time was ~200 minutes). A quicker, second run was repeated and presented in Figure 4-5(b) (green triangles Figure 4-6), which reached a comparable region to the metal in 80 minutes. During this period, cobalt content remained constant indicating very little $[(Co(NH_3)_3)_2(\mu\text{-}OH)_2(\mu\text{-}CO_3)](CO_3)\cdot 5H_2O$ precipitant. However, following the speciation during this period (Figure 4-5(b)) shows the reduced presence of

pentammine and formation of $[(Co(NH_3)_3)_2(\mu\text{-}OH)_2(\mu\text{-}CO_3)]^{2+}$. During this same period, the tetrammine resonance continued to gain increased dominance. Thus, during the initial heating period pentammine likely converts to tetrammine.

Due to the formation of $[(Co(NH_3)_3)_2(\mu\text{-}OH)_2(\mu\text{-}CO_3)]^{2+}$ at later stages in the carbonate synthesis, it is concluded that formation occurs after the tetrammine begins to react and as the solutions approach boiling point. At this point, pH fluctuates only a small amount and cobalt content begins to decrease correlating with nanoparticle precipitation. Time resolved studies revealed that the resonances corresponding to the formation of additional triammine and diammine species were observed, similar to the metal synthesis at 10725 ppm, 10810 ppm, 11050 ppm and 11700 ppm. The formation of Werner's complex was also seen in this period previously. It is likely the complex quickly precipitates out of the solution. This in conjunction with a lower Co content limits the ability of NMR to observe it during the carbonate syntheses.

The evolution of the carbonate anion through the synthesis appears to be fundamental to Co(III) species equilibria, prior to the boiling of the slurry. During heating, three unique structures are seen: monodentate, bidentate and bridging. Thus, attempts to measure the ^{13}C in a time resolved manor were also undertaken.

A second HDC catalysts synthesis was carried out using the metal precursor and is shown in Figure 4-7. The rate of heating was much quicker than the first run, reaching levels too low for the NMR method in only 100 minutes (previously ~200 minutes). The temperature and pH dependence of this second run can be seen as yellow inverted triangles in Figure 4-6. Although the reaction was much faster, the ^{59}Co NMR spectra (which are summarised in Figure 4-7), follow the same evolution as seen before, but include the corresponding solution ^{13}C NMR measurements.

Five ^{13}C NMR resonances were observed, two at 164.34(1) ppm and 165.73(1) ppm correspond to the dynamic equilibrium between carbonate (referred to as free carbonate from this point on) and bicarbonate and ammonium carbamate (NH_2CO_2). These were seen in the preliminary measurements, presented in Section 4.3.1. The final three ^{13}C NMR resonances are the Co(III) complexes. These have been assigned

such that the bidentate carbonate of $[Co(NH_3)_4CO_3]^+$ had a chemical shift in the solid state of ~166.5 ppm, which was seen in solution at 167.51(1) ppm. The tetrammine was the most obvious due to its long life in the synthesis. Secondly, $[(Co(NH_3)_3)_2(\mu\text{-}OH)_2(\mu\text{-}CO_3)]^{2+}$ was seen in solid state at 167.00(4) ppm versus 168.47(1) ppm in solution. Although the ^{59}Co NMR resonance for $[(Co(NH_3)_3)_2(\mu\text{-}OH)_2(\mu\text{-}CO_3)]^{2+}$ was initially on the same order of magnitude as the other complexes the ratio of cobalt:carbon was 2:1 rather than 1:1. Thus, a smaller ^{13}C NMR signal would be expected for equal amounts of ^{59}Co intensity. The monodentate carbonate of $[Co(NH_3)_5CO_3]^+$ was observed at 167.68(4) ppm in solid state coinciding with 168.87(1) ppm in solution state. The resonance was observed to quickly diminishes as carbonate either exchanged with hydroxyls, or converted to a bidentate configuration. All solution ^{13}C NMR resonances were more deshielded in solution.

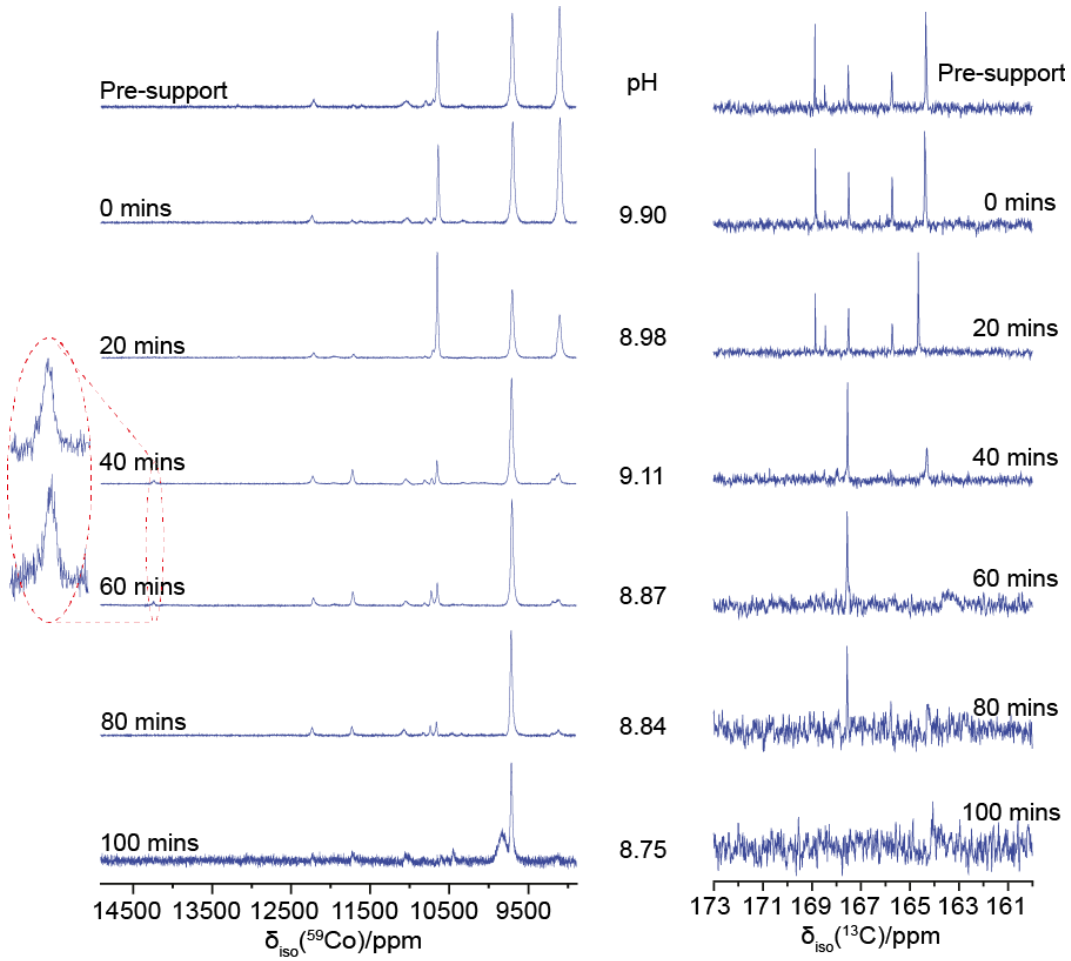

Figure 4-7: Time resolved Co_3O_4/Al_2O_3 synthesis using cobalt metal precursor, monitoring the solution state ^{59}Co and ^{13}C.

The initial heating period between 0 to 20 minutes of Figure 4-7 indicates the uptake of the dimeric triammine as expected. Decomposition of pentammine and triammine was also observed to release CO_2 into the system. This is shown in the ^{13}C NMR data due to the significant increase of the resonance at 164.34(1) ppm, thus driving the carbonate exchange, as described by Equations 4-3 and 4-4. As the reaction was seen to approach 40 minutes (which was 100 ˚C), ammonia carbonate was observed to collect in the condenser above the reaction. It was assumed that at this point all carbonate had left the reaction. However, as can be seen in Figure 4-7, the tetrammine species maintains the bidentate carbonate ligand and the free carbonate is still present. The free carbonate is most likely due to have been released from the continued evolution of the remaining $[Co(NH_3)_4CO_3]^+$. Although Werner's complex was seen at 40 and 60 minutes, the quantity made at 80 and 100 minutes was insufficient for the NMR sensitivity. However, the precursor triammine and diamine species are still present indicating rapid precipitation of Werner's complex.

4.3.3 Proposed Synthesis Route

Consolidating the observations from the time resolved synthesis allows for the proposition and discussion of an evolution scheme, prior to nanoparticle precipitation. A full explicit reaction mechanism with all possible equilibria is not possible, due to the convoluted nature of the reactions. This was seen in Section 4.3.2 in conjunction with experimental limitation which fail to capture short lived and low population species. However, the time resolved measurements provide sufficient insight to evaluate the roles of the carbonate species of pentammine, tetrammine and triammine complexes. Furthermore, an informed analysis of some of the intermediates is possible.

Research on monodentate and bidentate carbonate equilibria in chromium complexes by Erikson *et al.*[121] has been used to expand the carbonate equilibria, which have been observed in the solution studies, carried out in Section 4.3.2. Thus, the expanded CO_3 exchange reaction has been included in Figure 4-8. The newly introduced H_2CO_3 would be part of the equilibrium resonance at 160 ppm to 164 ppm.[122]

Prior to the main synthesis, the triammine complex was observed to readily crystallised out of both synthesis methods. Although it was seen to be produced as larger, more abundant crystals from the metal precursor method. Thus, Figure 4-8 shows the proposed synthesis route prior to heating and addition of the support. The preliminary measurements undertaken demonstrated the ease of which the bidentate carbonate reacts in the presence of H_2O, forming the other two complexes. In the

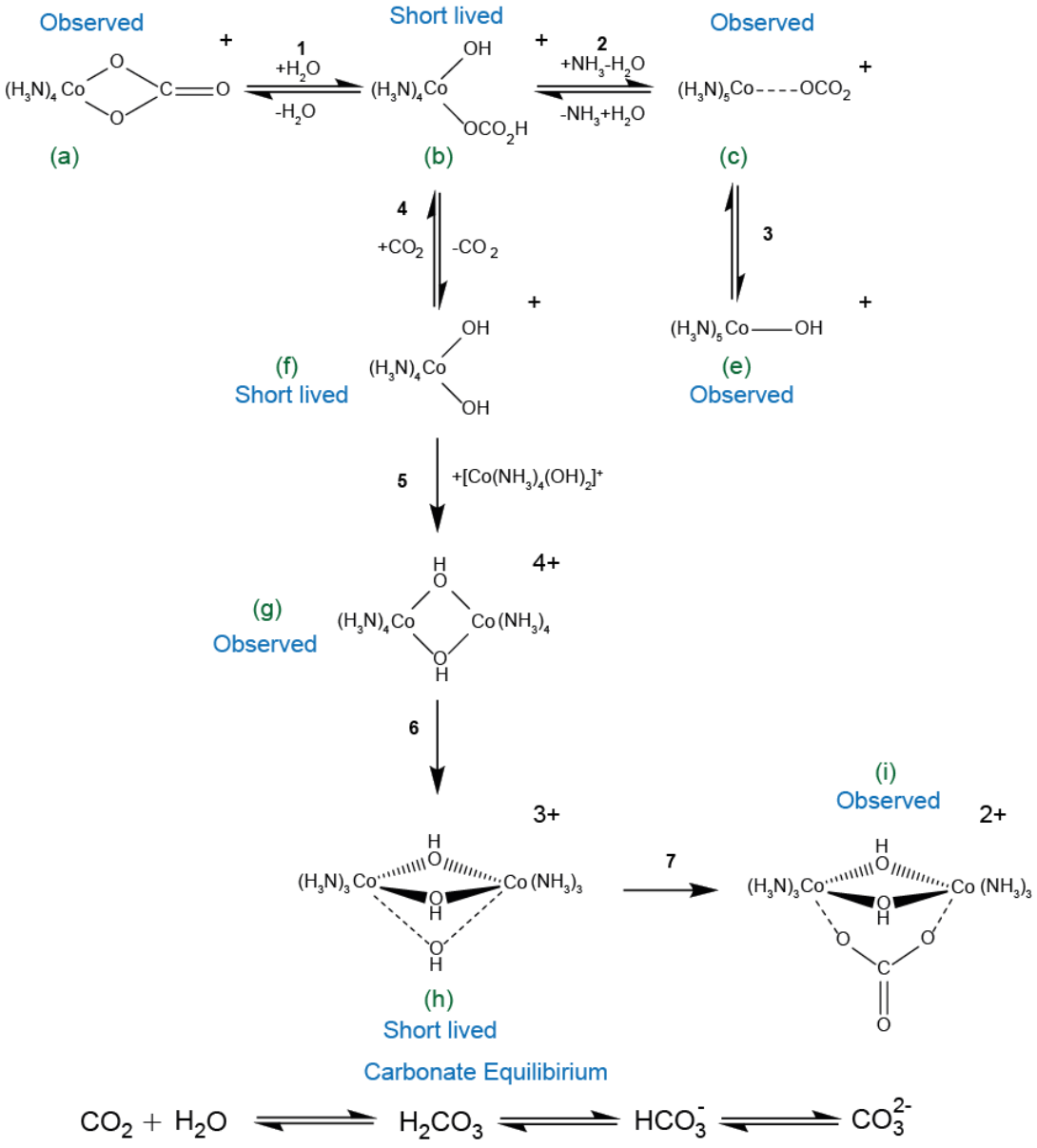

Figure 4-8: Proposed initial reaction scheme prior to the addition of support and the addition of heat. Some reversible changes ignored due likely being irreversible until heating is applied. Dashed lines show ionic bonding identified in the ^{13}C solid state CPMAS NMR measurements.

HDC catalyst synthesis this was not seen to be the case and it was $[Co(NH_3)_5CO_3]^+$ and $[(Co(NH_3)_3)_2(\mu\text{-}OH)_2(\mu\text{-}CO_3)]^{2+}$ which readily reacted and decomposed. Thus, it is proposed that the pentammine, $[Co(NH_3)_5CO_3]^+$, and tetrammine, $[Co(NH_3)_4CO_3]^+$, form first (Figure 4-8(a) and (c)). These complexes both have pathways to the formation of $[Co(NH_3)_4(OH)(CO_3H)]^+$ as shown in Figure 4-8(b) , via **1** and **2**.

The complex $[Co(NH_3)_4(OH)(CO_3H)]^+$ is short lived with two very reactive ligands. The exchange of the hydroxyl with an ammine at point **2** in Figure 4-8, forms the lower oxo coordinated pentammine. This may be driven by an internal H-bond between the protonated carbonate and the hydroxyl. The same mechanism may have been observed in the preliminary tetrammine measurements. An equilibrium between the type of oxo coordination is shown at **3** for the pentammine complexes (Figure 4-8(c) and (e)). At the early stages of the synthesis, there is an abundance of carbonate anions in the system and the equilibrium at **3** tends towards the carbonate ligand. It is unclear whether the carbonate ligand at this stage would be protonated, and would be dependent on the exchange mechanism, as discussed in Section 4.1.2.

It is probable that the tetrammine species does evolve in a comparable way to the synthesis used to make Werner's complex. This would seem logical following a similar method to what was shown in Equation 4-1, where the metal–oxygen bond remains intact, and CO_2 is released producing the complex $[Co(NH_3)_4(OH)_2]^+$ (Figure 4-8(f)). Association would occur to form a dimeric structure shown via **5** resulting in Figure 4-8(g). From the solid state studies, the hydroxyl bridges are highly shielded and are known to be unreactive.[116] It is unlikely at this stage that the complex would revert to a monomer easily.

The replacement of an ammine group was seen to occur in aqueous media in the preliminary measurements. However, only a single triammine resonance for $[(Co(NH_3)_3)_2(\mu\text{-}OH)_2(\mu\text{-}CO_3)]^{2+}$, was observed. It is thought $[(Co(NH_3)_3)_2(\mu\text{-}OH)_3]^{3+}$, (Figure 4-8(h)), was short lived or unstable in the experimental conditions due to no direct observation. However, the triple OH bridging structure would

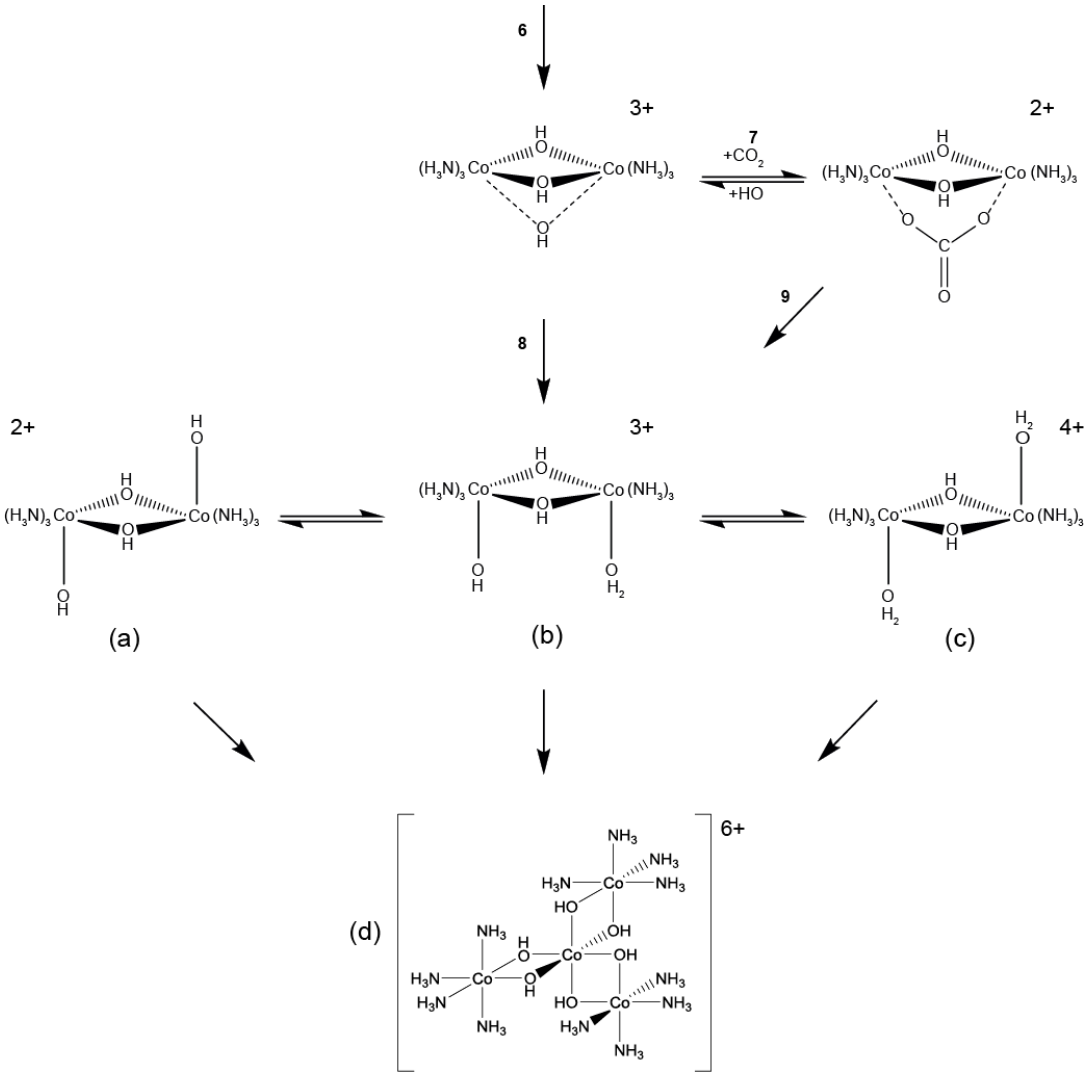

Figure 4-9: Complex evolution continues with the application of heat. The evolutions shown are proposed complexes that likely make up some of the triammine species observed in the NMR measurements.

potentially enable the carbonate bridge to form; isomerisation of OH ligands is known to limit this bridging formation.[116,119] The scheme presented in Figure 4-8 shows the evolution at **7** irreversible. However, as was seen in Figure 4-5 upon heating and into the later stages of the reactions it is likely **7** becomes reversible, leading to several complexes and isomers, as was discussed in Section 4.1.3.

Upon heating of the slurry, it was not possible to state exactly the form of the triammine or diammine complexes which were observed at 10725 ppm, 10810 ppm, 11050 ppm and 11700 ppm. It can be hypothesised that as heating begins the

mechanism at **7** becomes reversible or a second pathway forms, as shown in Figure 4-9. It is likely that upon heating, evolution of the complexes occurs and is represented **8** and/or **9** in Figure 4-9. Thus, some of the resonances identified between 10750-11700 ppm could be similar to those shown in Figure 4-9 (a), (b) or (c), forming from decarboxylation and isomerisation.

The dimeric triammine species shown in Figure 4-9(a), (b) and (c) would quickly become points for continued evolution, with several isomers and interconversions. Eventually, a trimeric complex would potentially form with one of the reactive ligands becoming a bridge. Removal of NH_3 as NH_4 would occur until Werner's complex formed, which was seen in the NMR. This process is subjective due to the rapid evolution of the reaction but is indicated in Figure 4-9(d). The growth of the oxo coordinated core of Werner's complex is thought to continue until the precipitation to Co_3O_4 occurs. From observations of the time resolved solution state ^{59}Co NMR, the precipitation is a fast process.

4.4 Conclusions

Solid state NMR measurements allowed for the assignment of both ^{59}Co species and ^{13}C species in solution state. The data also identified the bonding nature of carbonate ligands in the different configurations: monodentate, bidentate and bridging. Identifying the similarities of the monodentate and bridging configuration has been shown to be important, explaining why the bridging and bidentate configurations do not react via a similar mechanism.

This difference was first seen in the preliminary solution state measurements, which compared solution and solid state chemical shifts. It was observed that the tetrammine complexes readily decomposed into pentammine and triammine species. However, this was not a reversible process with solutions of pentammine and dimeric triammine remaining relatively pure. Although the pentammine complex was seen to exchange carbonate ligands with OH. During the time resolved syntheses, NMR measurements and monitoring of cobalt content alluded to the rapid decomposition

of both pentammine and triammine. The ionically bonded carbonate ligands most likely shared a similar decarboxylation mechanism. However, the lack of study of bridging carbonates in the pH range has meant further details cannot be provided.

During the precipitation of nanoparticles several triammine and diamine species were observed. It was concluded that several isomerization reactions occurred prior to the association of Co(III) complexes. As this occurs, complexes are short lived and it is not possible to complete a full synthesis pathway. The study has alluded to the key species and the long lived nature of the carbonate anion within the HDC synthesis.

The NMR study of both synthesis routes verified a common route to the precipitation of cobalt oxide nanoparticles. However, differences in relative amounts of key Co(III) complexes allowed for identification of the carbonatotetrammine complex as an initial precursor. Coupled with the observation of Werner's complex the original hypothesis has been verified. It has also been possible to infer equilibria reactions and mechanisms, including the observation $[(Co(NH_3)_3)_2(\mu\text{-}OH)_2(\mu\text{-}CO_3)]^{2+}$ does not necessarily play a significant role as first thought. The presence of the complex in both synthesis routes emphasises its role as an intermediate. The insight will hopefully enable future work into reducing the formation of $[(Co(NH_3)_3)_2(\mu\text{-}OH)_2(\mu\text{-}CO_3)](CO_3)\cdot 5H_2O$ in the cobalt metal synthesis, which is known to cause problems in production of the Co oxide nanoparticle catalysts, thus, potentially enabling continuous production of HDC catalysts for FT technologies. Thus, NMR has been shown to extract details from a very complex and dynamic system. Insights into the production of a commercial product have been obtained and will aid future development. This study also provides a methodology to study other systems which evolve through metal complexes.

Chapter 5 Catalyst support Interactions of Pt and Ni Catalyst Precursors

5.1 Background

The importance of heterogeneous catalysts for hydrogenation reactions is demonstrated by their utilisation across large commercial sectors, these including food, petrochemical and pharmaceutical.[50-52] Utilising metal oxide supports catalytic active materials are dispersed across a large surface area, thus maximising their reaction efficiencies. In addition to the physical dispersion oxide supports also interact with the catalytic materials beneficially[58] or detrimentally[57]. Utilising multi nuclear solid-state NMR, studies of both the catalyst precursors and the oxide support aims to alluded to the interactions between the two.

As discussed previously oxide supports play a significant role in the synthesis of catalytic materials. The mounting of catalytic metal species via nitrate solutions is a straight forward method to manufacturing a range of catalysts.[123,124] Nickel oxide and platinum oxide catalysts were chosen, the latter providing an NMR sensitive nucleus which has proven insightful in similar applications.[12] Furthermore, solid state NMR of PtO_2 has not been formally reported previously to the authors knowledge.

Despite the moderate NMR sensitivity of ^{195}Pt, which has a 33.8% natural abundance and a gyromagnetic ratio of 5.83×10^7 rad T^{-1} s^{-1} solid state studies have been limited.[88] This has predominantly been due to significant linewidths due to the CSA and Knight shift interactions.[12] Extensive ^{195}Pt solution NMR analysis has been reported and a catalogue of chemical shift assignments can be used to inform measurements.[125,126] The full ^{195}Pt NMR chemical shift range spans ~13000 ppm,

Pt(0) and Pt(II) oxidation states are observable at chemical shifts of ~0 to -6000 ppm. However, all measurements to be reported here are expected to be Pt(IV) which spans 7500 to -7000 ppm.[125]

Four common oxide supports have been studied these were α and γ-alumina, silica and titania. Both ^{27}Al and ^{29}Si NMR are routine and well characterised nuclei.[64] Firstly, ^{27}Al is, a quadrupolar $I = 5/2$ nuclei, with a gyromagnetic ratio of 6.98×10^7 rad T^{-1} s^{-1} and 100% natural abundance, and ^{29}Si, which is $I = 1/2$ with a gyromagnetic ratio of -5.32×10^7 rad T^{-1} s^{-1} but natural abundance of 4.68%. However, titanium measurements were not obtained.

The two aluminium supports studied were α-alumina and γ-alumina. The former contains an ordered 6-coordinate environment, characterisation via NMR has reported a single resonance at 13.9 ppm.[127] Structural disorder makes the study of γ-alumina more difficult for conventional techniques. The disorder manifests in the quadrupolar interaction as a tailing of the spectra towards lower ppm, the Czjzek model provides a method of extracting the NMR parameters.[128] Initial demonstrations of the model were included γ-alumina which reported shifts of 73.8 ppm (AlO(IV)) and 13.8 ppm (AlO(VI). Thus, the measurements under taken are already very well characterised and aim to monitor any changes within the lineshapes. Studies carried out at faster MAS frequencies and higher magnetic fields have also report γ-alumina to contain an AlO(V) environment at ~23 ppm.[129]

A recent study of hydroxyl speciation on γ-alumina utilising dipolar heteronuclear multiple-quantum correlation (HMQC) NMR experiments.[130] This enabled correlations between hydroxyls remaining after being dehydroxylated at 500 ˚C to be correlated to ^{27}Al resonances. The study focused on bridging and surface species which yielded proton speciation between -0.5 ppm and 4 ppm. Specifically, three bridging hydroxyl species have been identified at -0.2, 1.8 and 3 ppm.[130] Hydroxyls which are bound to one or two Al units have also been identified at 8.2(3) ppm and 2.3(2) ppm in boehmite the significant difference in chemical shift being attributed to clustering (thus, H-bonding to one another) or isolation respectively. However,

changes in these resonances to ~7.2 and 1.2 ppm are thought to occur depending on morphology since these can be interior or surface groups. In addition, physorbed water, would be expected at ~4.5 ppm.[131]

Unlike ^{27}Al which is highly receptive to NMR, ^{29}Si is typically more difficult requiring CPMAS experiments to obtain well resolved spectra. With site assignment from CPMAS, quantification can be carried out via direct single pulse measurements. Thus, allowing for a quantitative analysis of the silica network, the notation and understanding of which has been well documented.[64] The silica network is an arrangement of tetrahedral units Q, where by the number of other units linked is denoted in the subscript between 0 and 4. Thus, a silicon atom bound to four other silicon via oxygen is denoted by Q_4. As the subscript reduces the Si groups would likely be replaced by hydroxyls in the studies carried out in this thesis or nitrates.

This chapter aims to identify interactions between catalyst precursors and oxide supports starting from the impregnation of metal nitrate solutions. However, this is not an extensive study but aims to inform a continued investigation, which would utilise^{195}Pt NMR solid state NMR. Identification of precursor species and their decomposition through calcination could provide insight into how the catalysts binds to the surface. The changes caused by thermal treatments were studied by varying calcination temperatures for selected Pt/SiO_2 and Pt/Al_2O_3 materials. Single pulse MAS ^1H measurements are to be undertaken, however, it is not clear how informative these will be due to the possibility of surface species being hidden by large water or structural resonances. However, identification of speciation provides insight into experimental possibilities. Furthermore, measurements will demonstrate the use of the first Bruker 7 mm static ATMA (Automatic Tuning and Matching) probe for automated VOCS measurements of the ^{195}Pt containing materials.

5.2 Experimental

5.2.1 Synthesis

Platinum nitrate solution provided by Johnson Matthey and nickel nitrate hexahydrate acquired from Alfa Aesar were impregnated onto oxide supports via incipient wetness impregnation technique. The resulting pre-catalysts were then calcined at 100 ˚C and 500 ˚C for 2 hours. From this point if a temperature is not associated with the nitrate material it is assumed to be treated at 100 ˚C. Additionally, selected Pt/SiO_2 and Pt/Al_2O_3 materials were calcined at 200 ˚C, 300 ˚C and 400 ˚C.

Two γ-alumina materials were obtained from Sasol, SCFa-140 and HP14-150, SCFa-140 was used as received and also calcined at 1150 ˚C for four hours to produce α-alumina. The γ-alumina HP14-150 was only used for supporting the ^{15}N labelled $Ni(NO_3)_2$. Both labelled samples were produced from the dissolution of nickel in ^{15}N labelled nitric acid solution obtained from Sigma-Aldrich. The silica and titania were from Grace and Evonik respectively. A sample of PtO_2 was acquired from Sigma Aldridge, experiments mixed this with γ-alumina SCFa-140. The sample was later ball milled for 2 hours at 3000 rpm in a speed mixer DAC 150 FVZ with six yttria-stabalised zirconia balls (0.5 mm diameter) and a colour change from dark to paler brown was observed.

5.2.2 NMR Measurements

Single pulse ^1H measurements were carried out on a 14.1 T (Bruker Avance II+-600) spectrometer using a Bruker 2.5 mm probe which failed between data sets, collection continued with a Bruker 1.3 mm probe, both were operated at an MAS frequency of 30 kHz. Calibration of π/2 pulses were carried out on α-Alanine where the CH_3 peak was calibrated to 1.1 ppm, this was a secondary reference to Me_4Si the IUPAC reference.[132] The pulse delay was set to 5 s and no more than a maximum of 64 transients were required.

The ^{15}N NMR measurements were carried out as described previously in Section 3.2.3. A CPMAS90 experiment was used to calibrate the π/2 pulse. Repeat measurements for the sample of ^{15}N labelled sample on silica were performed on the 14.1 T Bruker Avance II+-600 spectrometer using a Hahn π/2–τ–π–τ pulse sequence. All measurements presented used a pulse delay of 300 s and ran for ~15 hours.

All ^{29}Si and ^{195}Pt NMR measurements were carried out on a Bruker Avance HD 7.05 T spectrometer. The ^{29}Si measurements were calibrated on kaolinite (-92 ppm) as a secondary reference as a secondary reference to Me_4Si (0 ppm).[133] CPMAS experiments used a π/2(^{1}H) of 3.5 μs and a contact time of 4 ms with decoupling using a pulse delay of 5 s. A π/2(^{29}Si) pulse was also calibrated on kaolinite and the direct measurements of ^{29}Si used decoupling during the acquisition with a pulse delay of 240 s. The ^{195}Pt measurements used a 7 mm static Bruker ATMA probe which had auto tuning capabilities. The ^{195}Pt was all acquired using the VOCS method stepping every 50 kHz using a Hahn echo pulse sequence with π/2(^{195}Pt) 2 μs and a 7 s pulse delay.

5.3 Results and Discussion

5.3.1 Pt and Ni Precursors Supported on α-Al_2O_3

Preliminary ^{1}H and ^{27}Al measurements were undertaken on α-Alumina samples with no or low metal loadings, these are summarised in Figure 5-1. The predominant ^{1}H resonance in the series can be seen to be at ~7.7 ppm and a smaller resonance at ~2.2 ppm. As discussed earlier these resonances represent hydroxyls which are either clustered or isolated and are marked by the solid lines in Figure 5-1. The dashed line indicates the region where physorbed water should appear, however, the only sample to be significantly affected by this was the Pt nitrate sample prior to calcination. As expected upon calcination the water resonance can be seen to drastically decrease with respect to the downfield hydroxyls.

The presence of the water resonance in the platinum samples was the most significant change across the α-alumina suite of samples. The $Ni(NO_3)_2/\alpha\text{-}Al_2O_3$ materials pre- and post-calcination do not show significant difference to the unloaded support, even though the metal loading was higher than the Pt materials. The ^{27}Al spectra shows a characteristic AlO(VI) peak at 14.2(5) ppm which agrees with the literature value of 13.9 ppm.[127]

It is not clear from the current measurements how the catalysts are interacting with the support. Furthermore, the low pore volumes of α-alumina make impregnation of higher loadings more difficult. A higher loading of platinum would allow for further as insight, as shown with the γ-alumina studies below.

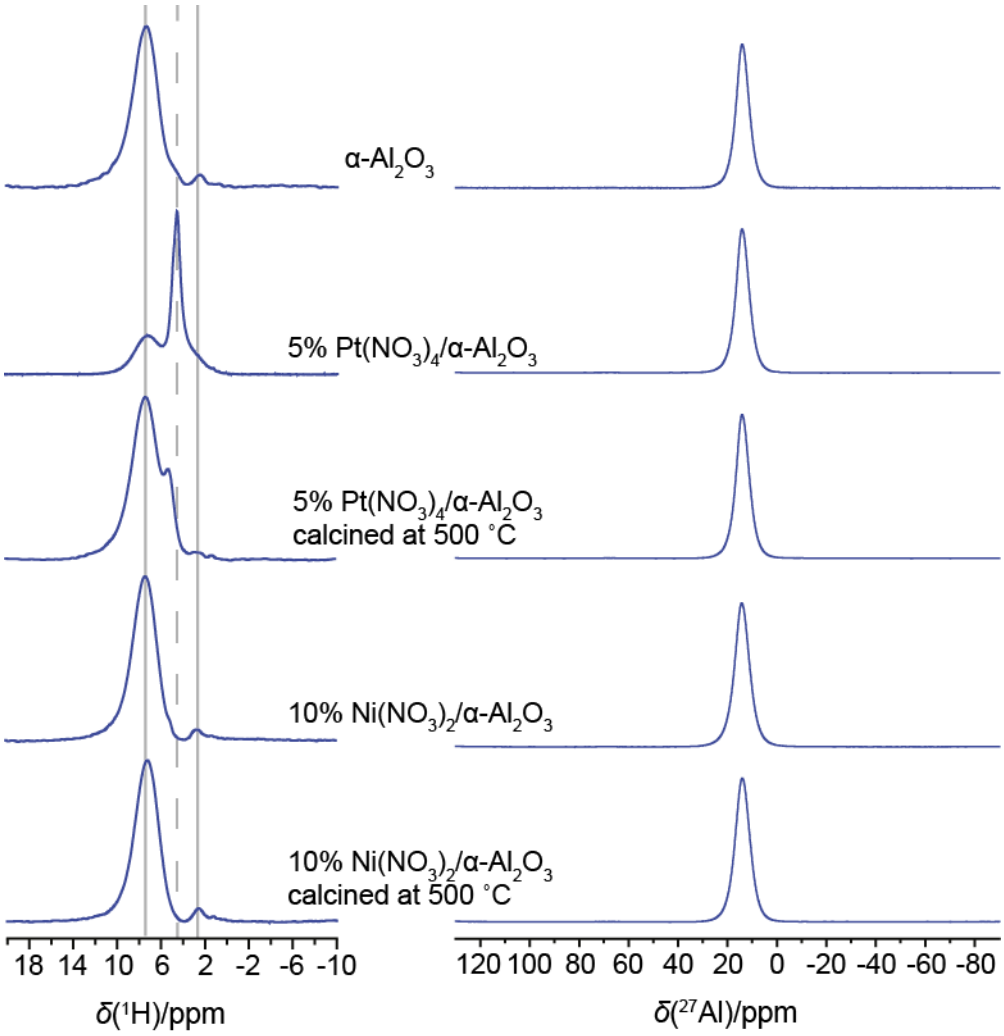

Figure 5-1: ^{1}H 30 kHz MAS and ^{27}Al 20 kHz MAS measurements of untreated and calcined samples carried out at 14.1 T on $\alpha\text{-}Al_2O_3$.

5.3.2 Pt and Ni Precursors Supported on γ-Al_2O_3

From Figure 5-2 the ^{1}H and ^{27}Al data for nickel and low loadings of platinum on the γ-alumina support are presented. The ^{1}H data shows comparable resonances to the previous results for α-alumina. However, the Ni nitrate samples suffer broadening and a significant loss of resolution amongst the ^{1}H measurements. This could be attributed to the Ni nitrate which contains six water molecules, thus increased loadings would contain more H_2O. The calcined nickel sample (10% $Ni(NO_3)_2$/γ-Al_2O_3 calcined at 500 ˚C) can be seen to have the single and clustered hydroxyls, as seen previously, and the species at ~3 ppm which bridge between aluminium nuclei.

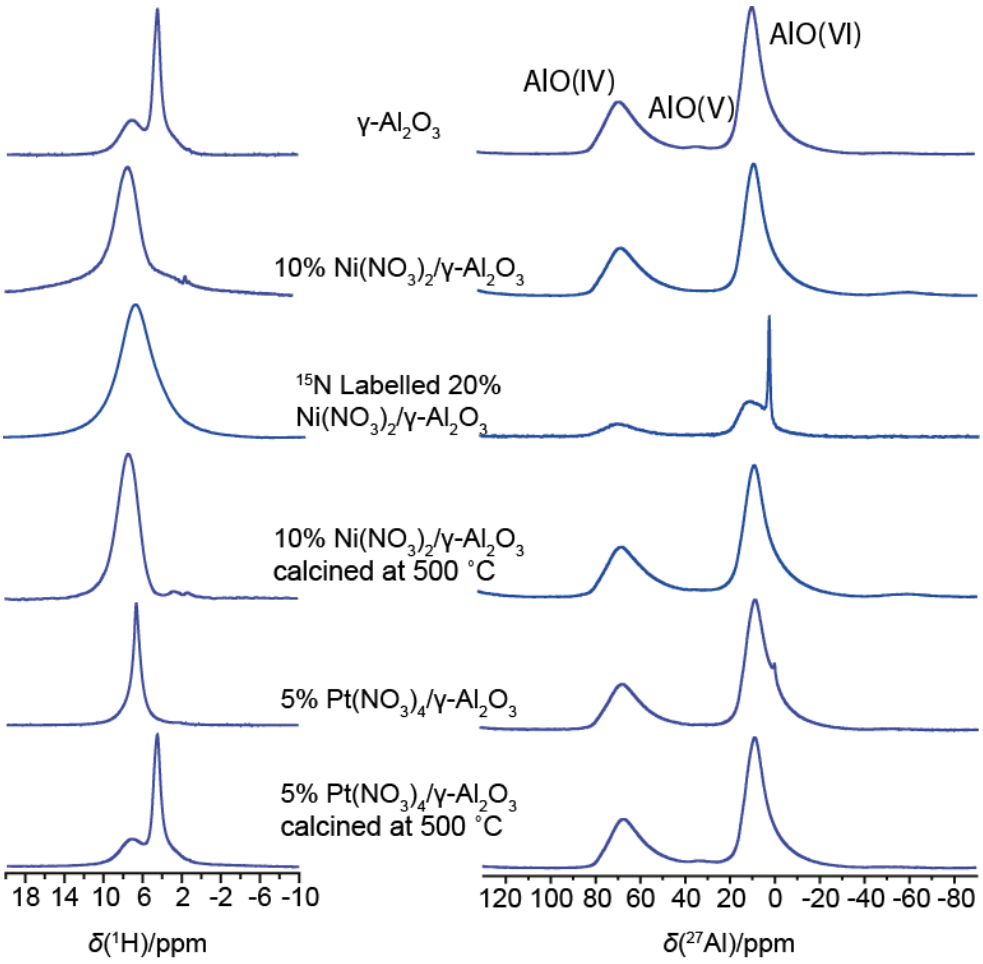

Figure 5-2: ^{1}H and ^{27}Al MAS NMR at 30 kHz and 20 kHz respectively, of no loading and low loaded samples on γ-Al_2O_3.

The ^{27}Al NMR spectra are indicative of γ-alumina, demonstrating the AlO(IV), and AlO(V) and AlO(VI) sites which are known to be disordered, a feature identified by the tailing on the up field side of the resonance. However, the most striking change amongst the data set is the sharp resonance at 2.36 ppm. This is a very narrow AlO(VI) resonance has a high degree of motion and was a product of the impregnation, thus, it is probably a surface species. Furthermore, the presence in both platinum and nickel loading indicates a common cause. Thus, a reaction with nitric acid may have occurred producing a motional aluminium nitrate compound. This has been observed in zeolites where nitric acid has caused Al leaching from the main structure.[134]

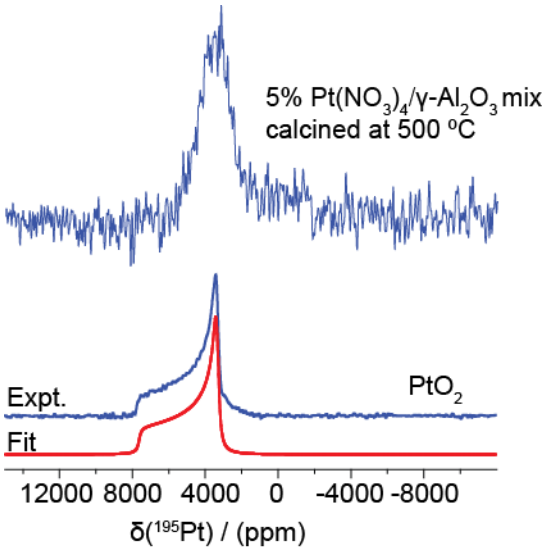

Figure 5-3: ^{195}Pt static solid-state NMR of 5% $Pt(NO_3)_4/\gamma$-Al_2O_3 and PtO_2 acquired via VOCS method with stepping every 50 kHz requiring ~15 slices each.

The IUPAC reference for ^{27}Al is aluminium nitrate solution, however, the resonance here was seen is at ~2 ppm. The difference between aluminium nitrate in solution and that observed in the measurements may be due to continued attachment to the alumina network. Furthermore, upon calcination the species must decompose as it is no longer seen in the PtO_2 or NiO_2 samples with the aluminium returning to the main structure.

An initial ^{195}Pt NMR measurement of the calcined platinum nitrate sample (5% $Pt(NO_3)_4/\gamma$-Al_2O_3 calcined at 500 ˚C) can be seen in Figure 5-3. A resonance with a

centre of gravity can be seen at 3400 ppm and a potential second at ~300 ppm. However, the signal to noise limits the analysis masking any CSA features and the analysis of the second site. Previous studies of platinum nanoparticles reported a possible resonance for PtO at 1750 ppm in the solid state.[12]

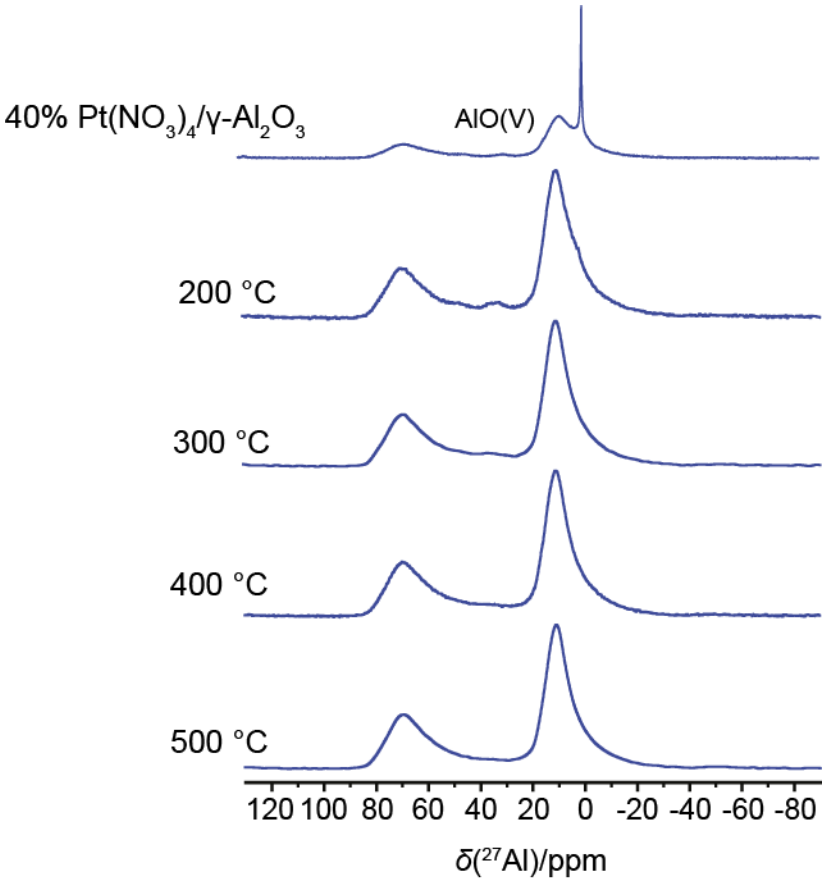

Figure 5-4: ^{27}Al NMR measurements at 20 kHz MAS of Pt nitrate on γ-alumina calcined at different temperatures.

A sample of PtO_2 was also measured yielding a resonance in a comparable region to the catalyst sample. A characteristic CSA lineshape was observed and is shown in Figure 5-3. Thus, an δ_{iso} of 4607 ppm was extracted with a Ω of 3916 ppm and a κ of -1.00, these parameters are summarised in Table 5-1. The span (κ) indicates an axially symmetric environment. The NMR VOCS measurement of 5% $Pt(NO_3)_4/\gamma$-Al_2O_3 calcined at 500 ˚C shown in Figure 5-3 is insufficient to observe a CSA characteristic lineshape.

To further utilise ^{195}Pt solid state static solid state NMR the platinum loading was drastically increased beyond the typical few percent for hydrogenation catalysts.[11] Although much higher loadings up to ~40% are used in fuel cell applications.[135] Figure 5-4 shows samples of platinum nitrate supported on γ-alumina at 40% loading (by weight) which were calcined between 200 ˚C and 500 ˚C. The first sample shown, prior to calcination, contains a significant amount of aluminium nitrate, relative to what was seen before. However, this has almost completely vanished from the NMR spectra that 200 ˚C indicating the removal of the nitrate anions.

In addition to the AlO(IV) and AlO(VI) resonances expected for γ-alumina, AlO(V) can also be seen. The presence of AlO(V) in γ-alumina when studied at sufficiently high magnetic field and MAS spinning speed has been carried out previously. Furthermore, the Al environment has been observed to be exclusively present on the surface and is thought to be a preferential anchoring site for catalysts.[129] Four

Table 5-1: CSA parameters for the ^{195}Pt fits shown in Figure 5-5 and Figure 5-7 for $Pt(NO_3)_4/\gamma$-Al_2O_3.

Name	**Peak assign-ment**	δ_{iso}[a] **(ppm)** (±100)	δ_{11}[b] **(ppm)** (±100)	δ_{22}[b] **(ppm)** (±50)	δ_{33}[b] **(ppm)** (±100)	Ω[c] **(ppm)** (±150)	κ[c] (±0.08)	$\Delta\delta$[d] (±100)	η[d] (±0.05)
PtO_2	1	4607	7218	3302	3302	3916	-1.00	3916	0.00
$Pt(NO_3)_4/\gamma$-	1	4017	5642	3651	2758	2884	-0.84	2438	0.55
Al_2O_3	2*	4035	-	-	-	-	-	-	-
200 ˚C	1	3897	5691	3314	2686	3005	-0.58	2691	0.35
	2*	3833	-	-	-	-	-	-	-
300 ˚C	1	3897	5691	3314	2686	3005	-0.58	2691	0.35
	2*	3833						-	-
400 ˚C	1	4044	6279	3284	2569	3710	-0.61	3353	0.32
	2*	3861	-	-	-	-	-	-	-
	3	-169	-	-	-	-	-	-	-
500 ˚C	1	4064	6083	3600	2509	3574	-0.39	3028	0.54
	2*	4139	-	-	-	-	-	-	-
	3	908	-	-	-	-	-	-	-

[a]–IUPAC isotropic shift convention: $\delta_{so} = (\delta_{11} + \delta_{22} + \delta_{33})/3$.

[b]– IUPAC shift convention: $\delta_{11} \geq \delta_{22} \geq \delta_{33}$.

[c] – Herzfeld-Berger shift convention: $\delta_{11} \geq \delta_{22} \geq \delta_{33}$ (tensorial representation not shown above), $\delta_{iso} = (\delta_{11} + \delta_{22} + \delta_{33})/3$, $\Omega = (\delta_{11} - \delta_{33})$, $\kappa = 3(\delta_{22} - \delta_{iso})/ (\delta_{11} - \delta_{33})$ $(1 \geq \kappa \geq -1)$.

[d] – Haeberlen shift convention: $|\delta_{33} - \delta_{iso}| \geq |\delta_{11} - \delta_{iso}| \geq |\delta_{22} - \delta_{iso}|$ (tensorial representation shown above), $\delta_{iso} = (\delta_{11} + \delta_{22} + \delta_{33})/3$, $\Delta\delta = \delta_{33} - 1/2(\delta_{11} + \delta_{22}) = 3/2(\delta_{33} - \delta_{iso})$,
$\eta_\delta = (\delta_{22} - \delta_{11})/ (\delta_{33} - \delta_{iso})$ $(1 \geq \eta_\delta \geq 0)$.

* – Gaussian/Lorentzian line fitted to replicate an anisotropic broadening of a CSA environment.

platinum nuclei have been observed to share each AlO(V) site. and at high loadings ~20 platinum atoms bind across several Al(V) sites creating 2D structures.[136]

These studies explain the observation of AlO(V) sites at lower calcination temperatures and their evolution. The loss of the AlO(V) resonance through the series could be due to a transition to AlO(VI), where the Al–O bond that would be gained is of the form Al–O–Pt. The use of a multiple quantum MAS (MQMAS) experiment

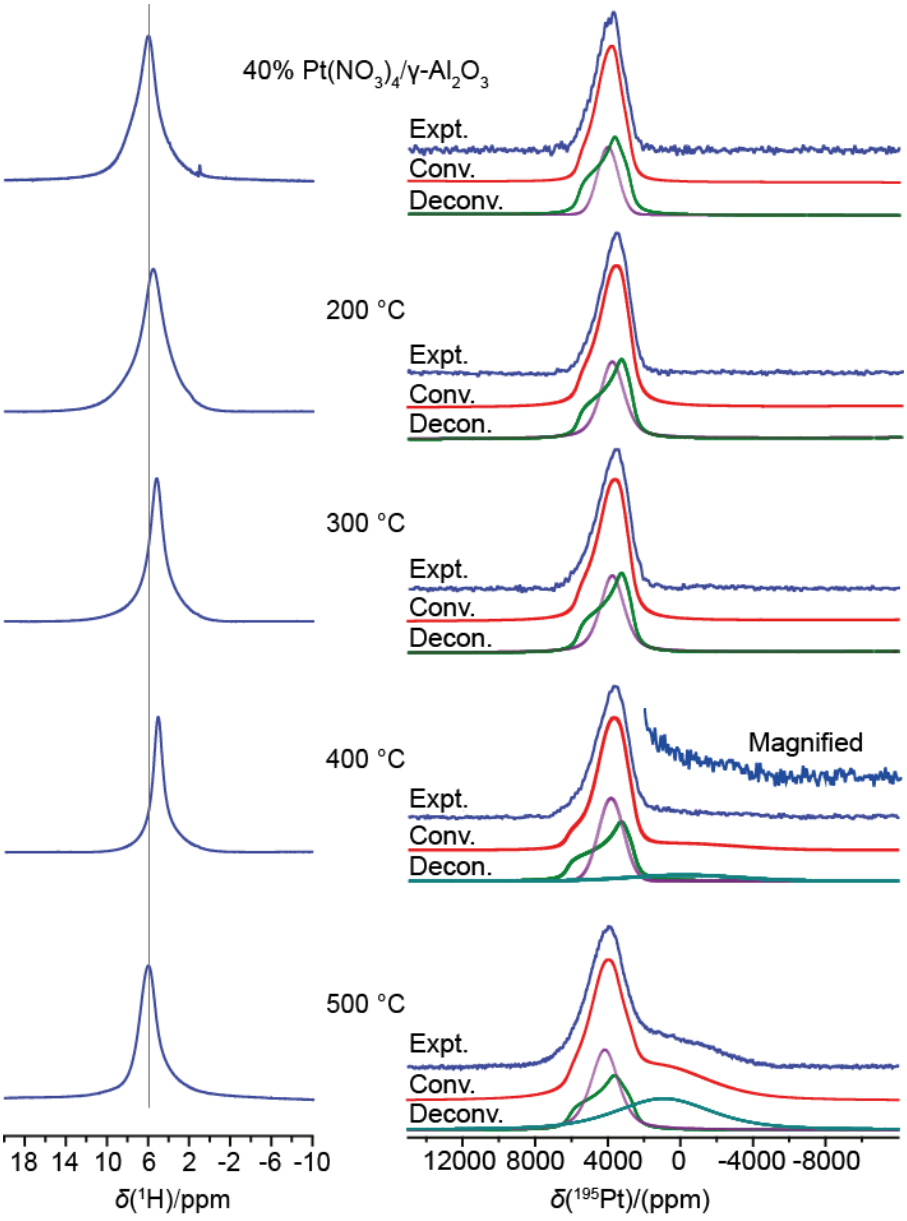

Figure 5-5: ^{1}H 30 kHz MAS NMR at 14.1 T and ^{195}Pt static NMR at 7.05 T of the calcined γ-alumina samples.

which can be used to distinguish overlapping quadrupolar resonances. Thus, it may be possible to identify multiple AlO(V) sites. In addition, it may also be able to distinguish these surface AlO(VI) sites from the AlO(VI) of the bulk.[137]

The lack of resolution seen in the ^{1}H measurements presented in Figure 5-5 make any analysis from this perspective difficult. However, the line width does appear to decrease as the calcination temperature is increased. This may be related to the removal of water.

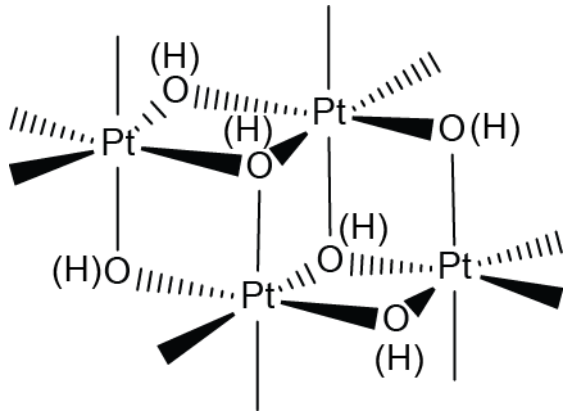

Figure 5-6: Proposed form of the oligomeric structures which deposit out of solution, the terminal ligands shown have the potential of being terminal hydroxyls or nitrates. The protons in the parentheses show potential for OH or O bridges. It would also be possible for more (or less) platinum units to be included in the schematic.

Extraction of NMR parameters for the ^{195}Pt measurements shown in Figure 5-5 are summarised in Table 5-1. The complexity of platinum nitrate solutions has been discussed previously (Section 0) and previous solution studies have identified several platinum complexes which make up oligomeric type structures including $[Pt(\mu\text{-}OH)_3(NO_3)_3]^{2-}$ (~4340 ppm), $[Pt(\mu\text{-}OH)_4(NO_3)_2]^{2-}$ (~4245 ppm)and $[Pt(\mu\text{-}OH)_6]^{2-}$ (3845- 4100 ppm).[138] However, comparisons to solid state ^{195}Pt measurements are almost redundant due to the significant CSA interaction already seen, except to allude to a window of interest.

From the literature studies of platinum nitrate solutions, it is thought oligomeric structures are depositing on to the surface of the catalyst support. The form of these structures would most probably be similar to that shown in Figure 5-6 (adapted from the literature[124,138]). The Pt oxide structure proposed in Figure 5-6 would

demonstrate octahedra about the Pt centres with several platinum oxide complexes bridge to one another. The bridges between platinum sites are thought to be oxygen or hydroxyls the mixture of both would likely cause a local disorder of the environments. This disorder may be why the ^{195}Pt measurements of platinum nitrate materials in Figure 5-3 and Figure 5-5 demonstrate broad relatively featureless resonances rather than the clear CSA line of PtO_2. Furthermore, PtO_2 forms as sheets of Pt bridged by O.[139] The structural difference would likely cause a difference in the Pt–Pt distances of the two structures which would explain differences in isotropic chemical shift.

The lineshape analysis of the platinum nitrate materials is thought to contain a single environment, however, the deconvolutions shown in Figure 5-5 include a Gaussian/Lorentzian (which has been faded to attempt to distinguish it from the CSA lineshape). This convolution has been carried out to emulate an asymmetric broadening of the environment. Physically this would indicate a preferential orientation. From the literature, the oligomeric species are thought to form in sheets which may offer a potential explanation. The CSA environment extracted from the 40 % $Pt(NO_3)_4/\gamma$-Al_2O_3 sample has an δ_{iso} of 4017 ppm, 600 ppm smaller than seen for PtO_2. A greater shielding of the nucleus may be due to the larger bridged structures that are thought to form. Both materials were close to axially symmetric but the Ω of the 40 % $Pt(NO_3)_4/\gamma$-Al_2O_3 was 2884 ppm much smaller than the PtO_2 (3916 ppm).

Upon calcination, the ^{195}Pt continues to display the asymmetric broadening, but very little change was observed at 200 ˚C and 300 ˚C. However, at 400 ˚C a second ^{195}Pt NMR environment was observed, although this is only just resolvable as seen from the magnified region of the spectrum. This is thought to be the oligomeric structures anchoring to the surface. At 500 ˚C the supported Pt oxide resonance is clear, the chemical shift initially at -169 ppm can now be seen to be more deshielded at 908 ppm. The change in the chemical shift for the supported platinum may initially have a significant error due to its the small intensity. Both measurements at 400 ˚C and 500 ˚C show a change in the unsupported resonance and indicate an increase in the

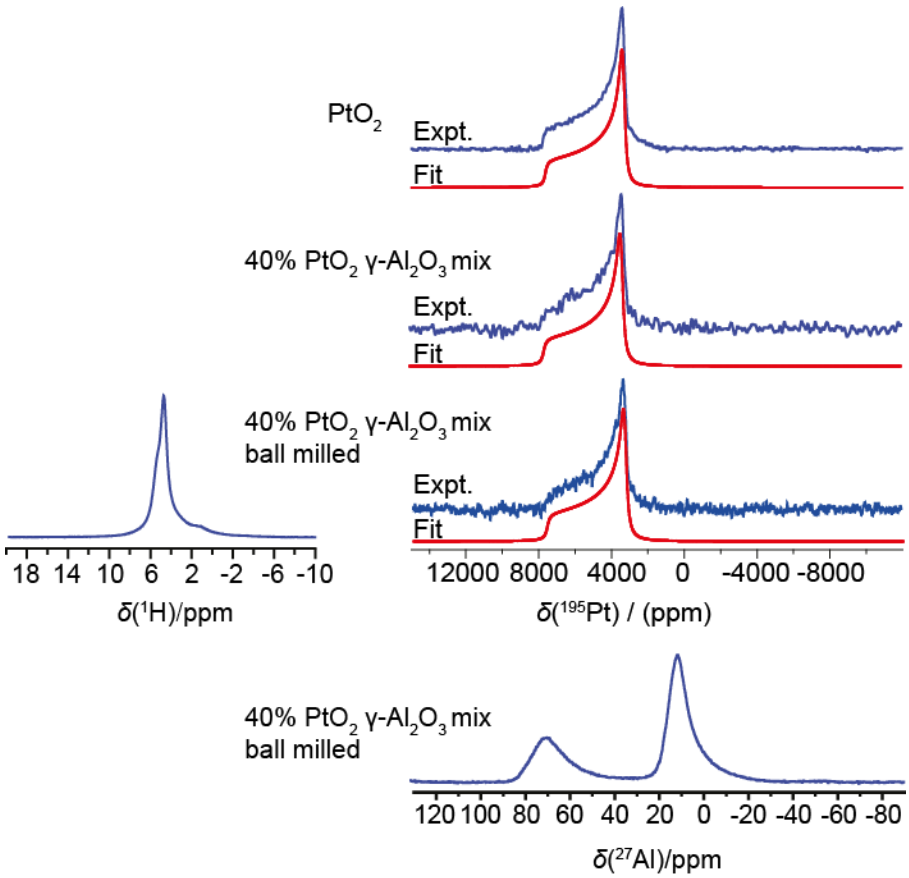

Figure 5-7: ^{195}Pt static solid-state NMR measurements of commercial PtO_2 which was then mixed with γ-alumina and finally ball milled. The ^{1}H and ^{27}Al of the ball milled sample are also included.

amount of preferentially ordered platinum. There is also a decrease in axial symmetry by the end of the calcination process of the unsupported species.

It is unclear how stable the unsupported structures associated with the initial platinum nitrate resonances are. It may be possible to remove the species if samples were washed. Studies of the washed samples may provide insight into surface interactions. A study of the resultant catalysts and the NMR measurements of Pt metal may also provide further detail into particle size and morphology, this has been shown previously.[12]

Measurements of the commercial PtO_2 are presented in Figure 5-7 to understand the effect of mixing with γ-alumina. No platinum-alumina interactions were observed with the resonance maintaining the characteristic CSA lineshape. This was also

observed in the ^{27}Al measurement presented in Figure 5-7. This was the same after ball milling the mixed sample, which has a corresponding ^{1}H spectrum. The ^{1}H measurements have better resolution that previously seen, this may be a removal of water. Quantification of the ^{1}H signal may aid explain the change is relative species.

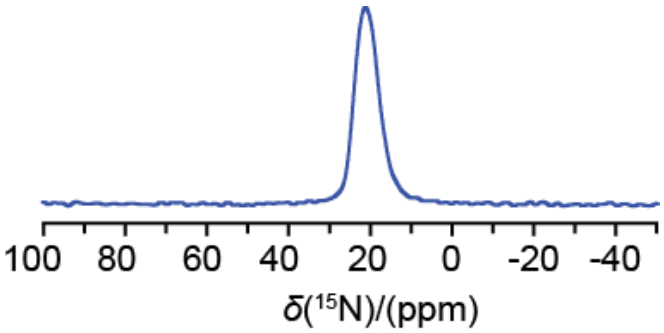

Figure 5-8: ^{15}N single pulse MAS at 12 kHz NMR measurement of $Ni(NO_3)_2/\gamma$-Al_2O_3.

To understand the role of the nitrates in the synthesis a ^{15}N labelled $Ni(NO_3)_2/\gamma$-Al_2O_3 sample was made. The ^{15}N NMR of this can be seen in Figure 5-8. The resonance is at ~21 ppm, which is the region for NO_3.[64] A single pulse experiment was required due to difficulties achieving cross polarisation. This, indicates a nitrate anion rather than nitric acid. Thus, the reaction with the alumina surface seen previously may cause a loss of the proton with the formation of an aluminium nitrate species in the ^{27}Al NMR.

5.3.3 Pt and Ni Precursors Supported on SiO_2

The calcination of platinum nitrate on silica at different temperatures was also studied, via ^{1}H, ^{29}Si and ^{195}Pt NMR. The ^{1}H and ^{195}Pt NMR measurements can be seen in Figure 5-9, the parameters of the deconvolutions are summarised in Table 5-2 and Table 5-3. Both nuclei demonstrate narrow resonances in the un-heated samples unlike that seen previously. Four ^{1}H NMR resonances were observed at 8.1 ppm, 8.5 ppm and 8.9 ppm which are hydroxyls making up ~98% of the signal, these motional hydroxyls suppress the water resonance which is at 4.7 ppm. The narrowing of the Pt and H resonances may indicate motion of the chemical species. Coupled with the

Table 5-2: ^{1}H 30 kHz MAS NMR parameters following the proton measurements of platinum nitrate on silica calcined at different temperatures.

Name	**Peak assignment**	**δ_{iso}(^{1}H)/ppm** (±0.1)	**Integrated intensity/%** (±0.5)
$Pt(NO_3)_4/SiO_2$	1	4.7	1.9
	2	8.1	31.7
	3	8.5	48.1
	4	8.9	18.3
200 ˚C	1	6.7	100
300 ˚C	1	5.8	85.5
	2	6.9	8.0
	3	8.4	6.5
400 ˚C	1	5.4	71.6
	2	7.1	28.4
500 ˚C	1	5.0	83.6
	2	7.2	10.2
	3	8.8	6.2

large ^{1}H chemical shifts the oligomeric structures may be H-bonding to surface hydroxyls in a way that allows dynamic freedom.

From the ^{195}Pt NMR VOCS measurements of the initial platinum nitrate sample ($Pt(NO_3)_4/SiO_2$) two CSA lineshapes at 3752 ppm and 3923 ppm were extracted. shown in parentheses). The amount of motion the oligomeric structures experience may be indicative of their size. Where the smallest structures are very narrow and have the leave Pt neighbours. This may explain the very narrow resonance which was observed at 4362 ppm. Thus, the other two species are larger and may experience H-bond differently when the structures are larger.

Upon calcination, both narrow resonances were seen to disappear, with the ^{1}H signal becoming overall more shielded and broadened. The ^{195}Pt NMR of $Pt(NO_3)_4/SiO_2$ 200 ˚C can be seen to be similar to the $Pt(NO_3)_4/\gamma$-Al_2O_3 samples where assignments were made to oligomeric structures. This is reflected in the δ_{iso} of 3891 ppm compared to 3986 ppm observed in $Pt(NO_3)_4/\gamma$-Al_2O_3, well within the error.

Calcination at 300 ˚C was observed to cause the ^{195}Pt species move down field to 4260 ppm. This change may be due to dehydration of the Pt nitrate which has been reported in this temperature region previously.[124] There was also a change in the CSA

parameters, with the Ω increasing by ~800 ppm from 200 ˚C to 300 ˚C in conjunction with an increase in axial symmetry. These changes may also be due to the removal

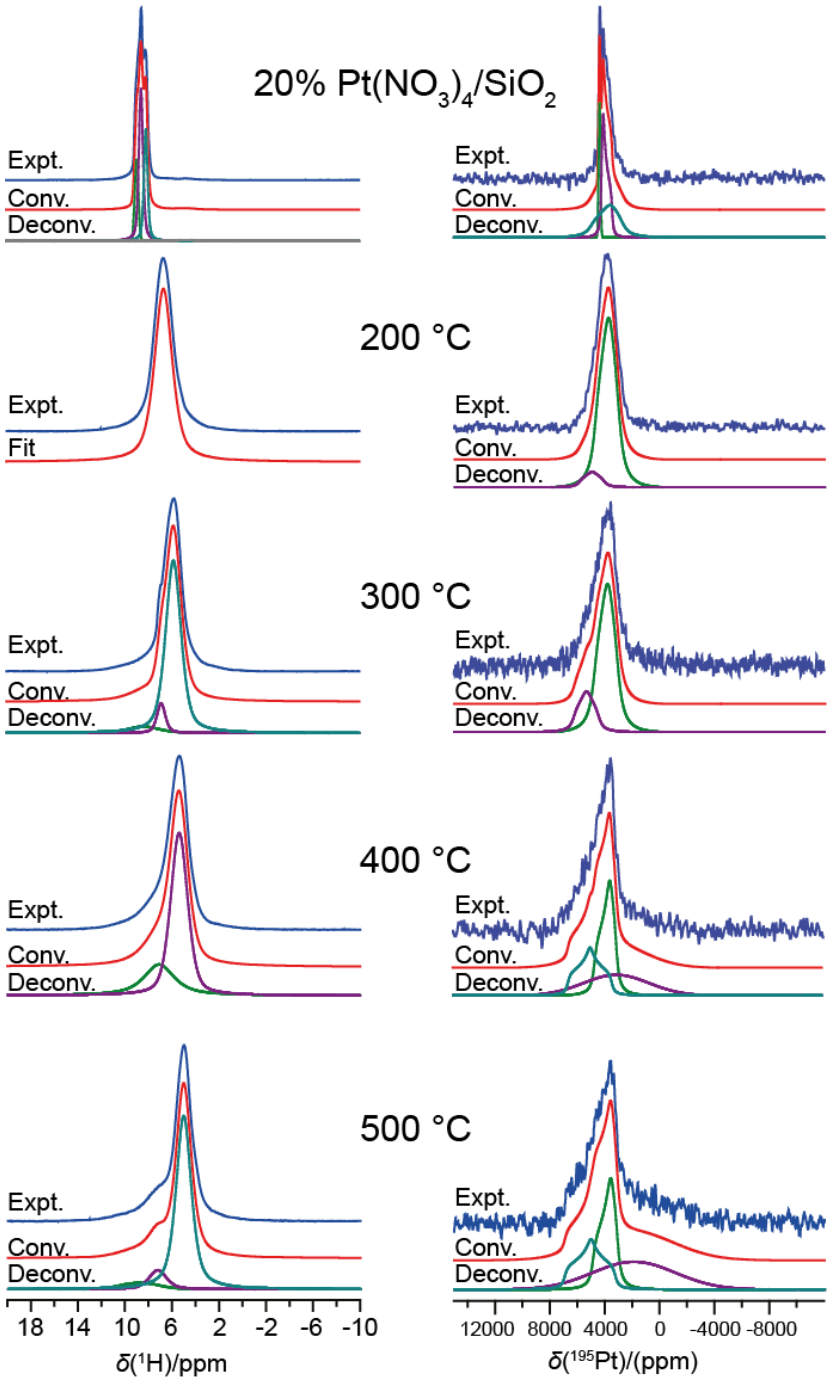

Figure 5-9: ^{1}H 30 kHz MAS measurements at 14.1 T and ^{195}Pt static VOCS measurements at 7.05 T following the calcination of platinum nitrate on silica at different temperatures.

of nitrates although this is a higher temperature than was observed in the γ-alumina materials. Through the series, the ^{195}Pt resonance for unsupported oligomeric structures were observed to have increased axial symmetry although the narrowing seen initially was lost.

From the ^{29}Si CPMAS measurements of $Pt(NO_3)_4/SiO_2$ shown in Figure 5-10 a change in the polarisation transfer efficiency to Q_4 was observed to occur between 200 to 300˚C. Comparing the single pulse measurements for this temperature step demonstrates actual amounts of each species did not change. Thus, a loss of H_2O stored in the silica network occurred. The loss of water increased the resolution of the proton measurements and three ^{1}H resonances can be deconvoluted, a shoulder is at 6.9 ppm, the main peak at 5.8 ppm and small hydroxyl species is observable at 8.4 ppm.

At 400 ˚C the proton resonances continue to become more shielded. The resonance at 5.4 ppm likely due to remaining water. A small species up field is also present at 7.1 ppm which could be an evolution of the hydroxyl species seen in the previous

Table 5-3: ^{195}Pt NMR parameters for platinum nitrate on silica calcined at different temperatures.

Name	**Peak assign-ment**	δ_{iso}[a] **(ppm)** (±100)	δ_{11}[b] **(ppm)** (±100)	δ_{22}[b] **(ppm)** (±50)	δ_{33}[b] **(ppm)** (±100)	Ω[c] **(ppm)** (±150)	κ [c] (±0.08)	$\Delta\delta$[d] (±100)	η[d] (±0.05)
$Pt(NO_3)_4/SiO_2$	1	3752	4961	3583	2712	2249	-0.23	1814	0.72
	2	3923	4219	4104	3445	774	0.7	-717	0.24
	3	4362(20)	-	-	-	-	-	-	-
200 ˚C	1	3891	5320	3505	2848	2472	-0.47	2144	0.46
	2*	3984	-	-	-	-	-	-	-
300 ˚C	1	4260	6201	3600	2979	3222	-0.61	2912	0.32
	2*	4073	-	-	-	-	-	-	-
400 ˚C	1	4355	6447	3340	3278	3169	-0.96	3138	0.03
	2*	3891	-	-	-	-	-	-	-
	3	2208	-	-	-	-	-	-	-
500 ˚C	1	4413	6577	3342	3320	3257	-0.99	3246	0.01
	2*	4002	-	-	-	-	-	-	-
	3	1745	-	-	-	-	-	-	-

[a]–IUPAC isotropic shift convention: $\delta_{iso} = (\delta_{11} + \delta_{22} + \delta_{33})/3$.

[b]– IUPAC shift convention: $\delta_{11} \geq \delta_{22} \geq \delta_{33}$.

[c] – Herzfeld-Berger shift convention: $\delta_{11} \geq \delta_{22} \geq \delta_{33}$ (tensorial representation not shown above), $\delta_{iso} = (\delta_{11} + \delta_{22} + \delta_{33})/3$, $\Omega = (\delta_{11} - \delta_{33})$, $\kappa = 3(\delta_{22} - \delta_{iso})/ (\delta_{11} - \delta_{33})$ $(1 \geq \kappa \geq -1)$.

[d] – Haeberlen shift convention: $|\delta_{33} - \delta_{iso}| \geq |\delta_{11} - \delta_{iso}| \geq |\delta_{22} - \delta_{iso}|$ (tensorial representation shown above), $\delta_{iso} = (\delta_{11} + \delta_{22} + \delta_{33})/3$, $\Delta\delta = \delta_{33} - 1/2(\delta_{11} + \delta_{22}) = 3/2(\delta_{33} - \delta_{iso})$, $\eta_\delta = (\delta_{22} - \delta_{11})/ (\delta_{33} - \delta_{iso})$ $(1 \geq \eta_\delta \geq 0)$.

* – Gaussian/Lorentzian line fitted to replicate an anisotropic broadening of a CSA environment.

sample. The ^{195}Pt VOCS measurements of the 400 ˚C has now begun to interact with the surface. This was characterised by the broad resonance at 2208 ppm. However,

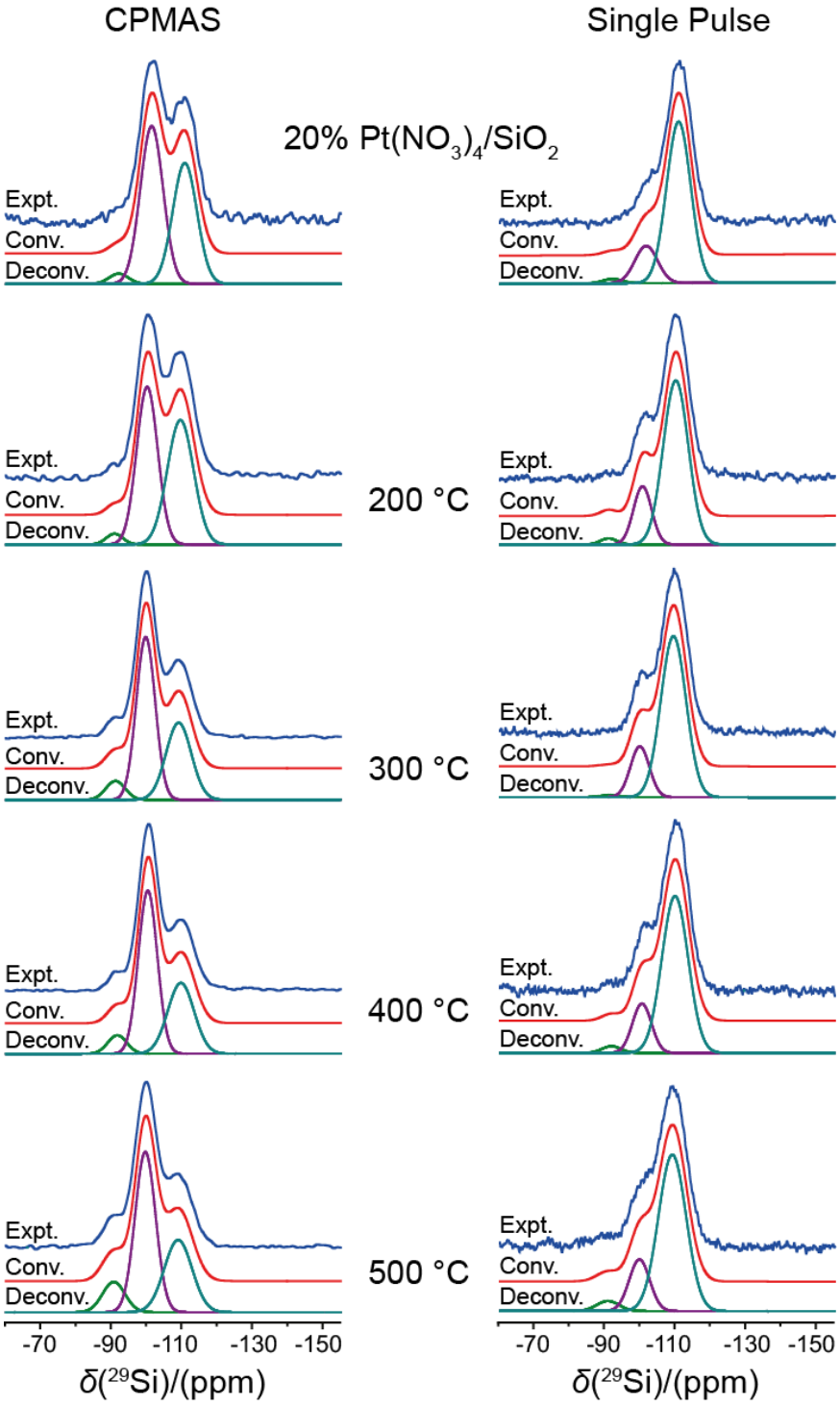

Figure 5-10: ^{29}Si 5 kHz MAS NMR at 7.05 T, assignment of speciation using CP experiments and quantification via direct excitation single pulse measurements.

Table 5-4: ^{29}Si speciation and NMR parameters, δ_{iso} found from CPMAS experiments and relative amounts found from direct measurements.

Name	**Peak assignment**	**δ_{iso} (ppm)** (±0.2)	**Relative amount (%)** (±0.5)
$Pt(NO_3)_4/SiO_2$	Q_2	-93.7	1.8
	Q_3	-103.6	17.6
	Q_4	-113.5	80.6
200 ˚C	Q_2	-92.6	1.9
	Q_3	-102.3	20.1
	Q_4	-112.2	78.0
300 ˚C	Q_2	-92.9	0.8
	Q_3	-101.9	19.0
	Q_4	-111.7	80.2
400 ˚C	Q_2	-93.4	2.5
	Q_3	-102.5	18.0
	Q_4	-112.4	79.5
500 ˚C	Q_2	-92.3	4.0
	Q_3	-101.8	18.8
	Q_4	-111.6	77.2

the signal to noise limits an accurate assignment. From the CSA parameters in Table 5-3 the platinum species at this point can now be seen to be in an axially symmetric environment. Finally, at 500 ˚C more of the oligomeric structures can be seen to interact and bind to the surface. From the increased signal, the resonance was observed at 1745 ppm.

Following the ^{29}Si CPMAS and single pulse data in Figure 5-10, Q_2 to Q_4 were observed which would be expected for bulk and surface species. Quantitatively very little change can be seen through the series for the main bulk of the material consisting of Q_3 and Q_4. The quantitative analysis of these species can be found in Table 5-4. However, at 400 and 500 ˚C as the Pt oxide anchors onto the surface an increase in Q_2 was observed. Thus, indicating a potential for the modification/ interruption of the silica network at the surface. The modification may be of the form Si–O–Pt–O–Si, such Pt has inserted into the surface. However, this is subjective due to the achieved signal to noise of the direct measurement.

A ^{15}N labelled sample of $Ni(NO_3)_2/SiO_2$ was synthesised to gain a better understanding of the role nitrate species. A summary of the ^{1}H, ^{15}N and ^{29}Si measurements are summarised in Figure 5-11 and the parameters extracted are in

Table 5-5: Summary of the NMR parameters and relative amounts of identified species extracted from NMR measurements of the $Ni(NO_3)/SiO_2$ sample with ^{15}N labelling.

$Ni(NO_3)_2/SiO_2$	**Peak assignment**	**δ_{iso} (ppm)**	**Relative amount (%)**
Nuclei:			(±0.5)
^{1}H	1	5.5(1)	35.5
	2	6.1(1)	64.5
^{29}Si	Q_3	-103.6(2)	17.0
	Q_4	-113.5(2)	83.0

Table 5-5. The proton speciation is comparable to that shown for the alumina supported catalysts, Figure 5-2, except for the missing hydroxyl bridging species, which would be expected. On the silica support, only physorbed water and H-bonded silanol groups were observed at 5.5 ppm and 6.1 ppm respectively.[140]

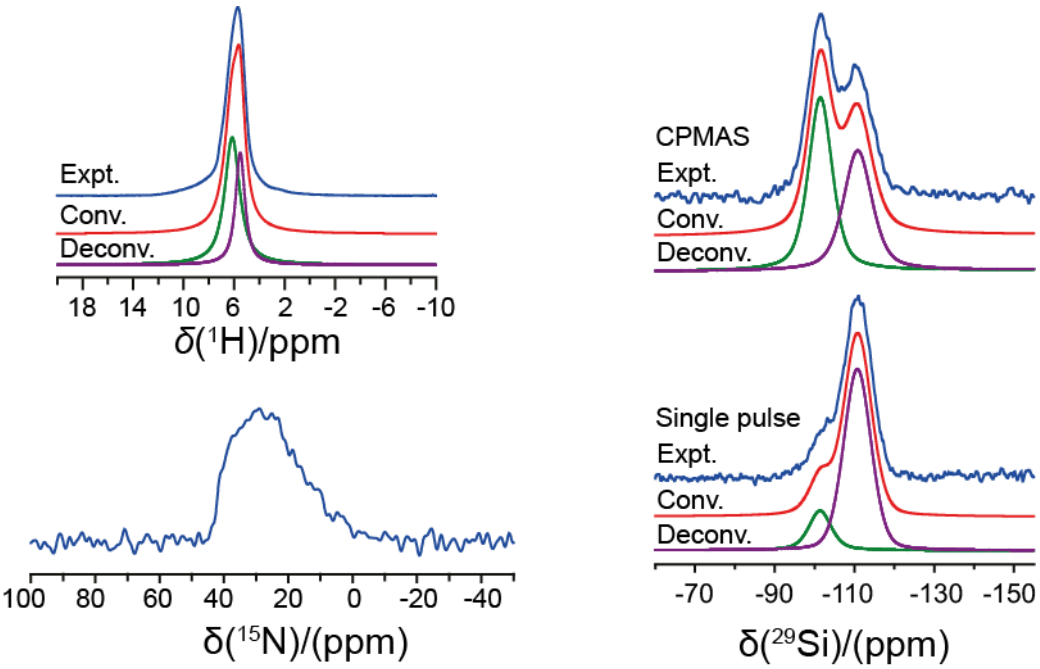

Figure 5-11: ^{1}H, ^{15}N and ^{29}Si solid state MAS NMR of the ^{15}N labelled $Ni(NO_3)_2/SiO_2$ were carried out at rotor frequencies, ν_r = 30, 12 and 5 kHz. The ^{1}H (single pulse) and ^{15}N (Hahn Echo) measurements were carried out at 14.1 T. The ^{29}Si single pulse (with decoupling) and CPMAS were carried out at 7.05 T.

CPMAS measurements of the ^{15}N labelled $Ni(NO_3)_2/SiO_2$ were not achieved and a Hahn echo was used due to the broad nature of the resonance. A very broad lineshape was not expected when compared to the observations seen in the γ-alumina, Figure

5-8, where a single relatively narrow site was seen. Previously it was thought only nitrates were remaining. However, the broad resonance indicates multiple species, which is much more complex than in the alumina example. At this stage, it is thought the $Ni(NO_3)_2/SiO_2$ contains species of nitric acid and nitrates which are similar. These could have several configurations bonding with the surface silica species and nickel species.

The ^{29}Si CPMAS presented in Figure 5-11 appeared to be less efficient requiring more transients and still yielding reduced signal to noise compared to those presented in Figure 5-10. The speciation was comparable to that observed for the platinum nitrate material presented in Figure 5-10 with the same shielded Q_3 and Q_4 units. No Q_2 was observed in Figure 5-11, however, this is based on the CPMAS where observations may be limited by signal to noise limitations. Confirmation of this observation could indicate a preference for the substitution of hydroxyl species on the surface. However, a repeat of measurements utilising spin counting methods would be required.

5.3.4 Pt Precursors Supported on TiO_2

The ^{1}H and ^{195}Pt NMR measurements of platinum nitrate on titania are shown in Figure 5-12. The ^{1}H measurements are comparable to those seen in the alumina samples with little resolution to achieve a confident deconvolution of sites. The resonance at ~6 ppm seen after calcination at 500 ˚C was assigned to hydroxyl bridges between titanium nuclei.[141] The nature of the initial ^{195}Pt VOCS measurements of $Pt(NO_3)_4/TiO_2$, Figure 5-12, demonstrates a similarity to the γ-alumina samples, Figure 5-7 and silica samples Figure 5-9. The initial resonance assigned to the oligomeric structure was initially found at 3918 ppm and no change in δ_{iso} was observed upon calcination. However, there was a change in the CSA parameters, the κ indicates a transformation towards axial symmetry. The mounted platinum oxide can be seen from the deconvolution in Figure 5-12 to be at 2223 ppm, comparable to the previous observations. The much smaller resonance used to simulate anisotropic broadening may indicate the oligomeric structures do not form

as preferentially as seen before. The titania particles used were much smaller than the other supports (nm verses μm) and it is proposed the oligomeric structures may have lacked the surface morphology to form in the sheets proposed previously.

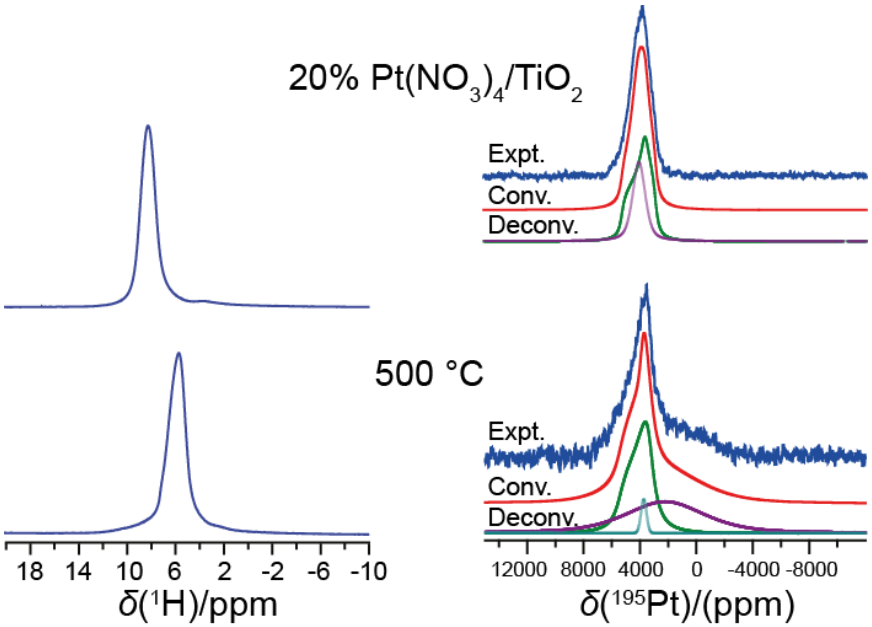

Figure 5-12: Solid state ^{1}H 30 kHz MAS NMR at 14.1 T and ^{195}Pt static VOCS measurements at 7.05 T of $Pt(NO_3)_4/TiO_2$.

Table 5-6: Summary of ^{195}Pt NMR parameters extracted from the platinum nitrate on titania sample not calcined and calcined at 500 °C.

Name	**Peak assign-ment**	δ_{iso}[a] **(ppm)** (±100)	δ_{11}[b] **(ppm)** (±100)	δ_{22}[b] **(ppm)** (±50)	δ_{33}[b] **(ppm)** (±100)	Ω[c] **(ppm)** (±150)	κ[c] (±0.08)	$\Delta\delta$[d] (±100)	η[d] (±0.05)
$Pt(NO_3)_4/TiO_2$	1	3918	5250	3625	2879	2371	-0.37	1998	0.56
	2*	4043	-	-	-	-	-	-	-
500 °C	1	4046	4432	2367	2339	2093	-0.97	2079	0.02
	2*	3936	-	-	-	-	-	-	-
	3	2223	-	-	-	-	-	-	-

[a]–IUPAC isotropic shift convention: $\delta_{so} = (\delta_{11} + \delta_{22} + \delta_{33})/3$.
[b]– IUPAC shift convention: $\delta_{11} \geq \delta_{22} \geq \delta_{33}$.
[c] – Herzfeld-Berger shift convention: $\delta_{11} \geq \delta_{22} \geq \delta_{33}$ (tensorial representation not shown above), $\delta_{iso} = (\delta_{11} + \delta_{22} + \delta_{33})/3$, $\Omega = (\delta_{11} - \delta_{33})$, $\kappa = 3(\delta_{22} - \delta_{iso})/ (\delta_{11} - \delta_{33})$ $(1 \geq \kappa \geq -1)$.
[d] – Haeberlen shift convention: $|\delta_{33} - \delta_{iso}| \geq |\delta_{11} - \delta_{iso}| \geq |\delta_{22} - \delta_{iso}|$ (tensorial representation shown above), $\delta_{iso} = (\delta_{11} + \delta_{22} + \delta_{33})/3$, $\Delta\delta = \delta_{33} - 1/2(\delta_{11} + \delta_{22}) = 3/2(\delta_{33} - \delta_{iso})$,
$\eta_\delta = (\delta_{22} - \delta_{11})/ (\delta_{33} - \delta_{iso})$ $(1 \geq \eta_\delta \geq 0)$.
* – Gaussian/Lorentzian line fitted to replicate an anisotropic broadening of a CSA environment.

5.4 Conclusions

The characterisation of the α-alumina samples yielded confirmation of hydroxyl species identified in literature. However, no interaction between the platinum or nickel nitrate precursors and the support was observed. Dehydration effects from the heat treatment caused the most significant changes of the ^{1}H NMR measurements. The ^{27}Al NMR did not show any changes from the basic α-Al_2O_3 material.

The measurements of γ-alumina lost resolution due to water within the ^{1}H measurements of many of the samples. It was unclear whether this was due to sample contamination or due to higher metal loadings (which introduced excess water into the system). From the ^{27}Al NMR measurements of both Ni and Pt materials on γ-alumina a narrow resonance was observed at 2.36 ppm which was thought to be due to a reaction with nitric acid. Thus, it was assigned to aluminium nitrate, though it was potentially still connected to the alumina network due to shift down field from the IUPAC reference.

Initial ^{195}Pt VOCS measurements were undertaken on a sample of PtO_2 and 5% $Pt(NO_3)_4$/γ-Al_2O_3 calcined at 500 ˚C. The prior sample or PtO_2 yielded an axial symmetric CSA lineshape with Ω of 3916(100) ppm, κ of -1.00(8) and a δ_{iso} of 4607(100) ppm. An attempt to measure a 5% $Pt(NO_3)_4$/γ-Al_2O_3 via ^{195}Pt NMR yielded resonances at ~3400 ppm and ~300 ppm. Utilising a higher platinum loading of 40% by weight, it was possible to deconvolute the spectrum which yielded a CSA lineshape at 4064(100) ppm and an environment at 908(100) ppm from 40% $Pt(NO_3)_4$/ γ-Al_2O_3 calcined at 500 ˚C.

A deshielded environment at ~3900 ppm was observed in the ^{195}Pt VOCS measurements was assigned to unsupported oligomeric structures of platinum oxide bridged by oxygen and hydroxyls. The oligomeric structures demonstrated preferential orientations across all supports. The cause of this was thought to be a preference for the formation of sheets on the surfaces.

As calcination temperature was increased through the γ-alumina series the δ_{iso} was seen to remain relatively similar. The Ω however increased as the structures began to become supported, although during this series the axial symmetry of the environment decreased. As the oligomeric structures interacted with the surface the a highly shielded ^{195}Pt resonance was observed. From the ^{27}Al NMR measurements for the calcination series, AlO(V) was observed in the non calcined sample and low calcination temperatures. This AlO(V) site was seen to disappear, with the supporting of oligomeric structures it was concluded an Al–O–Pt bonding was transforming AlO(V) to AlO(VI).

Impregnation of titania with platinum nitrate produced similar environments to those seen in the γ-alumina. However, upon calcination at 500 ˚C the lineshape fitting did not demonstrate as much preferential orientation dependence as seen previously. Thus, this would indicate dispersed structures due to the titania particle size.

The silica supported platinum nitrate samples demonstrated different phenomena compared to the other oxide supports studied. Prior to calcination motional ^{1}H and ^{195}Pt species were observed as very narrow resonances these were assigned to motional Pt oxide structures H-bonding to the surface. Upon calcination, these resonances broadened which would partly be due to the dehydration of the surface. However, the exact cause could not be identified. Furthermore, temperatures above 200 ˚C the ^{195}Pt data was comparable to the other data sets, indicating a convergence to the generation of similar oligomeric structures seen previously. However, unlike the alumina the ^{195}Pt environment was seen to move towards axial symmetry.

All ^{195}Pt NMR measurements undertaken showed the unsupported oligomeric structure resonance. The continued observation of this upon calcination at 500 ˚C on the 5% sample (the closest to an actual usable catalyst loading) may indicate material which won't aid the catalytic process.

It was apparent that differences between the impregnation of silica and γ-alumina coupled with the observation of aluminium nitrate that nitric acid was a significant factor. Labelled nickel nitrate samples were made supported on silica and γ-alumina.

The latter yielded what appeared to be a single environment at ~21 ppm which seemed to not contain immediate protons as hypothesised. The loss of protons from nitric acid may be in part due to the reaction with the alumina surface. The silica sample however yielded a broad asymmetric resonance which could not be deconvoluted but was likely a convolution of various nitrate species as discussed previously.

In addition to the standard synthesis methods discussed, PtO_2 was mixed with γ-alumina. However, even when ball milled no change in the ^{195}Pt was observed. Thus, it was concluded no PtO_2 interacted with the γ-alumina surface.

5.5 Future Work

The ^{1}H data collected could be improved if spin counting techniques were implemented. The ability to quantifiably compare the samples before and after calcination would greatly aid the exact assignment of hydroxyls and structural protons. This could also be improved if the samples were treated as moisture sensitive and dried prior to undertaking measurements.

Furthermore, 2D correlation experiments such as HMQC and CPMAS from ^{1}H to ^{27}Al would aid understanding of which proton species are lost upon the interaction of the metal oxide catalyst precursor and support, specifically in the γ-alumina case where the literature has shown recent advances.

Washing of the samples and repeating the measurements undertaken would aid in the understanding of initial surface interactions. An understanding of how strong these initial interactions are would be relevant to industrial products if the unsupported species is present as it could represent waste in the final product of a precious metal. Since the resonance has been seen to be clearly distinguish able due to its “narrow” nature, lower loaded samples could be checked for this species. Finally, the reduction of the samples to Pt metal may also aid the study of low Pt loadings due to the greatly reduced relaxation times.

Chapter 6 Summary

6.1 Solid State Characterisation of Isolated Co(III) Ammine Complexes

The solid state study of Co(III) ammine complexes has been shown to be fundamental to gaining an understanding of the Co oxide nanoparticle precipitation. The single crystal XRD measurements identified the isolated complex from the HDC synthesis (using the Co metal precursor) as $[(Co(NH_3)_3)_2(\mu\text{-}OH)_2(\mu\text{-}CO_3)](CO_3)\cdot 5H_2O$. The use of ^{59}Co solid state NMR was then used to confirm this was the same as the complex produced from the $CoCO_3$ synthesis route.

The attempt to acquire a single crystal XRD measurement of $[Co((\mu\text{-}OH)_2 Co(NH_3)_4)_3](SO_4)_3\cdot 9H_2O$ yielded the observation of $[Co(NH_3)_4(\mu\text{-}OH)_2](SO_4)_2 \cdot 2H_2O$ as a precursor material. A dehydrated version (only one crystallographic water) was synthesised and characterised which yielded a single ^{59}Co NMR resonance.

The two Co environments of differing oxo coordination were distinct in the ^{59}Co NMR measurements of Werner's complex, $[Co((\mu\text{-}OH)_2Co(NH_3)_4)_3](SO_4)_3\cdot 9H_2O$. However, single crystal XRD measurements observed disorder of the sulphate anion limiting structural analysis. This was thought to contribute to the limited resolution of the ^{15}N CPMAS measurements of the complex, although there was also less N content. Comparing the ^{1}H and ^{15}N measurements it was concluded inequivalent *cis* ammine groups were present experiencing different direct and indirect couplings to the ^{59}Co nucleus. It was concluded very different Co–N bond lengths were present

which disagrees with the partial crystal structure also presented. The cis ammine ligands were probably influenced differently by the significant H-bonding scheme present with the nine crystallographic waters in the unit cell.

Across the Co(III) complex series $[Co(NH_3)_4CO_3]Br$ was striking. The lack of crystallographic water and direct H-bonding to the bromide counter ion was seen to distinctly effect the NMR measurements. Most striking was the observation of three separated multiplets within the ^{15}N CPMAS measurements. Each multiplet had all eight expected splittings clearly resolved and were assigned to the two inequivalent *trans* groups being more deshielded than the two equivalent *cis* groups.

From the remainder of the Co(III) complex suite several other observations were striking. These complexes yielded axial symmetric lineshapes, although significant CSA interactions were observed to be present. The presence of water or hydroxyl ligands was observed in the CSA parameters of the ^{59}Co measurements. As shown by a change in sign of the skew (κ) compared to when only a carbonate ligand was bound. The span was seen to vary between 1273 ppm and 1510 ppm for carbonatotetrammine complexes. Replacement with hydroxyl and water ligands of the bidentate carbonate was seen to increase this into the range of 2331 ppm to 3095 ppm.

All Co(III) complexes were observed to demonstrate spin-spin coupling of the ^{59}Co nucleus to the ammine ligands. The coupling was perturbed by the quadrupolar interaction, though to different degrees. It was possible to assign *cis*-*trans* effects within the ^{15}N measurements, these were also shown to influence the ^{1}H NMR. It was the *cis* ligands which demonstrated the greatest effects from the quadrupolar perturbed J-coupling. Measured $|^{1}J(^{59}Co,^{15}N)|$ were between 56 Hz and 75 Hz. Furthermore, ammine groups were typically not equivalent within the groupings, potentially due to slight differences in Co–N bond lengths. This limited resolution complicated many of the spectra.

From the ^{59}Co solid state NMR a usable chemical shift reference scale was created. It was observed that each oxo coordinating ligand increased the chemical shift ~800 ppm from pentammine to the centre of Werner's complex. Within a single oxo coordination a disparity of ~1000 ppm was also observed depending on the anion, crystallographic water and type of oxo coordination.

Finally, three unique configurations of carbonate were observed, monodentate, bidentate and bridging. Of these only the bidentate configuration was observed to display spin-spin coupling in the ^{13}C CPMAS measurements. From the single crystal XRD structures this was also the configuration under the most strain due to two of the oxygen binding to the Co, the O–C–O angle was ~110˚.

6.2 Determination of Co Oxide Nanoparticle Precipitation Mechanism

Dissolving the three complexes $[Co(NH_3)_5CO_3]NO_3{\cdot}H_2O$, $[Co(NH_3)_4CO_3]Br$, $[Co(NH_3)_4CO_3](SO_4)_{0.5}{\cdot}1.5H_2O$ and $[(Co(NH_3)_3)_2(\mu\text{-}OH)_2(\mu\text{-}CO_3)](CO_3){\cdot}5H_2O$ in H_2O ensured the solid state ^{59}Co NMR chemical shifts were transferable. The complexes $[Co(NH_3)_5CO_3]^+$ (pentammine) and $[(Co(NH_3)_3)_2(\mu\text{-}OH)_2(\mu\text{-}CO_3)]^{2+}$ (dimeric triammine) were observed to remain relatively stable. However, the tetrammine complexes readily reacted with the water solution evolving into the pentammine and dimeric triammine. In the solid state the carbonates were observed to be more strongly ionic in nature, lacking spin-spin coupling, for the pentammine and dimeric triammine complexes. This was thought to be the reason the complexes remained stable in aqueous media.

During the time resolved measurements of the HDC catalyst syntheses it was concluded the opposite stability was present. The deconvolution of the synthesis observed the pentammine and dimeric triammine readily reacted. The pentammine was thought to convert to $[Co(NH_3)_4CO_3]^+$. The formation of $[(Co(NH_3)_3)_2(\mu$-

$OH)_2(\mu\text{-}CO_3)]^{2+}$ occurred after the other two main complexes, it was not thought to revert back to $[Co(NH_3)_4CO_3]^+$.

The complex $[(Co(NH_3)_3)_2(\mu\text{-}OH)_2(\mu\text{-}CO_3)]^{2+}$ precipitated out of both reactions. However, from the time resolved solution ^{59}Co measurements it was observed the precipitated complex readily redissolved upon mixing. Upon heating and with the support material present the dimeric triammine complex readily isomerised and associated. The evolution could not be expressed explicitly but it is thought the association of the different triammine species occurred to form Werner's complex (or a complex very similar). It is thought the oxo coordinated core of the observed Werner's complex grows rapidly before Co oxide nanoparticles precipitate out of solution. This made observations of it difficult in the HDC synthesis from $CoCO_3$ where Co content was lower.

Thus, details of the Co oxide nanoparticle synthesis have been extracted from the HDC catalyst synthesis. Although details are clearer at the initial stages general complex evolutions have been identified. The information presented should enable continued development of the product, the greater understanding of $[(Co(NH_3)_3)_2(\mu\text{-}OH)_2(\mu\text{-}CO_3)](CO_3)\cdot 5H_2O$ should enable continuous production to be achieved.

6.3 Catalyst Support Interactions

Samples of $Pt(NO_3)_4$ and $Ni(NO_3)_2$ were impregnated onto α-alumina, γ-alumina, silica and titania and calcined at various temperatures. Utilising ^{195}Pt solid state NMR it was shown that from the nitrate solution Pt oxide deposited. Thus, the characterisation of PtO_2 yielded an axial symmetric CSA lineshape, Ω of 3916(100) ppm, κ of -1.00(8) and a δ_{iso} of 4607(100) ppm.

However, the characterisation of $Pt(NO_3)_4$ on all the supports demonstrated resonances more shielded than that observed for PtO_2. The Pt oxide resonances of the

catalyst precursors was observed to be a broadened CSA lineshape and contained preferential orientations. This was attributed to the Pt oxide forming and depositing as oligomeric structures. These structures contained a mixture of OH and O bridges creating disorder. Also, these would have Pt–Pt inter nuclear distances different to PtO_2 which would account for the different chemical shifts observed.

The silica and α-alumina did not demonstrate any change through the research presented regarding catalyst support interactions. However, the γ-alumina was observed to react with the nitric acid of the precursors forming aluminium nitrate, which was still thought to be attached to the γ-alumina network. The species was narrow which was thought to be due to motion. Upon calcination, the species rapidly decomposed returning the Al to the alumina framework. From the γ-alumina it was also concluded that the catalyst metal oxides deposited preferentially on AlO(V) sites which were seen to disappear as calcination temperature increased. It is thought the oligomeric structures caused the AlO(V) to convert to AlO(VI) with the addition of an Al–O–Pt bond. This has not been directly observed in the ^{27}Al NMR though.

Changes were seen to occur in the ^{1}H NMR measurements carried out. However, speciation was not sufficient to allude to the evolution occurring. It has been proposed spin counting techniques and quantification of the ^{1}H signal measured could offer significant insights.

The use of ^{15}N labelled $Ni(NO_3)_2$ on γ-alumina and silica was carried out to study the role of nitrates and nitric acid. Both samples struggled to achieve CP conditions which indicated protons were not in the immediate vicinity. Thus, only nitrate species are likely present. The γ-alumina sample demonstrated a single resonance attributed to nitrate anions. However, a broad collection of nitrate species was observed on the silica sample. It was apparent an interaction between the nitric acid and silica had occurred. However, the consequences were not observed in the ^{29}Si NMR measurements.

Thus, further work is required to fully understand these hydrogenation catalyst systems. Correlation NMR experiments should enable further study of preferential binding sites. Washing and reduction of the samples may also provide further insight into the oligomeric structures.

References

(1) Purcell, E. M.; Torrey, H. C.; Pound, R. V. *Physical Review* **1946**, *69*, 37.

(2) Bloch, F.; Hansen, W. W.; Packard, M. *Physical Review* **1946**, *70*, 474.

(3) Bertini, I.; Bhaumik, A.; De Paëpe, G.; Griffin, R. G.; Lelli, M.; Lewandowski, J. R.; Luchinat, C. *Journal of the American Chemical Society* **2010**, *132*, 1032.

(4) Gabano, E.; Marengo, E.; Bobba, M.; Robotti, E.; Cassino, C.; Botta, M.; Osella, D. *Coordination Chemistry Reviews* **2006**, *250*, 2158.

(5) Smits, R. H. H.; Seshan, K.; Ross, J. R. H.; Kentgens, A. P. M. *The Journal of Physical Chemistry* **1995**, *99*, 9169.

(6) Zhang, R.; Mroue, K. H.; Ramamoorthy, A. *Accounts of Chemical Research* **2017**, *50*, 1105.

(7) Hanna, J. V.; Pike, K. J.; Charpentier, T.; Kemp, T. F.; Smith, M. E.; Lucier, B. E. G.; Schurko, R. W.; Cahill, L. S. *Chemistry – A European Journal* **2010**, *16*, 3222.

(8) Strobridge, F. C.; Middlemiss, D. S.; Pell, A. J.; Leskes, M.; Clement, R. J.; Pourpoint, F.; Lu, Z.; Hanna, J. V.; Pintacuda, G.; Emsley, L.; Samoson, A.; Grey, C. P. *Journal of Materials Chemistry A* **2014**, *2*, 11948.

(9) Fallah, M.; MacKenzie, K. J. D.; Hanna, J. V.; Page, S. J. *Journal of Materials Science* **2015**, *50*, 7374.

(10) Speight, R.; Wong, A.; Ellis, P.; Hyde, T.; Bishop, P. T.; Smith, M. E. *Solid State Nuclear Magnetic Resonance* **2009**, *35*, 67.

(11) Neri, G.; Milone, C.; Galvagno, S.; Pijpers, A. P. J.; Schwank, J. *Applied Catalysis A: General* **2002**, *227*, 105.

(12) Rees, G. J.; Orr, S. T.; Barrett, L. O.; Fisher, J. M.; Houghton, J.; Spikes, G. H.; Theobald, B. R. C.; Thompsett, D.; Smith, M. E.; Hanna, J. V. *Physical Chemistry Chemical Physics* **2013**, *15*, 17195.

(13) Edwards, J. C.; Adams, R. D.; Ellis, P. D. *Journal of the American Chemical Society* **1990**, *112*, 8349.

(14) Asaro, M.; Smith, R. M. In *Encyclopedia of Sustainability Science and Technology*; Meyers, R. A., Ed.; Springer New York: New York, NY, 2012; pp 3955.

(15) Todic, B.; Ordomsky, V. V.; Nikacevic, N. M.; Khodakov, A. Y.; Bukur, D. B. *Catalysis Science & Technology* **2015**, *5*, 1400.

(16) Khodakov, A. Y.; Chu, W.; Fongarland, P. *Chemical Reviews* **2007**, *107*, 1692.

(17) Steynberg, A. P.; Espinoza, R. L.; Jager, B.; Vosloo, A. C. *Applied Catalysis A: General* **1999**, *186*, 41.

(18) Luque, R.; de la Osa, A. R.; Campelo, J. M.; Romero, A. A.; Valverde, J. L.; Sanchez, P. *Energy & Environmental Science* **2012**, *5*, 5186.

(19) Bhutto, A. W.; Qureshi, K.; Abro, R.; Harijan, K.; Zhao, Z.; Bazmi, A. A.; Abbas, T.; Yu, G. *RSC Advances* **2016**, *6*, 32140.

(20) Fischer, F.; Tropsch, H. *Berichte der deutschen chemischen Gesellschaft (A and B Series)* **1926**, *59*, 830.

(21) Schulz, H. *Applied Catalysis A: General* **1999**, *186*, 3.

(22) Herrmann, W. A. *Angewandte Chemie International Edition in English* **1982**, *21*, 117.

(23) Guettel, R.; Turek, T. *Chemical Engineering Science* **2009**, *64*, 955.

(24) Iglesia, E. *Applied Catalysis A: General* **1997**, *161*, 59.

(25) Tavasoli, A.; Sadagiani, K.; Khorashe, F.; Seifkordi, A. A.; Rohani, A. A.; Nakhaeipour, A. *Fuel Processing Technology* **2008**, *89*, 491.

(26) Khodakov, A. Y. *Catalysis Today* **2009**, *144*, 251.

(27) den Breejen, J. P.; Radstake, P. B.; Bezemer, G. L.; Bitter, J. H.; Froseth, V.; Holmen, A.; de Jong, K. P. *J. Am. Chem. Soc.* **2009**, *131*, 7197.

(28) Dry, M. E. *Catal. Today* **2002**, *71*, 227.

(29) Schulz, H.; Claeys, M. *Applied Catalysis A: General* **1999**, *186*, 91.

(30) B., E.; A., F. R.; H., M. C.; R., S. G.; L., S. S. *Exxon's advanced gas-to-liquids technology*; Elsevier: Amsterdam, PAYS-BAS, 1998; Vol. 119.

(31) Elbashir, N. O.; Dutta, P.; Manivannan, A.; Seehra, M. S.; Roberts, C. B. *Applied Catalysis A: General* **2005**, *285*, 169.

(32) Klaigaew, K.; Samart, C.; Chaiya, C.; Yoneyama, Y.; Tsubaki, N.; Reubroycharoen, P. *Chemical Engineering Journal* **2015**, *278*, 166.

(33) Madikizela-Mnqanqeni, N. N.; Coville, N. J. *Journal of Molecular Catalysis A: Chemical* **2005**, *225*, 137.

(34) Girardon, J.-S.; Lermontov, A. S.; Gengembre, L.; Chernavskii, P. A.; Griboval-Constant, A.; Khodakov, A. Y. *Journal of Catalysis* **2005**, *230*, 339.

(35) Pakhomov, N. A.; Buyanov, R. A. *Kinetics and Catalysis* **2005**, *46*, 669.

(36) Khassin, A. A.; Yurieva, T. M.; Kustova, G. N.; Itenberg, I. S.; Demeshkina, M. P.; Krieger, T. A.; Plyasova, L. M.; Chermashentseva, G.

K.; Parmon, V. N. *Journal of Molecular Catalysis A: Chemical* **2001**, *168*, 193.

(37) Chen, J. G.; Sun, Y. H. In *Stud. Surf. Sci. Catal.*; Bao, X., Xu, Y., Eds.; Elsevier, 2004; Vol. 147, pp 277.

(38) Reuel, R. C.; Bartholomew, C. H. *Journal of Catalysis* **1984**, *85*, 63.

(39) Lok, C. M. **2004**, *147*, 283.

(40) Lok, M. C.; Kelly, G. J.; Gray, G. In; Google Patents, 2005.

(41) Casci, J. L.; Holt, E. M.; Neale, A. F. In; Google Patents, 2011.

(42) Schlessinger, G.; Simmons, J. W.; Jabs, G.; Chamberlain, M. M. In *Inorg. Synth.*; John Wiley & Sons, Inc., 2007; pp 173.

(43) Greenaway, A. M.; Lancashire, R. J. *J. Chem. Educ* **1982**, *59*, 419.

(44) Bauer, H. F.; Drinkard, W. C. *Journal of the American Chemical Society* **1960**, *82*, 5031.

(45) Jackson, W. G.; McKeon, J. A.; Zehnder, M.; Neuberger, M.; Fallab, S. *Chemical Communications* **2004**, 2322.

(46) Kauffman, G. In; Bull. Hist. Chem. Vol. 2014.

(47) Barron, L. D. *Molecular Light Scattering and Optical Activity*; Cambridge University Press, 2004.

(48) Moro, F.; Yu Tang, S. V.; Tuna, F.; Lester, E. *J. Magn. Magn. Mater.* **2013**, *348*, 1.

(49) Lloret, F.; Julve, M.; Cano, J.; Ruiz-García, R.; Pardo, E. *Inorg. Chim. Acta* **2008**, *361*, 3432.

(50) Chen, B.; Dingerdissen, U.; Krauter, J. G. E.; Lansink Rotgerink, H. G. J.; Möbus, K.; Ostgard, D. J.; Panster, P.; Riermeier, T. H.; Seebald, S.; Tacke, T.; Trauthwein, H. *Applied Catalysis A: General* **2005**, *280*, 17.

(51) Ray, K.; Deo, G. *Applied Catalysis B: Environmental* **2017**, *218*, 525.

(52) Hsu, N.; Diosady, L. L.; Rubin, L. J. *Journal of the American Oil Chemists Society* **1989**, *66*, 232.

(53) Zhang, X.; Tu, W.; Xiao, M.; Liu, Y.; Ye, J. *Current Applied Physics* **2017**, *17*, 1347.

(54) Konuspayeva, Z.; Berhault, G.; Afanasiev, P.; Nguyen, T.-S.; Giorgio, S.; Piccolo, L. *Journal of Materials Chemistry A* **2017**, *5*, 17360.

(55) Wicke, E. *Berichte der Bunsengesellschaft für physikalische Chemie* **1984**, *88*, 586.

(56) Tauster, S. J.; Fung, S. C.; Baker, R. T. K.; Horsley, J. A. *Science* **1981**, *211*, 1121.

(57) Campbell, C. T. *Nature chemistry* **2012**, *4*, 597.

(58) Mavrikakis, M.; Hammer, B.; Nørskov, J. K. *Physical Review Letters* **1998**, *81*, 2819.

(59) Bruix, A.; Rodriguez, J. A.; Ramírez, P. J.; Senanayake, S. D.; Evans, J.; Park, J. B.; Stacchiola, D.; Liu, P.; Hrbek, J.; Illas, F. *Journal of the American Chemical Society* **2012**, *134*, 8968.

(60) Wachs, I. E. *Catalysis Today* **1996**, *27*, 437.

(61) Storsæter, S.; Tøtdal, B.; Walmsley, J. C.; Tanem, B. S.; Holmen, A. *Journal of Catalysis* **2005**, *236*, 139.

(62) Trueba, M.; Trasatti, S. P. *European Journal of Inorganic Chemistry* **2005**, *2005*, 3393.

(63) Audi, G.; Bersillon, O.; Blachot, J.; Wapstra, A. *Nucl. Phys. A* **2003**, *729*, 3.

(64) MacKenzie, K. J.; Smith, M. E. *Multinuclear solid-state nuclear magnetic resonance of inorganic materials*; Elsevier, 2002; Vol. 6.

(65) Duer, M. J. *Introduction to Solid-State NMR Spectroscopy*; Wiley, 2005.

(66) Fayon, F.; Farnan, I.; Bessada, C.; Coutures, J.; Massiot, D.; Coutures, J. *Journal of the American Chemical Society* **1997**, *119*, 6837.

(67) Mason, J. *Solid State Nuclear Magnetic Resonance* **1993**, *2*, 285.

(68) Massiot, D.; Fayon, F.; Capron, M.; King, I.; Le Calvé, S.; Alonso, B.; Durand, J.-O.; Bujoli, B.; Gan, Z.; Hoatson, G. *Magnetic Resonance in Chemistry* **2002**, *40*, 70.

(69) Wasylishen, R. E.; Ashbrook, S. E.; Wimperis, S. *NMR of Quadrupolar Nuclei in Solid Materials*; Wiley, 2012.

(70) Power, W. P.; Wasylishen, R. E.; Mooibroek, S.; Pettitt, B. A.; Danchura, W. *The Journal of Physical Chemistry* **1990**, *94*, 591.

(71) Cheng, J. T.; Edwards, J. C.; Ellis, P. D. *The Journal of Physical Chemistry* **1990**, *94*, 553.

(72) Medek, A.; Frydman, V.; Frydman, L. *Journal of Physical Chemistry A* **1999**, *103*, 4830.

(73) Baugher, J. F.; Taylor, P. C.; Oja, T.; Bray, P. J. *The Journal of Chemical Physics* **1969**, *50*, 4914.

(74) Eichele, K. In, 2015.

(75) Bak, M.; Rasmussen, J. T.; Nielsen, N. C. *Journal of Magnetic Resonance* **2000**, *147*, 296.

(76) Ooms, K. J.; Bernard, G. M.; Kadziola, A.; Kofod, P.; Wasylishen, R. E. *Physical Chemistry Chemical Physics* **2009**, *11*, 2690.

(77) Menger, E.; Veeman, W. *Journal of Magnetic Resonance (1969)* **1982**, *46*, 257.

(78) Harris, R. K.; Olivieri, A. C. *Progress in nuclear magnetic resonance spectroscopy* **1992**, *24*, 435.

(79) Heise, H.; Kohler, F. H.; Brouwer, E. B.; Harris, R. K.; Steuernagel, S. *Magn. Reson. Chem* **1999**, *37*, 573.

(80) Ooms, K. J.; Wasylishen, R. E. *Canadian Journal of Chemistry* **2006**, *84*, 300.

(81) Apperley, D. C.; Harris, R. K.; Hodgkinson, P. *Solid State NMR: Basic Principles and Practice*; Momentum Press, 2012.

(82) Massiot, D.; Bessada, C.; Coutures, J. P.; Taulelle, F. *Journal of Magnetic Resonance (1969)* **1990**, *90*, 231.

(83) Massiot, D.; Farnan, I.; Gautier, N.; Trumeau, D.; Trokiner, A.; Coutures, J. P. *Solid State Nuclear Magnetic Resonance* **1995**, *4*, 241.

(84) Basolo, F.; Murmann, R. K.; Whitney, J. E.; Rollinson, C. L. In *Inorg. Synth.*; John Wiley & Sons, Inc., 2007; pp 171.

(85) Alexander, J. J.; Dorsey, J. G. *J. Chem. Educ* **1978**, *55*, 207.

(86) Kauffman, G. B.; Pinnell, R. P.; Crandall, J. K.; Jolly, W. L. In *Inorg. Synth.*; John Wiley & Sons, Inc., 2007; pp 176.

(87) Chan, J. C. C.; Au-Yeung, S. C. F. *Annual Reports on NMR Spectroscopy* **2000**, *41*, 1.

(88) Harris, R. K.; Becker, E. D.; Cabral de Menezes, S. M.; Goodfellow, R.; Granger, P. *Magnetic Resonance in Chemistry* **2002**, *40*, 489.

(89) Kirby, C. W.; Power, W. P. *Canadian Journal of Chemistry* **2001**, *79*, 296.

(90) Spiess, H. W. In *Dynamic NMR Spectroscopy*; Springer Berlin Heidelberg: Berlin, Heidelberg, 1978; pp 55.

(91) Medek, A.; Frydman, V.; Frydman, L. *Proceedings of the National Academy of Sciences* **1997**, *94*, 14237.

(92) Springborg, J.; Schäffer, C. E.; Wilson, M. L.; Wharton, J. M.; Hatfield, W. E. In *Inorg. Synth.*; John Wiley & Sons, Inc., 2007; pp 75.

(93) Coles, S. J.; Gale, P. A. *Chemical Science* **2012**, *3*, 683.

(94) Dolomanov, O. V.; Blake, A. J.; Champness, N. R.; Schroder, M. *Journal of Applied Crystallography* **2003**, *36*, 1283.

(95) Bureau, B.; Silly, G.; Buzaré, J. Y.; Legein, C.; Massiot, D. *Solid State Nuclear Magnetic Resonance* **1999**, *14*, 181.

(96) Fung, B. M.; Khitrin, A. K.; Ermolaev, K. *Journal of Magnetic Resonance* **2000**, *142*, 97.

(97) Zhu, J. H.; Wu, H. X.; Le Bail, A. *Solid State Sciences* **1999**, *1*, 55.

(98) Macikenas, D.; Hazell, R.; Christensen, A. N. *Acta Chemica Scandinavica* **1995**, *49*, 7.

(99) Christensen, A. N.; Hazell, R. G. *Acta. Chemica. Scandinavia* **1999**, *53*, 3.

(100) Haagensen, C. O.; Rasmussen, S. E. *Acta Chemica Scandinavica* **1963**, *17*, 1630.

(101) Barclay, G. A.; Hoskins, B. F. *Journal of the Chemical Society (Resumed)* **1962**, 586.

(102) Andersen, P. *Acta chem. scand* **1967**, *21*.

(103) Bernal, I.; Cetrullo, J.; Berhane, S. *Journal of Coordination Chemistry* **2000**, *52*, 185.

(104) Churchill, M. R.; Lashewycz, R. A.; Koshy, K.; Dasgupta, T. P. *Inorganic Chemistry* **1981**, *20*, 376.

(105) Feng, J.; Lee, Y. J.; Reeder, R. J.; Phillips, B. L. *Am. Mineral.* **2006**, *91*, 957.

(106) Sasane, A.; Smith, J. A. S. *Journal of Magnetic Resonance* **1978**, *32*, 265.

(107) Krishnamurty, K. V.; Mc Leod Harris, G.; Sastri, V. S. *Chemical Reviews* **1970**, *70*, 171.

(108) Kofod, P. *Magnetic Resonance in Chemistry* **2003**, *41*, 531.

(109) Jolly, W. L.; Harris, A. D.; Briggs, T. S. *Inorganic Chemistry* **1965**, *4*, 1064.

(110) Yoneda, H.; Nakashima, Y. *Bulletin of the Chemical Society of Japan* **1974**, *47*, 669.

(111) Nakashima, Y.; Sakaguchi, U.; Yoneda, H. *Chemistry Letters* **1974**, *3*, 503.

(112) Dobbins, R. J.; Harris, G. M. *Journal of the American Chemical Society* **1970**, *92*, 5104.

(113) Reynhardt, E. C. *Can. J. Phys.* **1974**, *52*, 1398.

(114) Jordan, R. B.; Sargeson, A. M.; Taube, H. *Inorganic Chemistry* **1966**, *5*, 486.

(115) Palmer, D. A.; Van Eldik, R. *Chemical Reviews* **1983**, *83*, 651.

(116) Koshy, K.; Dasgupta, T. P. *Journal of the Chemical Society, Dalton Transactions* **1984**, 2781.

(117) Dasgupta, T. P.; Harris, G. M. *Journal of the American Chemical Society* **1968**, *90*, 6360.

(118) Abdur-Rashid, K.; Dasgupta, T. P.; Burgess, J. *Journal of the Chemical Society, Dalton Transactions* **1994**, 2327.

(119) Jentsch, W.; Schmidt, W.; Sykes, A. G.; Wieghardt, K. *Inorganic Chemistry* **1977**, *16*, 1935.

(120) Wen, N.; Brooker, M. H. *The Journal of Physical Chemistry* **1995**, *99*, 359.

(121) Eriksen, J.; Monsted, L.; Mernsteda, O. *Acta Chemica Scandinavica* **1990**, *44*, 561.

(122) Wilson, A. D.; Stewart, F. F. *RSC Advances* **2014**, *4*, 11039.

(123) Karaca, H.; Safonova, O. V.; Chambrey, S.; Fongarland, P.; Roussel, P.; Griboval-Constant, A.; Lacroix, M.; Khodakov, A. Y. *Journal of Catalysis* **2011**, *277*, 14.

(124) Dou, D.; Liu, D.-J.; Williamson, W. B.; Kharas, K. C.; Robota, H. J. *Applied Catalysis B: Environmental* **2001**, *30*, 11.

(125) Still, B. M.; Kumar, P. G. A.; Aldrich-Wright, J. R.; Price, W. S. *Chemical Society Reviews* **2007**, *36*, 665.

(126) Levason, W.; Pletcher, D. *Platinum Metals Review* **1993**, *37*, 17.

(127) Fitzgerald, J. J.; Piedra, G.; Dec, S. F.; Seger, M.; Maciel, G. E. *Journal of the American Chemical Society* **1997**, *119*, 7832.

(128) d'Espinose de Lacaillerie, J.-B.; Fretigny, C.; Massiot, D. *Journal of Magnetic Resonance* **2008**, *192*, 244.

(129) Kwak, J. H.; Hu, J. Z.; Kim, D. H.; Szanyi, J.; Peden, C. H. F. *Journal of Catalysis* **2007**, *251*, 189.

(130) Taoufik, M.; Szeto, K. C.; Merle, N.; Rosal, I. D.; Maron, L.; Trébosc, J.; Tricot, G.; Gauvin, R. M.; Delevoye, L. *Chemistry - A European Journal* **2014**, *20*, 4038.

(131) Paluch, P.; Potrzebowska, N.; Ruppert, A. M.; Potrzebowski, M. J. *Solid State Nuclear Magnetic Resonance* **2017**, *84*, 111.

(132) Harris, R. K.; Becker, E. D.; Cabral De Menezes, S. M.; Goodfellow, R.; Granger, P. *Concepts in Magnetic Resonance* **2002**, *14*, 326.

(133) Maçon, A. L.; Jacquemin, M.; Page, S. J.; Li, S.; Bertazzo, S.; Stevens, M. M.; Hanna, J. V.; Jones, J. R. *Journal of Sol-Gel Science and Technology* **2017**, *81*, 84.

(134) Yokoi, T.; Mizuno, S.; Imai, H.; Tatsumi, T. *Dalton Transactions* **2014**, *43*, 10584.

(135) Zhou, Z.; Wang, S.; Zhou, W.; Wang, G.; Jiang, L.; Li, W.; Song, S.; Liu, J.; Sun, G.; Xin, Q. *Chemical Communications* **2003**, 394.

(136) Kwak, J. H.; Hu, J.; Mei, D.; Yi, C.-W.; Kim, D. H.; Peden, C. H. F.; Allard, L. F.; Szanyi, J. *Science* **2009**, *325*, 1670.

(137) Kraus, H.; Prins, R.; Kentgens, A. P. M. *The Journal of Physical Chemistry* **1996**, *100*, 16336.

(138) Vasilchenko, D.; Berdugin, S.; Tkachev, S.; Baidina, I.; Romanenko, G.; Gerasko, O.; Korenev, S. *Inorganic Chemistry* **2015**, *54*, 4644.

(139) Fantauzzi, D.; Bandlow, J.; Sabo, L.; Mueller, J. E.; van Duin, A. C. T.; Jacob, T. *Physical Chemistry Chemical Physics* **2014**, *16*, 23118.

(140) Kim, H. N.; Lee, S. K. *Geochimica et Cosmochimica Acta* **2013**, *120*, 39.

(141) Crocker, M.; Herold, R. H. M.; Wilson, A. E.; Mackay, M.; Emeis, C. A.; Hoogendoorn, A. M. *Journal of the Chemical Society, Faraday Transactions* **1996**, *92*, 2791.